UNICAMP

UNIVERSIDADE ESTADUAL DE CAMPINAS
Faculdade de Engenharia Mecânica

VICTOR ANTONIO SEIXAS DE MENEZES PAIVA

Statics, form-finding and dynamics of tensegrity systems

Estática, determinação de forma e dinâmica de sistemas tensegridade

Campinas

2024

VICTOR ANTONIO SEIXAS DE MENEZES PAIVA

Statics, form-finding and dynamics of tensegrity systems

Estática, determinação de forma e dinâmica de sistemas tensegridade

Thesis presented to the School of Mechanical Engineering of the State University of Campinas in partial fulfillment of the requirements for the degree of Doctor in Mechanical Engineering, in the field of Solid Mechanics and Mechanical Design.

Tese apresentada à Faculdade de Engenharia Mecânica da Universidade Estadual de Campinas como parte dos requisitos exigidos para a obtenção do título de Doutor em Engenharia Mecânica, na Área de Mecânica dos Sólidos e Projeto Mecânico.

Orientador: Prof. Dr. Paulo Roberto Gardel Kurka

Coorientador: Prof. Dr. Jaime Hideo Izuka

ESTE TRABALHO CORRESPONDE À VERSÃO FINAL DA TESE DE DOUTORADO DEFENDIDA PELO ALUNO VICTOR ANTONIO SEIXAS DE MENEZES PAIVA, E ORIENTADA PELO PROF. DR. PAULO ROBERTO GARDEL KURKA.

Campinas

2024

Ficha catalográfica
Universidade Estadual de Campinas (UNICAMP)
Biblioteca da Área de Engenharia e Arquitetura
Rose Meire da Silva - CRB 8/5974

P524s

Paiva, Victor Antonio Seixas de Menezes, 1994-
Statics, form-finding and dynamics of tensegrity systems / Victor Antonio Seixas de Menezes Paiva. – Campinas, SP : [s.n.], 2024.

Orientador(es): Paulo Roberto Gardel Kurka.
Coorientador(es): Jaime Hideo Izuka.
Tese (doutorado) – Universidade Estadual de Campinas (UNICAMP), Faculdade de Engenharia Mecânica.

1. Tensegridade (Engenharia). 2. Cinemática. 3. Membranas. 4. Vibração. 5. Método dos elementos finitos. 6. Análise estática. 7. Robótica. I. Kurka, Paulo Roberto Gardel, 1958-. II. Izuka, Jaime Hideo, 1974-. III. Universidade Estadual de Campinas (UNICAMP). Faculdade de Engenharia Mecânica. IV. Título.

Informações complementares

Título em outro idioma: Estática, determinação de forma e dinâmica de sistemas tensegridade
Palavras-chave em inglês:
Tensegrity (engineering)
Kinematics
Membrane
Vibration
Finite element method
Static analysis
Robotics
Área de concentração: Mecânica dos Sólidos e Projeto Mecânico
Titulação: Doutor em Engenharia Mecânica
Banca examinadora:
Paulo Roberto Gardel Kurka [Orientador]
Carlos Magno de Oliveira Valente
Fabiano Fernandes Bargos
Renato Pavanello
Tiago Henrique Machado
Data de defesa: 04-11-2024
Programa de Pós-Graduação: Engenharia Mecânica

Identificação e informações acadêmicas do(a) aluno(a)
- ORCID do autor: https://orcid.org/0000-0003-2862-1717
- Currículo Lattes do autor: http://lattes.cnpq.br/7439457585525706

UNIVERSIDADE ESTADUAL DE CAMPINAS
FACULDADE DE ENGENHARIA MECÂNICA

TESE DE DOUTORADO ACADÊMICO

Statics, form-finding and dynamics of tensegrity systems

Estática, determinação de forma e dinâmica de sistemas tensegridade

Autor: Victor Antonio Seixas de Menezes Paiva

Orientador: Prof. Dr. Paulo Roberto Gardel Kurka
Coorientador: Prof. Dr. Jaime Hideo Izuka

A Banca Examinadora composta pelos membros abaixo aprovou esta Tese de Doutorado:

Prof. Dr. Paulo Roberto Gardel Kurka, Presidente
DSI - Faculdade de Engenharia Mecânica - Universidade Estadual de Campinas

Prof. Dr. Carlos Magno de Oliveira Valente
Insper - Instituto de Ensino e Pesquisa

Prof. Dr. Fabiano Fernandes Bargos
DEBAS - Escola de Engenharia de Lorena - Universidade de São Paulo

Prof. Dr. Renato Pavanello
DMC - Faculdade de Engenharia Mecânica - Universidade Estadual de Campinas

Prof. Dr. Tiago Henrique Machado
DSI - Faculdade de Engenharia Mecânica - Universidade Estadual de Campinas

A Ata de Defesa com as respectivas assinaturas dos membros encontra-se no SIGA/Sistema de Fluxo de Dissertação/Tese e na Secretaria do Programa da Unidade.

Campinas, 4 de Novembro de 2024

DEDICATÓRIA

Tudo para a Andréia, minha companheira, e para a Lucia e o Toninho, meus pais. Mesmo sem dominar o tema, essas três pessoas sofreram comigo nas incontáveis recusas de artigos e vibraram com as aprovações como se fossem conquistas próprias, porque, de fato, são.

AGRADECIMENTOS

Durante o período do doutorado na Unicamp, atuei como professor no Insper. Após sentir os desafios dessa profissão na pele, considero justo e necessário dedicar os agradecimentos aos professores e professoras que marcaram a minha vida e me inspiram.

Agradeço ao professor Paulo Kurka, que me recebeu em 2015 para uma iniciação científica e me deu liberdade e confiança durante o mestrado e doutorado. A cena dele sentado na escada do ciclo básico atendendo estudantes com dúvidas é uma fonte eterna de inspiração. Agradeço ao professor Jaime Izuka, a quem devo a carreira, por me orientar desde a iniciação científica com paciência inesgotável, espero continuar os trabalhos no futuro e conservar a amizade pelo resto da vida. Agradeço ao professor Caio Santos por me apresentar um universo novo, compartilhar seus métodos de ensino e me apoiar sempre que precisei. Agradeço às professoras Lilian e Akemi por me acolherem e apoiarem durante os períodos de mudança.

Agradeço aos professores Fabiano, Renato Pavanello, Tiago e Dinho pela participação na banca, os comentários fornecidos são valiosos e melhoraram esse documento. Agradeço aos prof. Renato Pavanello e Marco Lucio por me oferecerem a minha primeira experiência como monitor e me fazerem admirar resistência dos materiais. Agradeço à professora Katia e aos professores Gregory e Tiago por me apresentarem a beleza da dinâmica.

Agradeço às professoras Bartira e Ayako, de japonês, ao professor Dries, de propulsão, ao professor Carlos, de economia, ao professor Raphael, preparador de goleiro, ao professor Minoru, de desenho, ao professor Freitas, de estatística, e ao professor Ramires, de cálculo.

Agradeço aos professores Teixeira, Fred, Celso, Pelicano, Ronny, Franco, Alfredo, Gabriel, Julien, Rafael, Jeff e às professoras Joice e Angélica, que vem dividindo a sala de aula comigo. Agradeço aos professores Galdino, Dinho e Paulo da república da Graúna.

Agradeço ao professor Maurício de Carvalho, de física mecânica, que usa uma paixão contagiante pelo tema para vencer um sistema de vestibular pouco estimulante. Agradeço ao professor Julio Tonon, de biologia, à professora Sol, de literatura e à professora Ivany e ao professor Rogers, de química, que têm humor e oratória espetaculares. Agradeço à professora Maria Lúcia e ao professor Olivares, de matemática, à professora Débora, de ensino religioso, à professora Vanessa, de língua portuguesa, ao professor Fernando, de educação física, e aos professores Gerson e Vagner, de história.

RESUMO

Estruturas e mecanismos de tensegridade têm atraído a atenção da comunidade científica devido ao seu potencial em associado a transformação de forma e eficiência estrutural em termos de resistência por peso. Sistemas de tensegridade podem ser projetados para empacotar, desenvolver e transformar em uma geometria de interesse. Essas características fazem das tensegridades alternativas promissoras para substituir braços manipuladores sólidos, que geralmente são pesados, longos e inconvenientes para transportar. Adicionalmente, antenas de satélites necessitam de uma superfície contínua para reflexão, o que motiva a pesquisa de sistemas tensegridade-membrana. Este estudo apresenta o objetivo geral de contribuir para a consolidação de sistemas tensegridade através da produção de um trabalho abrangente entre temas fundamentais da engenharia mecânica, fornecendo análises de estática e dinâmica, em duas e três dimensões do espaço, e por vias analíticas, numéricas e experimentais. Quatro projetos são apresentados: uma membrana triangular pré-tensionada, uma viga tensegridade plana puxada por um cabo na extremidade livre, definições analíticas de conectividade e incidências para prismas tensegridade e um braço 3D tensegridade que se expande e move conforme os comprimentos dos cabos variam. Os códigos fundamentais implementados em MATLAB estão disponíveis no repositório *GitHub* público <https://github.com/FictorP/Tensegrity/tree/main/formfinding>.

É razoável desenvolver um modelo de membrana antes de avançar para sistemas de tensegridade-membrana. Esta parte do estudo é dedicada à construção de um modelo numérico confiável de membrana. A membrana pré-tensionada é modelada num programa comercial e validada com um protótipo. O protótipo de borracha é cortado em um formato triangular, montado sobre um quadro e tensionado sob diversos níveis de carga. As frequências naturais são extraídas por processamento de imagem em cada configuração. A estrutura é reproduzida em um programa comercial e o modelo numérico é validado com os resultados experimentais.

A viga plana é submetida a grandes deslocamentos e vibração, os modelos numéricos para as análises estática não linear e modal são validados com um protótipo fabricado por manufatura aditiva. A metodologia para resolver a análise estática não linear é baseada no procedimento de cálculo de rigidez de elemento de barra pré-tensionado e no método de cargas incrementais de Euler. O protótipo é sujeito a diversos níveis de carga, o que gera diversas configurações deformadas. As frequências naturais são extraídas em cada configuração por processamento de imagem e testes com martelo de impacto e acelerômetro. O modelo numérico é calibrado com os resultados experimentais e uma análise de vibração completa é executada para todas as posições deformadas intermediárias.

Pesquisadores aplicam prismas tensegridade regulares para montar torres e grades, mas não há uma definição analítica para a matriz de conectividade dos membros. A metodologia apresentada nesta tese traz expressões genéricas para as matrizes de coordenadas dos nós, incidência e conectividade válidas para qualquer prisma tensegridade regular. Em seguida, essas expressões são aplicadas no método de determinação de forma do projeto do braço de tensegridade, que é um empilhamento de prismas.

O projeto do braço pode ser dividido em três estágios: expansão de uma configuração plana em uma torre de alta razão de aspecto, encurvamento da estrutura desenvolvida para gerar um movimento de manipulador, e cinemática inversa. A determinação de forma é obtida através de métodos cinemáticos, minimizando os comprimentos dos cabos para encontrar configurações estáveis, e a cinemática inversa é resolvida por redes neurais. Seis módulos quadruplex são combinados para montar o mecanismo deste estudo, mas a metodologia apresentada é válida para qualquer combinação de tensegridades cilíndricas.

Palavras–chave: tensegridade, determinação de forma, estática não linear, membrana, vibrações, conectividade

ABSTRACT

Tensegrity structures and mechanisms have drawn the attention of the scientific and engineering communities due to their potential related to shape shifting attributes and structural efficiency in terms of resistance per weight. Tensegrity systems can be designed to pack, deploy and transform their shape into a desired geometry. These characteristics make tensegrities promising alternatives to replace solid manipulator arms, which are usually heavy, long and inconvenient to transport. Additionally, satellite antennas require a continuous surface to reflect, which motivates the research of tensegrity-membrane systems. This study presents a global aim of contributing to the advancement of tensegrity systems by producing a comprehensive work that integrates fundamental topics in mechanical engineering, providing static and dynamic analyses in two and three dimensions in space through analytical, numerical, and experimental approaches. Four projects are presented: a prestressed triangular shaped membrane, a planar tensegrity beam guyed by a cable on its free end, analytical definitions for connectivity and incidence for tensegrity prisms and a 3D tensegrity arm that expands and moves as the cable lengths vary. The essential MATLAB scripts are posted in the public *GitHub* repository <https://github.com/FictorP/Tensegrity/>.

It is reasonable to develop a membrane model before advancing to tensegrity-membrane systems. This part of the study is dedicated to building a reliable numerical membrane model. The prestressed membrane is modeled in commercial software and validated with a prototype. The rubber prototype is cut into a triangular shape, mounted on a frame, and stressed under various load levels. Natural frequencies are extracted by image processing in each configuration. The structure is reproduced in commercial software, and the numerical model is validated with experimental results.

The planar beam is subjected to large displacements and vibration. The numerical models for nonlinear static and vibration analyses are validated with a 3D printed prototype. The methodology to perform the nonlinear static analysis is based on a procedure to calculate prestressed bar element stiffness and Euler's incremental loads method. The prototype is subjected to various load levels, generating multiple deformed configurations. Natural frequencies are extracted in those configurations by image processing and impact hammer tests with an accelerometer. The numerical model is calibrated with the experimental results, and a full vibration analysis is performed for all intermediate deformed configurations.

Researchers apply regular tensegrity prisms to assemble towers and grids, but an analytical definition for the member connectivity matrix is missing. The methodology presented in this thesis provides general expressions for node coordinates, incidence, and connectivity matrices, valid for any regular tensegrity prism. Subsequently, these expressions are applied in the form-finding method for the design of the tensegrity arm, which is a stack of prisms.

The arm design study can be divided into three stages: deployment of a flat configuration into a high aspect ratio tower, bowing the deployed structure to generate manipulator movement, and inverse kinematics. Form-finding is achieved through kinematical methods, by minimizing cable lengths to find stable configurations, and inverse kinematics is solved by neural networks. Six quadruplex modules are combined to assemble the mechanism of this study, but the presented methodology covers any stacking of cylindrical tensegrities.

Keywords: tensegrity, form-finding, nonlinear statics, membrane, vibration, connectivity

LIST OF FIGURES

LIST OF TABLES

LIST OF ABBREVIATIONS AND ACRONYMS

ASME	American Society of Mechanical Engineering
FEM	Finite element method
FPS	Frames per second
ICAS	International Council of the Aeronautical Sciences
SMFF	Stiffness matrix form-finding

LIST OF SYMBOLS

b	Bar length
f	Function for the Newton-Raphson routine
h	Prism height
i	Number of rows in matrix $\mathbf{H}$
j	Number of columns in matrix $\mathbf{H}$
l	Horizontal cable length
t	Number of struts
v	Vertical cable length
x	Node coordinate in the x-axis
y	Node coordinate in the y-axis
z	Node coordinate in the z-axis
$\mathbf{n}$	Node coordinates vector
$\mathbf{H}$	Generic $i \times j$ matrix
$\mathbf{G}$	Generic $\alpha \times \beta$ matrix
α	Number of rows in matrix $\mathbf{G}$
β	Number of columns in matrix $\mathbf{G}$

CONTENTS

1 INTRODUCTION

Tensegrity structures gained popularity in 1948 for their artistic value. Later, their potential for engineering applications was recognized by Buckminster Fuller, who coined the term tensegrity by merging the words 'tensional' and 'integrity' (Fuller; Applewhite, 1975). Tensegrity structures are composed of discontinuous bars or struts under compression and continuous tensile elements (cables) connected by torqueless joints (Zhang; Ohsaki, 2015b). The stressed state of the structure provides stability and affects the system stiffness (Motro, 1992), and a tensegrity structure must be stable without external forces. Furthermore, the maximum number of bars in contact determines the class of a tensegrity. In a class 1 tensegrity, the bars do not touch each other (Skelton; Oliveira, 2009).

The advantages of tensegrities over traditional structures have drawn the attention of researchers from various fields, such as architecture (Jáuregui, 2020), robotics (Paul *et al.*, 2006), material sciences (Fraternali *et al.*, 2012) and even biology (Ingber, 2003) and DNA related research (Liedl *et al.*, 2010). Three of the main advantages of tensegrity systems are highlighted in this work: uniaxial stress, stiffness control and shape transformation.

The uniaxial stress condition guarantees that the bars remain under compression while the cables remain under traction (Ashwear; Eriksson, 2014). In terms of applications in engineering, this property contributes to an optimized material selection and to well defined boundary conditions in kinematical studies. The designer can select a traction resistant material to build the cables and a compression (and buckling) resistant material to manufacture the struts (Motro, 1992). In terms of modelling, the uniaxial stress property is advantageous to know which elements are potentially subject to compression or traction in advance. This information creates opportunities to optimize the numerical methodologies developed in this study.

Cables are usually selected as the tensile components in tensegrity systems, but membranes can also act as tensile elements and replace the cables in a few designs. These assemblies are called tensegrity-membrane systems and can be useful, for example, in satellite antennas. They combine the advantages of tensegrity systems with the possibility of using a membrane to act as a reflective surface. However, implementing a membrane finite element model can be challenging. Numerous researchers have addressed this problem, but much of the published literature skips steps when defining these models. In this work, a numerical model of a prestressed membrane is developed in commercial software (ANSYS) to assess its vibration behavior. Various stress levels are analyzed, and a triangular membrane prototype (Figure 1.1) is experimented with and compared to the numerical model.

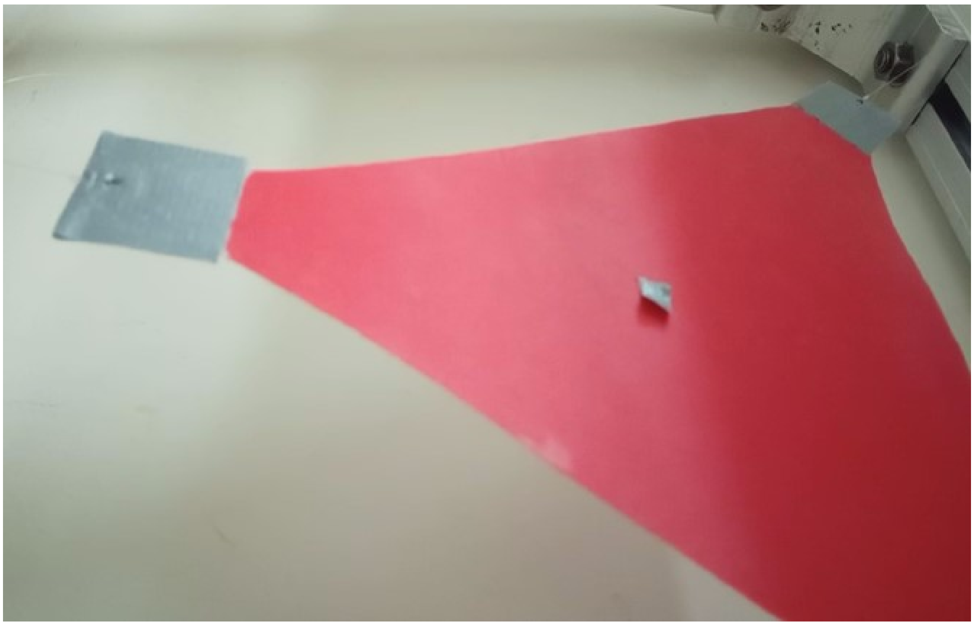

Figure 1.1 – Prestressed membrane.

Traditional structures, such as beams and trusses, would have to be rebuilt in order to adjust their stiffness or geometry. However, a tensegrity system can have its stiffness and geometry adjusted by varying the prestress in its cables. Furthermore, if the stresses are proportionally changed, the geometry remains. This property is assessed in this study with a planar tensegrity beam under large displacements (Figure 1.2). The nonlinear changes in geometry cause significant variation in the cable stresses and natural frequencies, which are extracted by an accelerometer and image processing. The community has developed several strategies for solving nonlinear static analyses using the finite element method (FEM) and has applied FEM methodologies to tensegrity systems. However, studies involving nonlinear statics on tensegrity structures are rare or rely on lengthy strategies. Additionally, while many works address tensegrity beams, few develop models for their control. This work aims to fill these gaps with a straightforward methodology validated by experiments.

The overall shape of tensegrity systems can be organized into categories: prismatic, spherical, humanoid and bio-inspired (Liu *et al.*, 2022). Tensegrity prisms are formed by two polygonal bases connected by struts joining their vertexes. For example, the simplest prism (triplex) is formed by two triangular shapes (three cables each), three bars connecting the bottom

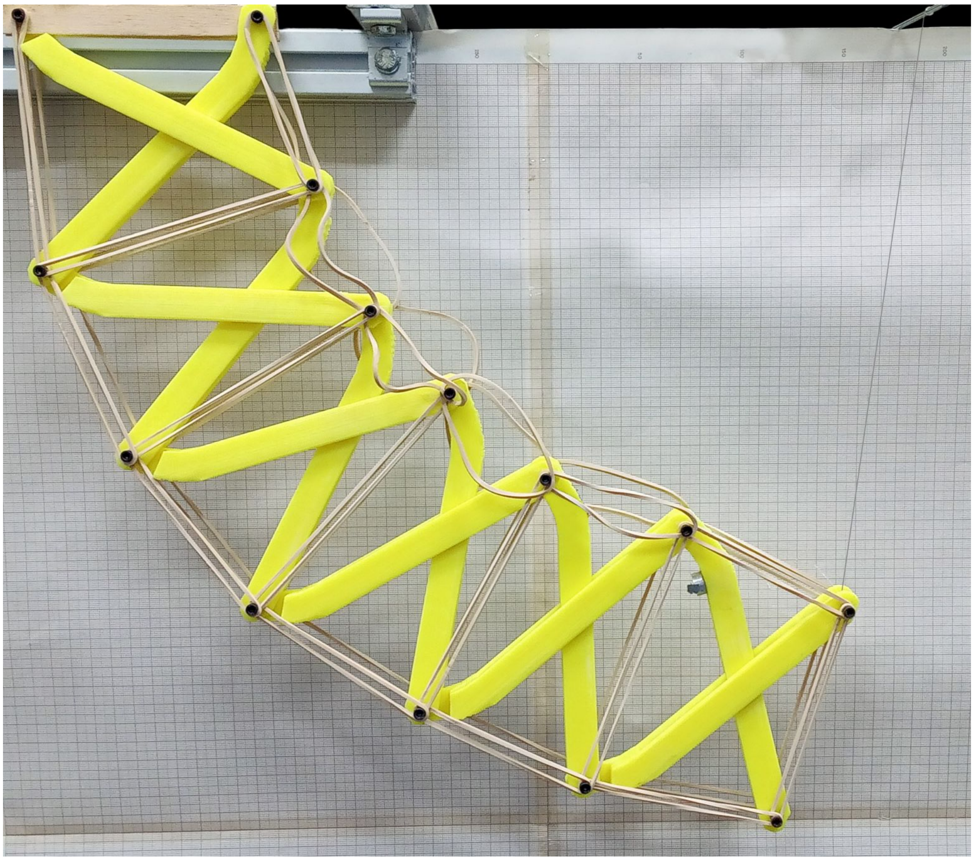

Figure 1.2 – Tensegrity beam.

and top vertexes, and three cables also connecting the bottom and top vertexes. The number of bars dictates the number of sides in the polygonal bases and the total number of cables. Additionally, the rotation of the top base can be clockwise or counterclockwise relative to the bottom base (Figure 1.3). However, the general definition of node, connectivity and incidence matrices for prisms with four or more struts are missing in the literature. In this work, analytical definitions for those matrices are provided using floor and ceiling functions.

The geometry of a tensegrity can also be changed by varying the cable lengths. However, determining its final form given the member lengths is a relatively complex problem. This problem category has been defined as form-finding, and numerous techniques have been developed. Among them, kinematical methods usually fix the length of the bars and minimize the length of the cable elements. The literature contains several works that apply kinematical methods, particularly those based on dynamic relaxation. However, a detailed, step-by-step algorithm for form-finding using nonlinear programming is still lacking. In this study, a 3D arm (Figure 1.4) is designed and a kinematical form-finding procedure is developed to calculate its deployment and shape transformation. Additionally, the inverse kinematics is calculated using

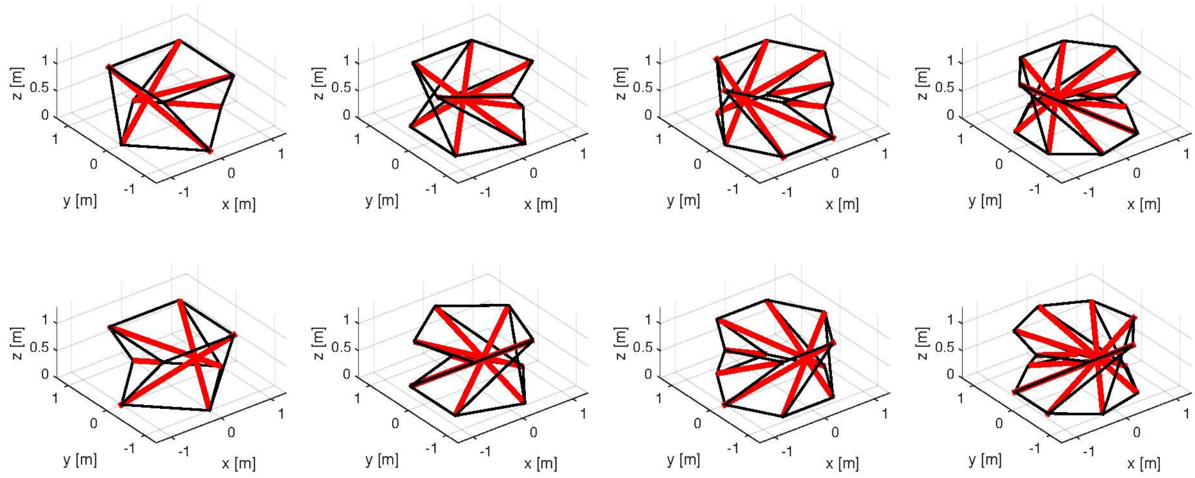

Figure 1.3 – Regular tensegrity prisms.

an artificial neural network.

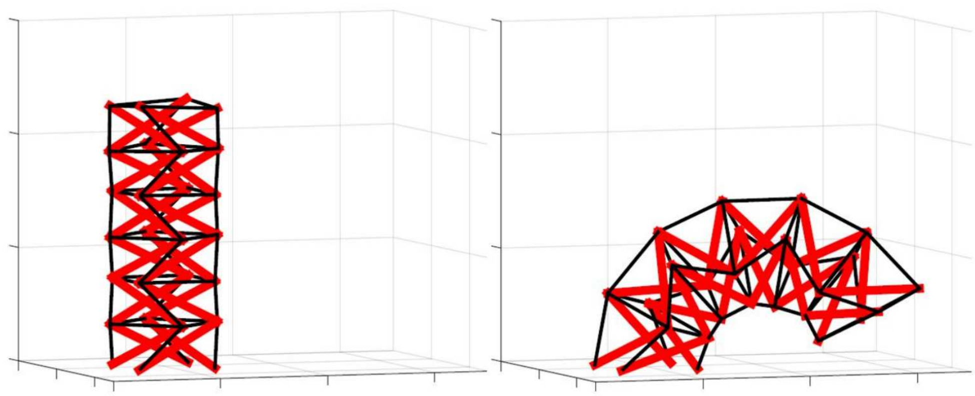

Figure 1.4 – Tensegrity arm.

1.1 Objectives

The overall objective of this work is to enhance the recognition of tensegrity and tensegrity-membrane systems as potential solutions to engineering challenges. This is achieved by reporting studies across an extensive range in solid mechanics, including static, kinematic, vibration and control analyses, in two- and three-dimensional environments, using analytical, numerical, and experimental approaches. To fulfill this global goal, four independent projects are performed, with the following specific objetives:

- Implement a numerical model of a membrane in a commercial software and validate the outputs with a prototype.

- Develop a methodology to solve nonlinear static analyses of prestressed tensegrity structures.
- Perform a vibration study on a planar tensegrity beam and validate with experimental results.
- Develop analytical definitions for node, incidence and connectivity matrices for tensegrity prisms.
- Develop a form-finding procedure to deploy a transportable packed tensegrity system into a high structure and afterwards into a bowed arm.

1.2 Thesis structure

This thesis follows the paper-based format: Chapter 2 contains a literature review related to statics, form-finding and dynamics of tensegrity and tensegrity-membrane systems, Chapter 3 covers the tensegrity-membrane report presented in the *International Congress of the Aeronautical Sciences 2022*, Chapter 4 presents the tensegrity beam study published in the *Journal of Mechanisms and Robotics*, Chapter 5 contains the analytical definitions of node, incidence and connectivity matrices of tensegrity prisms published in the *Mechanics Research Communications* journal, and chapter 6 shows the tensegrity arm work published in *Meccanica*. Chapter 7 discusses how those studies are connected and brings methodological challenges that have been omitted in the papers for conciseness. Chapter 8 summarizes the main conclusions, limitations of the developed procedures and future research directions. Appendix A shows the definition of the Kronecker product applied in Chapter 4 and appendices B, C and D present the permission to use content by the publishers that hold copyrights. The MATLAB scripts used in the form-finding and beam projects are publicly available at <https://github.com/FictorP/Tensegrity/>.

2 LITERATURE REVIEW

Tensegrity theory and mechanisms have been applied to robotics recently. Four main categories of tensegrity robots can be defined (Liu *et al.*, 2022), according to their shapes: prismatic (Arsenault; Gosselin, 2009), spherical (SunSpiral *et al.*, 2015), humanoid (Lessard *et al.*, 2016) and bio-inspired (Liu; Yao, 2019). The spherical shape can also be achieved with curved members (Schorr *et al.*, 2021; Jahn *et al.*, 2024). The 3D arm (Chapter 6) studied in this thesis can be mostly associated with the prismatic category, as it combines tensegrity prisms to assemble a tower. However, it performs a manipulator movement in the second stage of the study. Therefore, it could be combined with a gripper (Sumi *et al.*, 2017) to integrate a humanoid robot design. The planar beam (Chapter 4) can be equally associated with the humanoid and bio-inspired categories.

Some characteristics of tensegrity robots are attractive to space engineering projects, such as low weight and deployment capability. The Super Ball bot (Agogino *et al.*, 2018) is an icosahedral tensegrity robot with 24 cables and 6 bars and was designed to be used as a space exploration probe. The high resistance to impact of the probe is useful for landing, and the system rolls to explore the terrain, as cables are tension-controlled. Also, space exploration vehicles usually contain a camera on top of a solid mast to reach a farther horizon and collect data of scientific interest. For example, the Mars 2020 *Perseverance* rover (Maki *et al.*, 2020) has a mast that carries two cameras (Navcam), tilts to increase its field of view and provides an advantageous position from a higher spot. However, a flexible mast (Holland *et al.*, 2006; Kurka *et al.*, 2014) could bring more features to the probe by bending to explore cliffs and difficult access regions. The disadvantage associated with a long and flexible beam is the nonlinear behavior and vibration. Therefore, sophisticated techniques are required to predict its kinetics. The planar beam (Chapter 4) is a tip pulled tensegrity version of a space exploration mast, that brings the advantages of tensegrity structures to a space exploration vehicle. Its nonlinear static behavior and vibrations are studied. In addition, a 3D tensegrity arm (Chapter 6) is advantageous because the movements are driven by the internal cables of the structure, avoiding the necessity to attach a pulling cable to the tip of the structure to provide bending. Also, the compact shape is helpful to save volume in the launcher and absorb impact on landing (Sabelhaus *et al.*, 2015). Many aerospace structures require reflective surfaces, such as satellite antennas and sails. Pure tensegrity systems cannot fulfill that requirement, but tensegrity-membrane structures provide a surface that can be covered with a reflective skin and take advantage of the benefits associated to tensegrity systems (Teixeira *et al.*, 2018; Kurka *et al.*, 2018). To better predict the behavior of tensegrity-membrane systems, it is reasonable to build a reliable numerical model of a prestressed membrane (Chapter 3). The natural frequencies obtained numerically are compared with image processing outputs from a prototype.

2.1 Prestressed membrane

The propulsion efficiency of a spacecraft depends on a low ratio of overall mass to solar sail and antenna area. Technological solutions for in-orbit deployable, ultralightweight sail and antenna surfaces are, therefore, in high demand (Leipold *et al.*, 2005).

The modification of space structure may require adding numerous components, leading to weight increase (Yang; Sultan, 2017). The mechanical properties of tensegrity-membrane systems make them appealing solutions for lightweight and deployable systems that the aerospace industry can apply and substitute a pure tensegrity structure (Gebara *et al.*, 2019; Yang; Sultan, 2019; Leipold *et al.*, 2005). Yang and Sultan (2016) used the total Lagrangian formulation to perform a dynamics study of a tensegrity-membrane structure. Goyal *et al.* (2017) designed a growth adaptable artificial gravity space habitat based on a tensegrity-membrane structure.

The membrane of the tensegrity system performs a structural role as a tensile element, and can perform a reflective function if covered by a reflective skin. As membranes are usually very flexible, their vibration behavior has a direct impact on their geometry and efficiency (Kukathasan; Pellegrino, 2002). Therefore, accurate models to calculate their vibration behavior are in demand. Sunny *et al.* (2012) suggests a method that provides an analytical approximation to the behavior of prestressed membranes. Liu *et al.* (2021) modeled an umbrella membrane in ANSYS and analysed its behavior under different sets of rain loads. The numerical results were validated with a prototype. Hu *et al.* (2017) performed vibration studies of an inflatable tube and a plane film and compared numerical and experimental results for different internal pressures of the tube and for wet and dry conditions. Wei *et al.* (2018) modeled a triangular plane membrane and a long inflatable boom and validated the numerical results with prototypes. The authors suggest the use of catenary-shaped edges to reduce wrinkling of the triangular membrane and compare the stress analysis with a straight edge model. Catenary edges on membranes are implemented experimentally by (Wong; Pellegrino, 2006a), analytically by (Wong; Pellegrino, 2006b) and numerically by (Wong; Pellegrino, 2006c).

Vibration studies can be used to detect structural damage. Hu *et al.* (2019) proposed a methodology to detect local damage in rectangular and circular membranes by combining Bayesian operational modal analysis and 3D digital image correlation. The damped vibration response of a membrane under impact loads is studied experimentally (Liu *et al.*, 2019), analytically (Liu *et al.*, 2019) and numerically (Li *et al.*, 2018). Finally, Liu *et al.* (2018) suggested a methodology to use the vibration response to a local impact to find the stress level of a membrane. The triangular membrane studied in this thesis is stressed at different levels, and its natural frequencies are recorded and extracted by image processing. A numerical model is created in ANSYS, and the results are compared.

2.2 Tensegrity beam

Tensegrity structures have the particularity to eventually display large nodal displacements even when the deformations of its members are small (Kebiche *et al.*, 1999). Also, the occurrence of slack cables is problematic in tensegrity mechanisms because it generates rough movements, especially when those cables constantly change from stressed to slack states (Kan *et al.*, 2018a; Shi *et al.*, 2020). Numerous researchers have suggested methodologies for nonlinear analysis of tensegrity systems. Kebiche *et al.* (1999) proposed a methodology for tensegrity structures considering geometrical nonlinearities. They applied a total Lagrangian formulation to calculate the internal stress vector and the tangent matrix of a four struts tensegrity system under compression, traction, bending, and torsion loads. A stressed multi-cell beam was also investigated, and the outputs present a nonlinear behavior caused by the flexibility. They observed that the stiffness of the system increases with the self-stress level and external loads. However, the behavior is different under compressive loads. Analogously to anisotropic materials, the orientations of the loads dictate the displacements.

Tran and Lee (2011) proposed a numerical method for large displacements that considers nonlinearities in geometry and material properties. Total and updated Lagrangian formulations were applied to assess the geometrical nonlinearity, and the elastoplastic stress-strain relationship was used to account for the material nonlinearity. The suggested procedure determines responses of the quadruplex unit module, five-quadruplex module beam and double layer quadruplex grid. The outputs agree with the work presented by Kebiche *et al.* (1999)

and support that stiffness and self-stress increase together. The stretching (instead of bending) stiffness is dominant in the quadruplex unit module. The self-stress level does not affect the bending strength capacity of the double layer quadruplex tensegrity grid.

Zhang *et al.* (2013) developed a numerical methodology that can be applied for tensegrity systems both externally or internally actuated. The procedure captures mechanical responses of tensegrities subject to large and nonlinear deformation under different conditions. The dynamics and control aspects of tensegrity systems are in evidence, but a static analysis for critical situations is relevant in most engineering projects. Therefore, it is beneficial for the community to document new methods and validate them with experiments involving statics.

Skelton and Oliveira (2009) show a methodology to determine the stiffness of a tensegrity for given element stresses and material properties. That stiffness is suitable to perform a linear static analysis. But large displacements and internal stresses create nonlinearities associated to geometry and tension and provide inaccurate results. The study shown in Chapter 4 extends the reach of that methodology by presenting an algorithm that can be applied when large deformations are involved as well. Faroughi and Lee (2014) and Zhang *et al.* (2016) used a co-rotational approach to solve the nonlinear structural problem. Murakami (2001) obtained the equation of motion of the tensegrity system through Euler method and updated Lagrangian formulation.

The method presented in this thesis combines the methodology shown in (Skelton; Oliveira, 2009) for pre-stressed tensegrity structures with Euler (or incremental) loads algorithm (Crisfield, 1991). A 3D printed prototype of the 3D arm is used to validate the numerical model. The experiments contemplate five load levels. A vibration study is performed in those deformed configurations, the natural frequencies are obtained by an acceleromenter and by image processing and compared to the numerical results.

2.3 Analytical studies

Prismatic or cylindrical tensegrity structures consist of two parallel polygonal bases. A regular t-strut prism is built from two t-sided polygons, each composed of t cables, connected by t struts and t vertical cables. These modules are also referred to as triplex, quadruplex, and so on, depending on the number of struts (Vassart; Motro, 1999). Tensegrity prism modules have been extensively studied (Micheletti *et al.*, 2019; Xu; Luo, 2010; Amendola *et al.*, 2014; Ma *et al.*, 2018) and combined to generate masts (Furuya, 1992) or grids (Wendling *et al.*, 2003; Tran; Lee, 2010). The specific number of struts in a tensegrity prism determines its shape and results in associated node and connectivity matrices. Modules with 3-struts (triplex) (Furuya, 1992; Fraternali *et al.*, 2012), 4-struts (quadruplex) (Feron *et al.*, 2019; Wendling *et al.*, 2003; Tran; Lee, 2010), 5-struts (pentaplex) (Feron *et al.*, 2019), 6-struts (Feron *et al.*, 2019), and others have been applied by the community. Although many articles specify their node and connectivity matrices, few studies have focused on deriving general definitions for these matrices.

Node positions can be generated using widely-known form-finding techniques, such as force density (Zhang; Ohsaki, 2015a), dynamic relaxation (Ali *et al.*, 2011), and kinematical methods (Tibert; Pellegrino, 2011), but most of these techniques require a connectivity matrix as input. The adapted force density method described in (Yu *et al.*, 2022) can be employed to model T-4 tensegrity structures, including regular prisms like the quadruplex module referenced in numerous studies. However, this method involves numerical procedures to generate the connectivity matrix and then identifies whether members are bars or cables. A more efficient approach could involve deriving the connectivity matrix directly from the geometry.

This issue has been partially addressed; the methodology to obtain the connectivity of a 3-strut tensegrity prism is covered in (Nagase *et al.*, 2016). Furthermore, they construct a global connectivity matrix for combinations of 3-strut prisms: stacked to form towers or aligned to create grids. This work is expanded in (Jiang *et al.*, 2020), where a general definition for the node matrix of tensegrity plates formed by 3-strut prisms of any complexity is developed. Additionally, they explore assemblies of reinforced 3-strut prisms, which include extra cables to enhance stiffness. However, analytical definitions for node and connectivity matrices applicable to prisms with more than three struts remain undeveloped.

Research groups in materials science (Angelo *et al.*, 2020) and biomechanics (Bansod *et al.*, 2018) may prefer to use the finite element method (FEM). FEM typically requires an incidence matrix, which conveys the same information as the connectivity matrix, though it is rarely provided in tensegrity research papers. The study presented in Chapter 5 offers analytical definitions for node, incidence, and connectivity matrices, applicable to t-strut tensegrity prisms in both clockwise and counterclockwise rotations with $t > 3$. These definitions utilize floor and ceiling operators, which have not been widely applied in tensegrity research but offer a convenient method for working with indexes and facilitating subsequent implementation.

2.4 Tensegrity arm

The applications suggested previously are focused on aerospace structures, but civil engineering projects can benefit from tensegrity systems too. Kitipornchai *et al.* (2005) combined a Lamella suspen-dome with a tensegrity base to increase its reduce its member stresses and increase its buckling capacity and stiffness. Also, if properly equipped with actuators, tensegrity structures applied to civil engineering designs can have their strength-to-mass ratio improved by actively resisting external loads (Wang *et al.*, 2021). Rhode-Barbarigos *et al.* (2010) designed a deployable tensegrity footbridge, Veuve *et al.* (2017) developed control commands to accommodate the structure in case of element damages, and Sychterz and Smith (2018) evaluated the impact of ruptured cables on natural frequencies. A deployable tensegrity grid can be used as a solution for sea accessibility (Hrazmi *et al.*, 2021). Skelton *et al.* (2014) and Carpentieri *et al.* (2015) combined fractals (Michell, 1904) and topology optimization to suggest methodologies to develop arch shaped minimal mass tensegrity bridges. Carpentieri *et al.* (2017) applied their procedures to develop a deployable roof, which aims to harvest solar energy on water canals while minimising water losses through evaporation. Temporary bridges are useful to access disaster areas (Yeh *et al.*, 2015), a tensegrity structure that can be conveniently packed and transported is convenient. Also, depending on the local topography, the capacity to generate an arch shape after deployment can be beneficial. The design presented in Chapter 6 could inspire a transportable bridge project because it addresses packing, deploying and arching.

Those features are accomplished by shape transformations, which are calculated through form-finding procedures and can be organized as static and kinematic categories (Tibert; Pellegrino, 2003). Static methodologies seek equilibrium configurations that guarantee a state of self stress in the structure (subject to a set of requirements). A popular example of static methodology is the force density method (Zhang; Ohsaki, 2006). Estrada *et al.* (2006) proposed a numerical procedure that does not require the element lengths as input. It is based on the force density matrix rank and generates new configurations. When the lengths of the members are not initially specified, that procedure is worthy of being considered. Raj and Guest (2006) proposed a method that utilizes symmetry to reduce computational effort. Zhang *et al.* (2014) suggested a form-finding method based on the stiffness matrix (SMFF). Koohestani (2012) converted the form-finding method in an optimization problem and applied a genetic algorithm to solve it. The objective function generates the desired rank on the force density matrix, and the technique determines the force densities by minimising such function. Analytical solutions (Koohestani, 2017) and an approach using nonlinear programming and LU-decomposition of the force density matrix (Koohestani, 2020) have been presented.

Kinematic methods work by keeping the bar lengths constant and minimizing the cable lengths (Tibert; Pellegrino, 2003). The opposite is valid, but it is relatively complex to increase the length of a bar in a robot. The form-finding of a tensegrity structure can be transformed in a constrained minimization problem (Pellegrino, 1986) and solved by nonlinear programming (Ohsaki; Zhang, 2015). When there is a large solution space, nonlinear programming is disadvantageous. Therefore, stochastic techniques have been selected by some researchers. Xu and Luo (2010) used a binary coded genetic algorithm to determine the shape of irregular tensegrity systems. Also, Li *et al.* (2010) presented a Monte Carlo form-finding method and demonstrated it on various tensegrity configurations.

Quadruplex modules (tensegrity prisms with four bars) are stacked to form a deployable class 2 tensegrity tower presented in this thesis. The system deploys from a flat configuration into a tower (first stage) and from a tower into an arch (second stage). The cable lengths are shortened to achieve the shape transformation of the first stage. After fully deployed into a high aspect ratio tower, the cable lengths are changed to form asymmetric modules and generate the arch shape of the second stage. As the modules are asymmetric, form-finding methods that assume symmetry cannot be applied. Also, force density methods may not be advantageous because all bars and many cables keep their lengths constant in both stages. Therefore, the selected strategy to calculate the tensegrity tower is an adapted kinematic method with nonlinear programming. This design contributes to the field because it provides advances in the kinematic methods and suggests a structure that could be applied in engineering projects.

2.5 Tensegrity systems in other fields

Aside from evident applications of tensegrity and tensegrity-membrane systems in physics, architecture and engineering, the features explored in this thesis can be availed in other fields. Double helix DNA structures can be used as struts and single stranded DNA can be used as cables in nanoscale tensegrity prisms. The work developed in (Liedl *et al.*, 2010) shows a three-strut tensegrity prism that deploys by shortening one of their vertical cables, similar to the form-finding procedure suggested in Chapter 6. Also, they assemble a planar tensegrity in the same configuration of a single level of the tensegrity beam studied in Chaper 4.

An equivalent self-assembly property is explored in human anatomy. Collagen is an abundant structural protein, forms the extracellular matrix around most cells, and provides a tensegrity-based structural framework that is continuous with the fascia (Scarr, 2011). Even though its shape is mostly helical, the methodology presented in Chapters 6 and 7 can be adapted to model its packing and deployment steps. Also, tensegrity systems can be integrated with origami structures (Ma *et al.*, 2023; Fonseca *et al.*, 2022). This combines the reach of tensegrity research to the reach of origami systems in studies covering RNA (Poppleton *et al.*, 2023), biomedical (Ahmed *et al.*, 2020) and battery (Song *et al.*, 2014) research.

Apart from the evident applications of tensegrity and tensegrity-membrane systems in physics, architecture, and engineering, the features explored in this thesis can be applied to other fields. Double-helix DNA structures can act as struts, while single-stranded DNA can serve as cables in nanoscale tensegrity prisms. The work in (Liedl *et al.*, 2010) demonstrates a three-strut tensegrity prism that deploys by shortening one of its vertical cables, similar to the form-finding procedure proposed in Chapter 6. They also assemble a planar tensegrity in the same configuration as a single level of the tensegrity beam studied in Chapter 4. An equivalent self-assembly property is explored in human anatomy: collagen, an abundant structural protein, forms the extracellular matrix around most cells and provides a tensegrity-based framework continuous with the fascia (Scarr, 2011). Although its shape is primarily helical, the methodology in Chapters 6 and 7 can be adapted to model its packing and deployment. Additionally, tensegrity systems can be integrated with origami structures (Ma *et al.*, 2023; Fonseca *et al.*, 2022), combining tensegrity research with the potential of origami in studies involving RNA (Poppleton *et al.*, 2023), biomedical applications (Ahmed *et al.*, 2020), and battery (Song *et al.*, 2014) research.

3 PRESTRESSED MEMBRANE

The article entitled "Experimental and numerical analysis of a pre-stressed tensegrity membrane" is presented in this chapter. It is authored by Victor A. S. M. Paiva, Luis H. Silva-Teixeira, Jaime H. Izuka, Paola G. Ramos and Paulo R. G. Kurka and was presented by Prof. Kurka at the 33rd congress of the International Council of the Aeronautical Sciences (ICAS) held in Stockholm (Sweeden) in September 2022. The congress does not hold a copyright on the published papers.

This paper explores the potential of tensegrity-membrane structures in the context of aerospace engineering, where their structural efficiency and shape-shifting capabilities are highly valued. The study focuses on the integration of a stressed membrane within a tensegrity system, which presents challenges in modeling and construction. A triangular-shaped membrane is numerically modeled and experimentally tested under four distinct sets of stresses. The study includes the calculation of natural frequencies, which are validated through image processing of membrane vibration records. These results provide critical insights into the behavior of tensegrity-membrane systems, contributing to the broader understanding and potential applications of these structures.

Chapter 7 contains comments on how this paper relates to the overall objective of this thesis. Additionally, it discusses the potential of the image processing methods in assisting physics and engineering educators.

33RD CONGRESS
OF THE INTERNATIONAL COUNCIL
OF THE AERONAUTICAL SCIENCES
STOCKHOLM, SWEDEN, 4-9 SEPTEMBER, 2022

ICAS 2022 SWEDEN

EXPERIMENTAL AND NUMERICAL ANALYSIS OF A PRE-STRESSED TENSEGRITY MEMBRANE

Victor A. S. M. Paiva[1], Luis H. Silva-Teixeira[1], Jaime H. Izuka[2], Paola G. Ramos[1] & Paulo R. G. Kurka[1]

[1]Universidade Estadual de Campinas, Campinas, Sao Paulo, 13083-970, Brazil
[2]Universidade Estadual de Campinas, Limeira, Sao Paulo, 13484-350, Brazil

Abstract

Tensegrity structures have caught the attention of scientists and aerospace engineers because of their potential, regarding structural efficiency and shape shifting characteristics. Furthermore, some applications require surfaces to perform structural or reflective functions, which motivate the design of tensegrity-membrane systems. Such systems can be challenging in terms of modelling and construction, therefore it is important, in the first place, to analyse the tensioned membrane component of such a tensegrity system. In this study, a triangular shaped membrane is numerically modelled and experimentally tested, under four sets of stresses. Natural frequencies are calculated and validated from image processing of membrane vibration records.

Keywords: membrane; tensegrity; modal; static; ansys

1. Introduction

Tensegrity is a class of pre-stressed structures in which tension provides integrity. The rigid components of a tensegrity structure remain always under compression, while cables and membranes work always under tension [18]. Tensegrity-membrane systems are comprised of membranes, bars and tendons. They belong to the class of flexible multibody structures and can be treated as an extension of tensegrity systems [27]. Tensegrities ideally match the definition of smart structures because they represent a special class of tendon-spatial structures. Their members may perform functions such as sensing, actuating, and feedback controlling simultaneously [16]. Additional advantages of tensegrities over traditional structures are: high structural efficiency and resistance to impact [1], controllable stiffness [2], controllable shape [31], deployability [17] and uniaxial stress of its elements [3].

Also, tensegrity-membrane configurations are generally light weighted and capable of significant shape changes, which enable these novel systems to experience relatively easy folding and unfolding between packed and deployed configurations, if properly controlled [28].

Researchers in aerospace sciences have interest in tensegrity structures. A growth adaptable artificial gravity space habitat based on a tensegrity-membrane structure has been designed by [5]. A tensegrity robot with six bars and 24 cables in an icosahedral shape was suggested by [21], to be used as a space exploration probe. The high resistance to impact of the probe is useful for landing, and the system rolls to explore the terrain, as cables are tension-controlled. Tensegrity-membrane systems can also be used in the exploration of ocean and lakes [4].

The propulsion efficiency of a spacecraft depends on a low ratio of overall mass to solar sail and antennas area. Technological solutions for in-orbit deployable, ultralightweight sail and antenna surfaces are, therefore, in high demand [10].

Traditional space systems are generally designed with rigid support frames. The modification of their configuration requires addition of numerous components, which leads to an increase in weight [27]. The mechanical properties of tensegrity-membrane systems thus, make them promising candidates for lightweight and deployable space structures that can be used in the aerospace industry, such as

space antennas and solar sails. The tensegrity-membrane combination appears as an alternative solution to a pure tensegrity structure ([4], [29] and [10]).
The membrane of the tensegrity system can be covered by a reflective skin, performing structural and reflective functions ([22] and [9]). However, as membrane structures are generally very flexible, there is a need for accurate models to predict their vibration behavior because it has a direct impact on their desired geometric characteristic and efficiency [8]. A methodology that provides an analytical approximation to the behavior of membranes under a certain pre-stress limit is suggested by [20]. An umbrella membrane is modelled in ANSYS by [14] and its behavior is analysed for different sets of rain load. The numerical analysis results are validated with a prototype. Vibration studies of a plane film and an inflatable tube is performed in [6]. Their work compares numerical and experimental results for wet and dry conditions and for different internal pressures of the tube. A long inflatable boom and a triangular plane membrane are modelled in [23] and the numerical results are validated with prototypes. To reduce wrinkling of the triangular membrane, the authors suggest using catenary-shaped edges and compare the stress analysis with a straight edge model. The implementation of catenary edges on membranes is assessed experimentally by [24], analytically by [25] and numerically by [26].
Vibration studies are also useful to detect damage in a structure. A methodology is proposed by [7] to detect local damage in circular and rectangular membranes by combining 3D digital image correlation and Bayesian operational modal analysis. Numerical, analytical and experimental studies of the damped vibration response of a membrane under impact loads are also performed in ([13], [15]) and [11]). Finally, a methodology is suggested by [12] to find the stress level of a membrane from its vibration response to a local impact.
The present work, therefore, contributes to the validation of a pre-stressed membrane model. A finite element model of a membrane is built in the ANSYS platform to analyse the behavior of a pre-stressed tensegrity-membrane structure. Different pre-stressing conditions are simulated and analysed, and a triangular stressed membrane prototype is assembled and experimented to validate the numerical model of the structure.

2. Methodology

A membrane pulled at its vertexes (Figure 1) through cables c_1, c_2 and c_v, develops pre-stresses, and its natural frequencies and modes of vibration are acquired. The triangular shape is convenient because the traction in one cable allows the calculation of the traction in the other two, so the experiment requires traction measurement of only one cable. Four sets of pre-stresses generated by four different forces in c_v are simulated in the commercial software *Ansys Mechanical APDL* and experimentally tested.

2.1 Numerical static analysis

The pre-stresses in the membrane are used to calculate the stiffness for the vibration analysis. Movement constraints in axes X and Y are applied to the vertexes 1 and 2 of the membrane. All nodes in this analysis are constrained to move in the Z direction. The elements LINK180 and SHELL281 are used in the FEM platform to model the cables and the membrane, respectively.

2.2 Numerical vibration analysis

All cables ends are fixed, and the pre-stresses from the static analysis are used to calculate the stiffness. However, these stresses do not contain the forces in c_1 and c_2 because they do not participate in the static analysis. Therefore, the stress in the cables are inserted manually. Movement along the Z-axis is free in the vibration analysis. The INISTATE command is used to store, load, and insert the pre-stresses. With such boundary conditions applied, a numerical modal analysis is performed to estimate the pre-stressed structure's natural frequencies and mode shapes. Figures 2a and 2b show the static and modal analyses (respectively) of the second set of pre-stresses, as an example. Modes of vibration associated with wrinkling of the membrane (Figure 3) and rigid body modes were discarded.

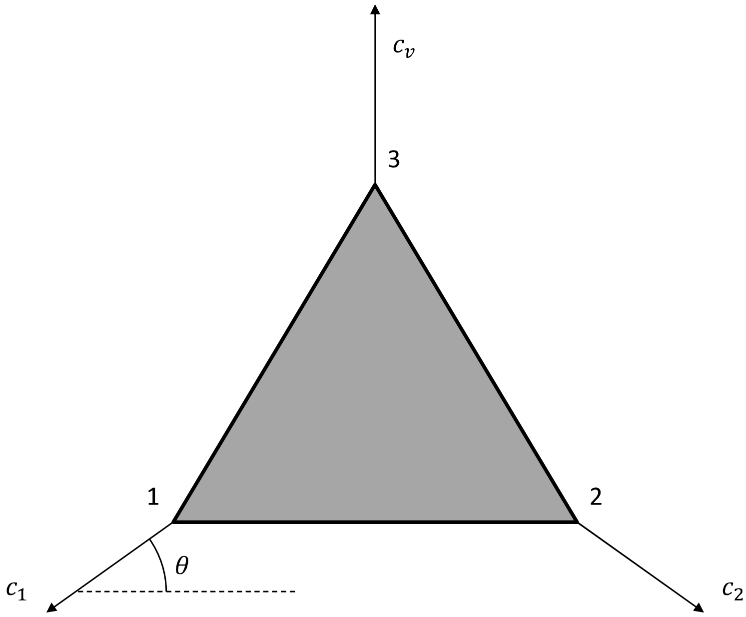

Figure 1 – Membrane configuration.

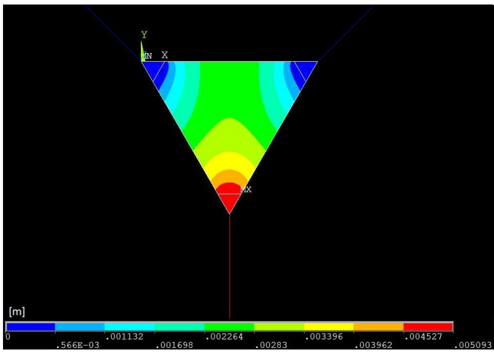

(a) Static analysis.

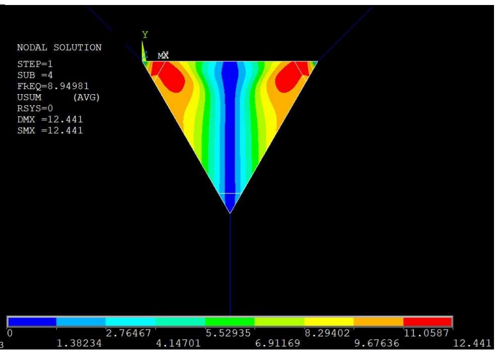

(b) Modal analysis.

Figure 2 – Numerical results for the second set of pre-stresses.

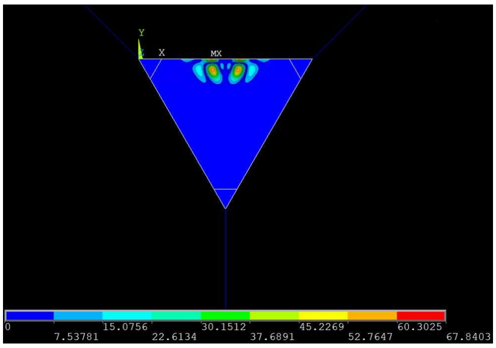

Figure 3 – Example of a mode of vibration associated with wrinkling.

Materials properties and geometrical parameters for simulation are indicated in Table 1. The influence of air displacement in the vibration of the membrane can be represented numerically by increasing the material density to $3500 kg/m^3$ (actual density of the material is $1350 kg/m^3$) [30].

Table 1 – Simulation parameters.

Young modulus	2.5 MPa
Density	3500 kg/m^3
Membrane thickness	0.43 mm
Membrane side	0.17 m
c_1	0.01 m
c_2	0.08 m
c_v	0.08 m
θ	$\pi/4$ rad

3. Experimental procedure

Similarly to the numerical model, the ends of the cables are fixed. However, one of them is fixed to a hook scale (10 g resolution) that indicates the traction in that cable (Figure 4). This measured value is the input for the numerical analyses. The membrane is made of rubber, and the nylon cables have a diameter of $0.4mm$.

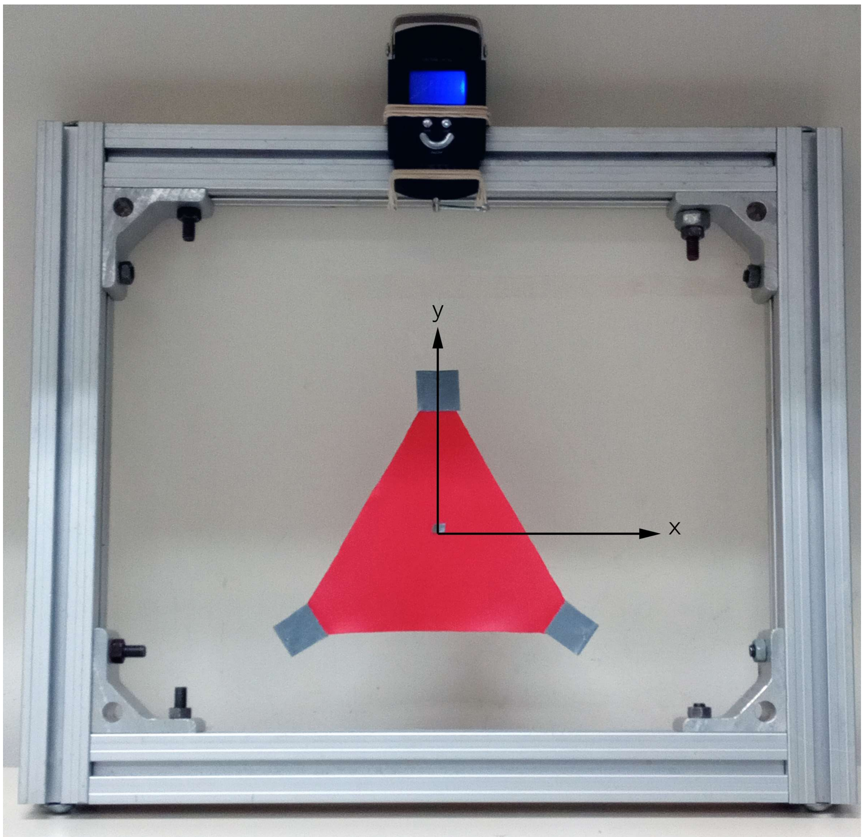

Figure 4 – Prototype.

An impulse is applied perpendicular to the membrane, and a $30fps$ camera, parallel to the XY plane of the membrane surface, records its vibration as shown in Figure 4, . From this position, the membrane is seen from its side and the vibration happening in the Z direction is tracked by the vertexes and by a marked point in the middle of the prototype. An image processing software acquires the position of these markers over time, the data is treated, and a Fourier transform is applied to obtain the response in the frequency domain. Each pre-stress set is analysed multiple times, its specters are normalised to unity, and a mean curve is plotted with a thicker line (Figures 5a, 5b, 5c and 5d).

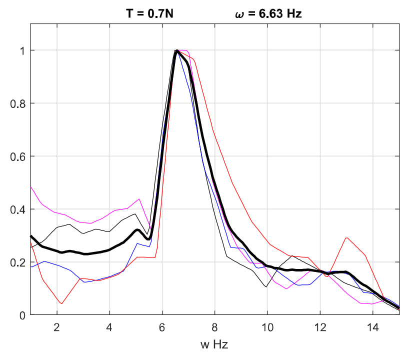

(a) $c_v = 0.7N$.

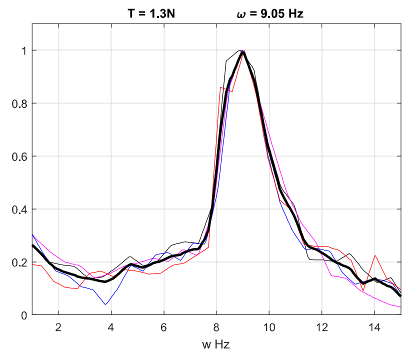

(b) $c_v = 1.3N$.

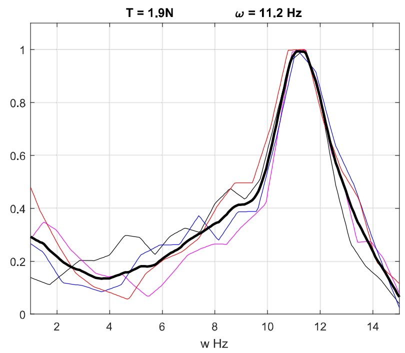

(c) $c_v = 1.9N$.

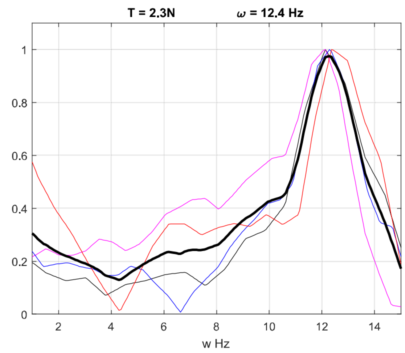

(d) $c_v = 2.3N$.

Figure 5 – Modal analysis for different sets of membrane stress.

4. Results

Results from the experiments are collected and organized along with the numerical outputs (table 2). The first mode of vibration is the highest energy one and is most relevant to the membrane dynamics. The experimental analysis compares the measured frequencies of the first mode with those obtained numerically. Spurious modes [19] were discarded.

Table 2 – Natural frequencies.

c_v	Experimental	Numerical	Error
0.7N	6.63Hz	6.95Hz	3.17%
1.3N	9.05Hz	8.95Hz	2.55%
1.9N	11.2Hz	10.89Hz	4.33%
2.3N	12.4Hz	13.24Hz	5.02%

5. Conclusions

The numerical model of the membrane of a tensegrity structure is implemented. Simulations and experimental tests on a prototype are performed under different pre-stressing conditions. Higher stresses generate higher natural frequencies, as expected. The obtained results are compared and errors between numerical and experimental procedures are not greater than 5.02%, which indicates good agreement between model and prototype. Furthermore, the uncertainties of the simulation and experimental procedures do not invalidate the proposed methodologies. It indicates that the numerical model of the membrane can be successfully used and integrated with previously validated numerical models of tensegrity structures. Future steps involve building and modelling a membrane with catenary edges and combining it with a tensegrity to assemble a tensegrity-membrane system.

6. Contact Author Email Address

mailto: v140962@dac.unicamp.br and kurka@unicamp.br.

7. Copyright Statement

References

[1] Adrian K Agogino, Vytas SunSpiral, and David Atkinson. Super ball bot-structures for planetary landing and exploration. 2018.

[2] N. Bel Hadj Ali and I.F.C. Smith. Dynamic behavior and vibration control of a tensegrity structure. *International Journal of Solids and Structures*, 47(9):1285–1296, 2010.

[3] Nasseradeen Ashwear and Anders Eriksson. Natural frequencies describe the pre-stress in tensegrity structures. *Computers & structures*, 136:162–171, 2014.

[4] Christine A Gebara, Kalind C Carpenter, and Anna Woodmansee. Tensegrity ocean world landers. In *AIAA Scitech 2019 Forum*, page 0868, 2019.

[5] Raman Goyal, Tyler Bryant, Manoranjan Majji, Robert E Skelton, and Anthony Longman. Design and control of growth adaptable artificial gravity space habitat. In *AIAA SPACE and Astronautics Forum and Exposition*, page 5141, 2017.

[6] Yu Hu, Wujun Chen, Yufeng Chen, Daxu Zhang, and Zhenyu Qiu. Modal behaviors and influencing factors analysis of inflated membrane structures. *Engineering Structures*, 132:413–427, 2017.

[7] Yujia Hu, Weigong Guo, Weidong Zhu, and Yongfeng Xu. Local damage detection of membranes based on bayesian operational modal analysis and three-dimensional digital image correlation. *Mechanical Systems and Signal Processing*, 131:633–648, 2019.

[8] S. Kukathasan and Sergio Pellegrino. Vibration of prestressed membrane structures in air. In *43RD AIAA/ASME/ASCE/AHS/ASC STRUCTURES, STRUCTURAL DYNAMICS, AND MATERIALS CONFERENCE*, 2002.

[9] P Kurka, V Paiva, L Teixeira, J Izuka, and P Gonzalez. Dynamic behavior and vibration analysis of tensegrity-membrane structures. In *Proceedings of ISMA*, 2018.

[10] M. Leipold, H. Runge, and C. Sickinger. Large sar membrane antennas with lightweight deployable booms. In *28th ESA Antenna Workshop on Space Antenna Systems and Technologies, ESA/ESTEC*, 2005.

[11] Dong Li, Zhou-Lian Zheng, Rui Yang, and Peng Zhang. Analytical solutions for stochastic vibration of orthotropic membrane under random impact load. *Materials*, 11(7):1231, 2018.

[12] Chang-Jiang Liu, Michael D Todd, Zhou-Lian Zheng, and Yu-You Wu. A nondestructive method for the pretension detection in membrane structures based on nonlinear vibration response to impact. *Structural Health Monitoring*, 17(1):67–79, 2018.

[13] Changjiang Liu, Xiaowei Deng, Jian Liu, and Zhoulian Zheng. Impact-induced nonlinear damped vibration of fabric membrane structure: theory, analysis, experiment and parametric study. *Composites Part B: Engineering*, 159:389–404, 2019.

[14] Changjiang Liu, Fan Wang, Ling He, Xiaowei Deng, Jian Liu, and Yuyou Wu. Experimental and numerical investigation on dynamic responses of the umbrella membrane structure excited by heavy rainfall. *Journal of Vibration and Control*, 27(5-6):675–684, 2021.

[15] Changjiang Liu, Fan Wang, Jian Liu, Xiaowei Deng, Zuoliang Zhang, and Haibing Xie. Theoretical and numerical studies on damped nonlinear vibration of orthotropic saddle membrane structures excited by hailstone impact load. *Shock and Vibration*, 2019, 2019.

[16] Cornel Sultan Mohammed R. Sunny and Rakesh K. Kapania. Optimal energy harvesting from a membrane attachedto a tensegrity structure. *AIAA*, 52(2):307–19, 2014.

[17] V Paiva, P Kurka, and JH Izuka. Kinematics and dynamics of tensegrity structure in expansion. In *31st Congress of the International Council of the Aeronautical Sciences*, page 10, 2018.

[18] Robert E. Skelton and Mauricio de Oliveira. *Tensegrity Systems*. Springer US, 2009.

[19] Din Sun, John Manges, Xingchao Yuan, and Zoltan Cendes. Spurious modes in finite-element methods. *IEEE Antennas and Propagation Magazine*, 37(5):12–24, 1995.

[20] Mohammed R Sunny, Rakesh K Kapania, and Cornel Sultan. Solution of nonlinear vibration problem of a prestressed membrane by adomian decomposition. *AIAA journal*, 50(8):1796–1800, 2012.

[21] Vytas SunSpiral, Adrian Agogino, and David Atkinson. Super ball bot-structures for planetary landing and exploration, niac phase 2 final report. 2015.

[22] LH Teixeira, JH Izuka, P Gonzalez, and P Kurka. A numerical analysis of the dynamics of a tensegrity-membrane structure. In *31st Congress of the International Council of the Aeronautical Sciences*, page 9, 2018.

[23] Jianzheng Wei, Ruiqiang Ma, Yufei Liu, Jianxin Yu, Anders Eriksson, and Huifeng Tan. Modal analysis and identification of deployable membrane structures. *Acta Astronautica*, 152:811–822, 2018.

[24] Wesley Wong and Sergio Pellegrino. Wrinkled membranes i: experiments. *Journal of Mechanics of Materials and Structures*, 1(1):3–25, 2006.

[25] Wesley Wong and Sergio Pellegrino. Wrinkled membranes ii: analytical models. *Journal of Mechanics of Materials and Structures*, 1(1):27–61, 2006.

[26] Wesley Wong and Sergio Pellegrino. Wrinkled membranes iii: numerical simulations. *Journal of Mechanics of Materials and Structures*, 1(1):63–95, 2006.

[27] Shu Yang and Cornel Sultan. A comparative study on the dynamics of tensegrity-membrane systems based on multiple models. *International Journal of Solids and Structures*, 113:47–69, 2017.

[28] Shu Yang and Cornel Sultan. Lpv control of a tensegrity-membrane system. *Mechanical Systems and Signal Processing*, 95:397–424, 2017.

[29] Shu Yang and Cornel Sultan. Deployment of foldable tensegrity-membrane systems via transition between tensegrity configurations and tensegrity-membrane configurations. *International Journal of Solids and Structures*, 160:103–119, 2019.

[30] Leyland G Young, Suresh Ramanathan, Jiazhu Hu, and P Frank Pai. Numerical and experimental dynamic characteristics of thin-film membranes. *International Journal of Solids and Structures*, 42(9-10):3001–3025, 2005.

[31] J.Y. Zhang and M. Ohsaki. Adaptive force density method for form-finding problem of tensegrity structures. *International Journal of Solids and Structures*, 43(18):5658 – 5673, 2006.

4 TENSEGRITY BEAM

The article entitled “A dynamical model for the control of a guyed tensegrity beam under large displacements” (Kurka *et al.*, 2024) is presented in this chapter. It is authored by Victor A. S. M. Paiva, Luis H. Silva-Teixeira, Jaime H. Izuka, Paola G. Ramos and Paulo R. G. Kurka and is presented with permission from the American Society of Mechanical Engineering ASME (Appendix C). The paper has been published in the Journal of Mechanisms and Robotics, vol. 16, issue 9, 2024. DOI: 10.1115/1.4064259.

This paper addresses a gap in the existing literature on tensegrity systems, where most studies either overlook the possibility of large static deformations or rely on complex and lengthy methods to determine system dynamics. In contrast, this work introduces a straightforward methodology to identify the dynamic characteristics of a guyed tensegrity beam structure, specifically under conditions of large deformations. The method, based on a low-order, adaptive, nonlinear finite element model with pre-stressed components, is applied to both numerical and experimental models of a planar tensegrity beam. The study combines image processing and accelerometer data to extract the experimental natural frequencies of the structure, which are then compared to numerical results. Additionally, Prony’s method is employed to estimate damping, and a numerical control strategy is developed using the dynamical model of the structure.

Chapter 7 contains comments on the results presented in this paper that relate to the overall objective of this thesis. It also reaffirms the application of image processing techniques in educational environments for engineering and physics. Appendix presents the definition of the Kronecker product operator $\otimes$ shown in sections *2.1 Static Analysis of Tensegrity Structures* and *3.4 Relevance of the Force Density Term*.

The MATLAB scripts used in the nonlinear static analysis are publicly available at <https://github.com/FictorP/Tensegrity/tree/main/beam/static>, and in the modal analysis at <https://github.com/FictorP/Tensegrity/tree/main/beam/modal>.

ASME Journal of Mechanisms and Robotics
Online journal at:
https://asmedigitalcollection.asme.org/mechanismsrobotics

Paulo R. G. Kurka
Faculty of Mechanical Engineering,
Universidade Estadual de Campinas,
Mendeleyev Street,
13083-860 Campinas, São Paulo, Brazil
e-mail: kurka@unicamp.br

Victor A. S. M. Paiva[1]
Faculty of Mechanical Engineering,
Universidade Estadual de Campinas,
Mendeleyev Street,
13083-860 Campinas, São Paulo, Brazil
e-mail: v140962@dac.unicamp.br

Luis H. Silva-Teixeira
Faculty of Mechanical Engineering,
Universidade Estadual de Campinas,
Mendeleyev Street,
13083-860 Campinas, São Paulo, Brazil
e-mail: luishsteixeira@gmail.com

Paola G. Ramos
Faculty of Mechanical Engineering,
Universidade Estadual de Campinas,
Mendeleyev Street,
13083-860 Campinas, São Paulo, Brazil
e-mail: pagora00@gmail.com

Jaime H. Izuka
Faculty of Applied Sciences,
Universidade Estadual de Campinas,
Pedro Zaccaria Street,
13484-350 Limeira, São Paulo, Brazil
e-mail: jhizuka@unicamp.br

A Dynamical Model for the Control of a Guyed Tensegrity Beam Under Large Displacements

Most studies regarding models of tensegrity systems miss the possibility of large static deformations or provide elaborate and lengthy solutions to determine the system dynamics. Contrarily, this work presents a straightforward methodology to find the dynamic characteristics of a guyed tensegrity beam structure, allowing the application of vibration control strategies in conditions of large deformations. The methodology is based on a low-order, adaptive, nonlinear finite element model with pre-stressed components. The method is applied to numerical and experimental models of a class 2 tensegrity structure with a high length-to-width aspect ratio. Image processing and accelerometer data are combined to extract the experimental natural frequencies of the structure, which are compared to numerical results. Prony's method is applied to estimate damping, and a numerical control strategy is employed using the dynamical model of the structure.
[DOI: 10.1115/1.4064259]

Keywords: *nonlinear statics, cable-driven, tensegrity, dynamics*

1 Introduction

Tensegrity structures became popular in 1948 by Snelson as an art form. Fuller and Applewhite recognized their engineering value and created the term tensegrity as a contraction of "tensional" and "integrity" [1]. Tensegrity structures contain compressive discontinuous parts (struts) and continuous tensile parts (cables) connected with ball joints (pin-joint) [2]. The rigidity of tensegrity systems results from a state of self-stressed equilibrium between cables under tension and compressed rigid bodies [3]. Generally, the self-weight of the cables can be disregarded [4]. However, recent articles have explored factors such as friction and contact between struts [5,6]. Tensegrities are considered class one if the bars do not touch each other. Otherwise, the class is given by the maximum number of struts sharing a common node. A fundamental aspect of tensegrities is the uniaxial stress property of the components: cables and bars must be under tension and compression, respectively [7]. This property contributes to an optimized choice of materials and geometry, focusing on resistance to traction in the cables and compression (and buckling) in the bars [3].

Tension structures, such as cable nets, membrane structures, and tensegrity domes, offer significant advantages over conventional structures, such as steel structures [8]. Due to their design, tensegrities can serve as the foundation of lightweight and strong mechanical structures using less material [9] when designed efficiently [10]. Among various traditional approaches, the tensegrity concept is one of the most promising for active and deployable structures [11–13]. For deployment, the disjointed struts provide a crucial advantage of the tensegrity concept, enabling a compact package [14]. In addition, they may integrate structural and control systems since the elastic components can carry both sensing and actuating functions [15]. Also, a small amount of energy is sufficient to control the shape of tensegrity structures, which is advantageous for active control [16]. Tensegrity structures also exhibit excellent shape change capability and shock resistance. These features can be beneficial in mechanisms, robots, and space exploration rovers [17–20]. The concept and features of tensegrities are valuable in high technology and aerospace structural applications [21].

[1]Corresponding author.

Contributed by the Mechanisms and Robotics Committee of ASME for publication in the Journal of Mechanisms and Robotics. Manuscript received August 21, 2023; final manuscript received December 6, 2023; published online February 1, 2024. Assoc. Editor: Med Amine Laribi.

Recently, tensegrities have received significant attention from scientists and engineers in fields such as architecture, civil engineering [22], biology [23], and in the construction of dampers [24], shape-shifting structures, such as twisting wings [25] and ocean wave energy harvesting mechanisms [26]. Many form-finding methods and topology designs have been developed recently [27–33] along with the introduction of new tensegrity families [34,35]. The kinematic and dynamic behaviors of tensegrities have been investigated in works such as those in Refs. [5,6,9,11,14,36,37]. Particular concerns in these studies include the magnitudes of structural displacements, which can be large, even if the deformation of individual members are small [38]. Slack cables also represent a relevant problem, especially when such elements transition from tensioned to slack states in tensegrity mechanisms, generating roughness in the system movements [39,40]. The literature shows a large number of works related to the nonlinear analysis of tensegrity systems. Kebiche et al. [38] developed a calculation method for tensegrity systems taking into account geometrical nonlinearities. They used a total Lagrangian formulation to determine the tangent matrix and the internal stress vector for a four-strut tensegrity system subjected to traction, compression, bending, and torsion loading. They also studied a multi-cell beam under traction. The results reveal nonlinear behavior due to flexibility, with rigidity increasing with the external load and self-stress level, except in compression loads. The mechanical behavior was observed to be similar to anisotropic materials, where the displacements response depends on the orientation of the loads. Tran and Lee [41] also presented a numerical method for large deflections, including both geometric and material nonlinearities. They utilized total Lagrangian and updated Lagrangian formulation to treat the geometrical nonlinearity, while material nonlinearity was handled through the elastoplastic stress–strain relationship. Their proposed method calculates responses of the quadruplex unit module, double layer quadruplex grid, and five-quadruplex module beam under external loads. The results indicate that the stiffness of tensegrity structures increases with the self-stress level. In the quadruplex unit module, the stretching stiffness dominates over bending. The bending strength capacity of the double layer quadruplex tensegrity grid is not significantly affected by the self-stress level. The updated Lagrangian formulation is recommended for the large deflection analysis of tensegrity structures. Zhang et al. [42] developed an efficient numerical method capable of capturing mechanical responses of tensegrity structures with very large and highly nonlinear deformations under different conditions. This method is applicable for all types of tensegrities subjected to either external or internal applied actuation.

The literature is limited in terms of experimental results on high aspect ratio tensegrity beams. This work extends the available collection to assist the community in validating new static and dynamic models. Additionally, considering the dynamical analysis works investigated, there is a knowledge gap regarding vibration control of tensegrity structures with fast and large geometry changes. Most kinematic and kinetic models of tensegrities found in the literature employ lengthy and time consuming adaptive or relaxation techniques to evolve from the different conditions of large displacement movements. Implementing control strategies based on these techniques can be challenging. In contrast, the present work proposes simpler manners to build a dynamic model of tensegrity structures that can be assembled in real-time, yielding sufficient parameters to allow the vibration control of the structure at any stage of its present large displacement movement. The proposed methodology is based on the superimposition of a low-order, adaptive, nonlinear finite element model with pre-stressed components onto the nodes of the statically deformed structure. The node positions of the structure, then, are determined by a polynomial function obtained previously from static analysis data, undergoing the workspace of possible large deformations. To verify and validate the proposed analysis technique, the numerical model and a physical prototype of a planar tensegrity guyed beam are utilized. The dynamic characteristics under different operational conditions are also investigated.

Furet and Wenger [43] also studied the kinematics and actuation of a planar tensegrity manipulator with two levels (2-X) and observed that friction can be relevant to the dynamics of the mechanism, which should be added in future reports. Even though the results from a two-level tower can be extrapolated to a certain extent, the behavior might change significantly in higher aspect ratios. The prototype presented in this work features six levels (6-X), and the damping ratios are estimated. There is limited data available in the literature regarding these kinds of analyses on tensegrity guyed beams. The tensegrity structure presented in this paper counts on comparisons to the studies presented in Refs. [44,45], which focused on a solid, long, guyed beam under large displacements. However, the present model was observed to behave similarly. Furthermore, the dynamic model developed in this work is used to apply the vibration control procedure shown in Ref. [45] for long beams, which has been verified experimentally [46]. An adaptation of the dead-band controller shown in Ref. [47] for tensegrity systems is another viable option.

2 General Modeling Methodology

2.1 Static Analysis of Tensegrity Structures. The geometry of a tensegrity structure is defined by the node and connectivity matrices [48]. The ith node coordinates are described by a position vector $\mathbf{n_i}$. A node matrix $\mathbf{N}$ containing all b nodes of the structure is defined (Eqs. (1) and (2)). The connectivity $\mathbf{c_k}$ of the kth member joining nodes i and j is given by Eq. (3), where $\mathbf{e_i}$ is a vector with a length of b, filled with zeros and containing 1 in the ith position. The connectivity matrix is thus assembled (Eq. (4)).

$$\mathbf{n_i} = \begin{bmatrix} x_i \\ y_i \end{bmatrix} \tag{1}$$

$$\mathbf{N} = \begin{bmatrix} \mathbf{n_1 n_2} \cdots \mathbf{n_b} \end{bmatrix} \tag{2}$$

$$\mathbf{c_k} = \mathbf{e_i} - \mathbf{e_j} \tag{3}$$

$$\mathbf{C}^T = \begin{bmatrix} \mathbf{c_1 c_2} \cdots \mathbf{c_b} \end{bmatrix} \tag{4}$$

The member vectors $\mathbf{m_k}$ represent the h members of the structure in the members matrix $\mathbf{M}$, which is obtained from the node and connectivity matrices (Eq. (5)).

$$\mathbf{M} = \mathbf{N}\mathbf{C}^T = \begin{bmatrix} \mathbf{m_1} & \mathbf{m_2} & \cdots & \mathbf{m_h} \end{bmatrix} \tag{5}$$

Finally, the stiffness matrix $\mathbf{K_k}$ of a member k can be defined (Eqs. (6) and (7)) as

$$\mathbf{K_k} = \mathbf{c_k}\mathbf{c_k}^T \otimes \mathbf{L_k} \tag{6}$$

where

$$\mathbf{L_k} = s_k\left(\mathbf{I} - \frac{\mathbf{m_k}\mathbf{m_k}^T}{\|\mathbf{m_k}\|^2}\right) + K_B\frac{\mathbf{m_k}\mathbf{m_k}^T}{\|\mathbf{m_k}\|^2} = \mathbf{K_\Sigma} + \mathbf{K_\phi} \tag{7}$$

The term $s_k = f_k/l_k$ is the force density of a member and $K_B = E_kA_k/l_k$ is the linear elastic stiffness for bars. Therefore, the stiffness matrix $\mathbf{K_k}$ is composed of the pre-stress $\mathbf{K_\Sigma}$ and material $\mathbf{K_\phi}$ components. Terms f_k and l_k represent, respectively, the normal force and length of the kth member.

The symbol $\otimes$ in Eq. (6) indicates a Kronecker product. As $\mathbf{c_k}\mathbf{c_k}^T$ is $b \times b$ and $\mathbf{L_k}$ is 2×2 (in a planar system), the product $\mathbf{c_k}\mathbf{c_k}^T \otimes \mathbf{L_k}$ is $2b \times 2b$, the same dimensions as the global stiffness matrix $\mathbf{K_G}$, which is assembled by the simple sum of all element stiffness matrices $\mathbf{K_k}$. Finally, for a given load vector $\mathbf{f}$, the displacements $\mathbf{u}$ are calculated as

$$\mathbf{u} = \mathbf{K_G}^{-1}\mathbf{f} \tag{8}$$

Static environmental loads can be introduced into the load vector $\mathbf{f}$, while temperature loads can be introduced directly into the pre-stress component $\mathbf{K_\Sigma}$ as the effect of thermal expansion.

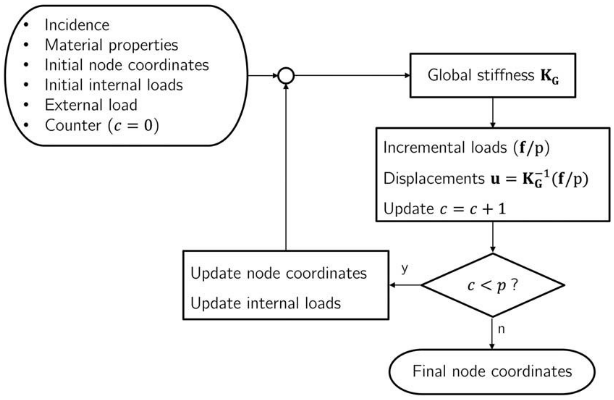

Fig. 1 Flowchart of the incremental loads algorithm adapted to tensegrity structures

2.2 Nonlinear Static Analysis. The method described in the previous section is appropriate for small displacements, but can be adapted to assess behavior under large deformations. The total load, which causes large displacements, must be applied in small increments to satisfy the small deformations assumption in all steps, resembling the strategy used in Ref. [49]. The intensity of the total force $\mathbf{f}$ is divided by the number of steps p, transforming one nonlinear analysis into p linear analyses [50,51]. Material properties E and ρ, cross-sectional areas A, and incidences are assumed to be constant during all steps of the analysis.

Node coordinates $\mathbf{N}$ and internal stresses σ have to be updated at every step according to the new displacements, as shown in Fig. 1. The internal loads affect the pre-stress component $\mathbf{K_\Sigma}$ of the stiffness matrix $\mathbf{K_k}$. The force density s_k is related to the internal stresses σ of the deformed members of the tensegrity structure by the relation in Eq. (9).

$$s_k = \frac{f_k}{l_k} = \frac{\sigma_k A_k}{l_k} \tag{9}$$

For efficiency purposes, the incremental loads can be calculated in advance if the system does not generate significant changes in the direction of external loads. But, in many applications, the large deformations of the structure generate relevant impacts on the external loads orientations. Therefore, the algorithm suggests calculating the incremental loads vector at every step.

The Euler's incremental loads procedure is not recommended for solving models containing a high number of elements due to its relatively lower efficiency when compared to more sophisticated methodologies. However, models with few elements can be calculated in an adequate simulation time. Additionally, the procedure is relatively simple to implement and combine with the methodology that assumes small displacements.

Still, real-time controllers may need to convert an external load into node coordinates nearly instantaneously. To provide a quick access, resultant node positions from a large set of analyses are associated with their respective external loads and fitted using a fourth-order polynomial. Also, the final lf and starting lo lengths of a determined cable are used to represent the external load in a dimensionless measure $c = lf/lo$. The polynomials are expressed in matrix form (Eq. (10)), where $\mathbf{X}$ and $\mathbf{Y}$ represent the coefficient matrices, and $\mathbf{r_n}$ is the position vector of node n in x ($\mathbf{i}$) and y ($\mathbf{j}$) coordinates. Furthermore, the image of the polynomials for $0 < c < 1$ can be interpreted as the workspace of the mechanism joints, which adds to the work developed in Ref. [52].

$$\begin{bmatrix} \mathbf{r_1} \\ \mathbf{r_2} \\ \vdots \\ \mathbf{r_b} \end{bmatrix} = \mathbf{X} \begin{bmatrix} c^4 \\ c^3 \\ c^2 \\ c \\ 1 \end{bmatrix} \mathbf{i} + \mathbf{Y} \begin{bmatrix} c^4 \\ c^3 \\ c^2 \\ c \\ 1 \end{bmatrix} \mathbf{j} \tag{10}$$

2.3 Modal Analysis. Any set of node coordinates, material properties, and rest lengths provides enough information to define the stiffness and mass matrices. Once the final static positions are calculated, the force density in each cable is obtained by comparing their final and natural lengths, and the stiffness matrix is determined as shown in Eq. (6). The total mass q is assumed to be equally distributed within the w bars, and first-order shape functions are used to calculate each element mass matrix $\mathbf{H_k}$ (Eq. (11)).

$$\mathbf{H_k} = \frac{q/w}{6} \begin{bmatrix} 2 & 0 & 1 & 0 \\ 0 & 2 & 0 & 1 \\ 1 & 0 & 2 & 0 \\ 0 & 1 & 0 & 2 \end{bmatrix} \tag{11}$$

The global mass matrix $\mathbf{H_G}$ is the superposition of the element mass matrices $\mathbf{H_k}$. The natural frequencies ω and modes of vibration $\mathbf{d}$ are extracted from the solutions of the eigenvalue problem (Eq. (12)).

$$(\mathbf{K_G} - \omega^2 \mathbf{H_G})\mathbf{d} = 0 \tag{12}$$

2.4 Damping Parameters. The tensegrity dynamics can be represented by the matrix equation (13):

$$\mathbf{H\ddot{x}} + \mathbf{D\dot{x}} + \mathbf{Kx} = \mathbf{f} \tag{13}$$

where $\mathbf{D}$ is the damping matrix and can be represented as proportional to mass and stiffness (Eq. (14)). The proportional damping assumption has to be taken carefully in tensegrity systems [53,54]. Numerical results (Fig. 9) show that the first two natural frequencies are sufficiently separated and the dynamic study focuses on them. Additionally, the experimental procedures considered impulse excitation instead of harmonic. These criteria do not guarantee that a proportional damping model will be accurate, but suggest that the assumption can lead to reasonable results. This hypothesis is assumed subject to a second inspection in the results section.

$$\mathbf{D} = \alpha \mathbf{H} + \beta \mathbf{K} \tag{14}$$

To reduce the order of Eq. (13), an equivalent system (Eq. (15)) can be defined and further replaced by the matrix equation (16) [55].

$$\begin{cases} \mathbf{H\ddot{x}}(t) + \mathbf{D\dot{x}}(t) + \mathbf{Kx}(t) = \mathbf{f}(t) \\ \mathbf{H\dot{x}}(t) - \mathbf{H\dot{x}}(t) = \mathbf{0} \end{cases}$$
$$\begin{bmatrix} \mathbf{0} & \mathbf{H} \\ \mathbf{H} & \mathbf{0} \end{bmatrix} \begin{Bmatrix} \mathbf{\dot{x}}(t) \\ \mathbf{\ddot{x}}(t) \end{Bmatrix} + \begin{bmatrix} \mathbf{K} & \mathbf{C} \\ \mathbf{0} & -\mathbf{H} \end{bmatrix} \begin{Bmatrix} \mathbf{x}(t) \\ \mathbf{\dot{x}}(t) \end{Bmatrix} = \begin{Bmatrix} \mathbf{f}(t) \\ \mathbf{0} \end{Bmatrix} \tag{15}$$

$$\rightarrow \mathbf{G\dot{z}}(t) + \mathbf{Qz}(t) = \mathbf{f}'(t) \tag{16}$$

Also, an optimization procedure can be used to estimate the proportional damping parameters α (geometry related) and β (material and joints associated). The cost function (J) of the optimization problem that has to be minimized is presented in Eq. (17):

$$\begin{cases} \text{minimize} & J = \frac{\sum_{d=1}^{D} (\xi_{d\text{num}} - \xi_{d\text{exp}})^2}{D} \\ \text{subject to} & \alpha \geq 0 \\ & \beta \geq 0 \end{cases} \tag{17}$$

where d corresponds to the vibration mode, D is the total number of modes, and ξ_{num} and ξ_{exp} are the numerical and experimental damping ratios, respectively.

To calculate the cost function J, the number of numerical damping ratios must match the number of experimental damping ratios. Therefore, a model order reduction is performed to achieve a second-order state-space model. Minimizing J is equivalent to finding α and β that generate numerical damping ratios ξ_{num} as close as possible to the experimental damping ratios ξ_{exp}.

2.5 Control. To assess the control behavior of the vibrating structure, a numerical simulation is performed. The mass $\mathbf{H}$, stiffness

K, and damping **D** matrices of the tensegrity beam model are used in the implementation of a control technique. The numerical H_∞ control strategy presented in Ref. [45] is replicated, with a single motor acting on the structure. The external load vector $\mathbf{f}(t)$ in Eq. (13) can be expressed as a combination of disturbance and actuator terms (Eq. (18)), where **B** and **b** stand for disturbance matrix and force input vector, while $\mathbf{w}(t)$ and $u(t)$ are the disturbance and actuator forces, respectively. Transient environmental conditions, such as wind loads, can be incorporated into the disturbance term.

$$\mathbf{f}(t) = \mathbf{B}\mathbf{w}(t) + \mathbf{b}u(t) \tag{18}$$

The controller aims to add active damping and minimize the system's highest singular value. Weight functions are employed to focus the vibration suppression in the frequency range close to the dominant frequency. In this approach, performance, actuator signal, disturbance, and noise weight functions are applied, connected to the model, and the *hinfsyn* MATLAB function is used. Their filter gains must be adjusted to minimize the H_∞ norm, thereby increasing the system's robustness.

3 Guyed Tensegrity Beam Model

3.1 Numerical Procedures. A planar tensegrity beam with six sections, as shown in Fig. 2, is studied in this paper. Thick lines represent bars and thin lines stand for the tendons. The maximum number of rigid bodies connected by the same node is two. Therefore, it is a class 2 tensegrity. A cable pulls the tip toward a fixed point located close to the base and causes large deformations in the structure, following the studies presented by Holland et al. [56] and Kurka et al. [45], but with a guyed tensegrity instead of a long beam. The large deformations require a nonlinear static study. Additionally, the high aspect ratio suggests low frequencies and motivates a vibration analysis.

The numerical model was implemented under the following assumptions:

- The structure is composed of 30 elements (12 bars and 18 cables) and 14 nodes.
- Bars and cables are linearly elastic and one-dimensional elements.
- The total mass of the structure is attributed to the bars.
- Damping is included in the joints and assumed to be proportional to mass and stiffness.
- Gravity is included. The self-weight is inserted as a load.

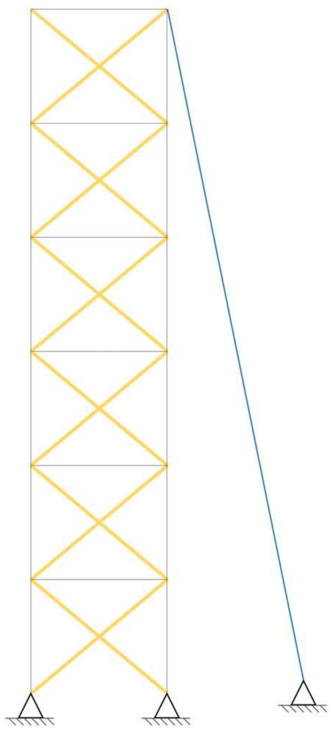

Fig. 2 Schematics of the studied structure

Rubber bands are applied as cables because their natural length is shorter than the starting distance between nodes. Therefore, they begin the experiment under tension and bear a larger displacement before becoming slack. Additionally, friction in the joints was not considered in the static analysis because it mostly depends on relative motion.

The load changes its direction during the analysis. As the top node moves while the base does not, the guying cable varies its orientation. Therefore, the force has to be adjusted in each step of the incremental loads procedure. Despite the relatively low efficiency of the incremental loads technique, in this study, all 30 members can be represented by a single element each, leading to a very low computational cost in each iteration. To conveniently access the static analysis results, the node positions are associated with the relative length $c = lf/lo$ of the pulling cable through a polynomial fit. Base nodes remain fixed, as their coordinates do not vary under different levels of c. The node coordinates matrix (which can be quickly built from a given pulling cable relative length c) provides enough information to assemble the mass and stiffness global matrices.

The damping global matrix is required to obtain a complete dynamic model of the structure. The system poles λ_d for each d mode are obtained from experimental responses using Prony's method (as described in Ref. [55]) and using Eq. (19) as a fitting function.

$$ft(t) = \sum_{d=0}^{D} P_d e^{\lambda_d} \tag{19}$$

where P_d is the amplitude, and D is the number of modes.

The damping ratio ξ_d for each d mode is obtained from Eq. (20). These damping ratios are used to estimate the damping matrix **D** through an optimization procedure (Eq. (17)).

$$\lambda_d = -\xi_d\omega_d + i\Omega_d = -\xi_d\omega_d + i\left(\omega_d\sqrt{1-\xi_d^2}\right) \tag{20}$$

3.2 Experimental Procedures. The prototype is built with 150 mm 3D-printed bars and rubber bands as cables, forming a class 2 tensegrity. Each bar is composed of two strips that entwine the strips of its pair (Fig. 4), minimizing displacements in depth and increasing the critical buckling load, which could be problematic in planar tensegrity systems [57]. Also, one of their ends is slightly arched to allow acute angles. The use of 3D printing technology facilitates this unique design. The bi-dimensional beam is hung upside down against a grid paper and guyed by a nylon cable, as shown in Fig. 3. The prototype is bi-dimensional and offers more stability when hung upside down, which reduces out-of-plane motion. Although most applications suggest a stand-up position, it is important to validate the numerical model under reduced error conditions. Deformed configurations are photographed, and image pixel positions are calibrated to yield metric deformation measurements. The camera is placed as far as possible from the prototype, and the images are zoomed in to minimize perspective errors. Tolerance for these uncertainties is indicated in the results section.

Four deformed configurations and the natural layout under self-weight are studied, and the final length of the pulling cable is replicated in the numerical model for all configurations. Vibration analyses are performed in all positions. An accelerometer is attached to the last bar (highlighted in Fig. 3) to extract the natural frequencies. The accelerometer is used to generate a frequency response function using the impact hammer test. Additionally, the experiment is

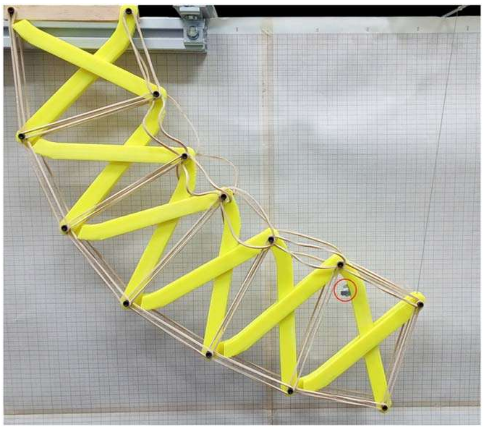

Fig. 3 Example of a deformed configuration

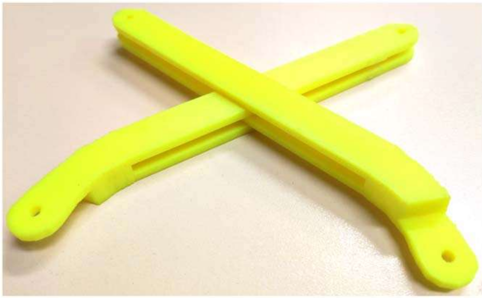

Fig. 4 Struts design in detail

recorded by a 30 frames per second (fps) camera, and image processing software is used to track the node positions over time. Finally, a fast Fourier transform algorithm is applied to convert those position-time data sets into frequency responses, providing more experimental data to validate the method. Utilizing image processing to the vibration study is convenient in this experiment because this structure exhibits low natural frequencies, staying within the camera's fps limits. Furthermore, the mass of the accelerometer may interfere with the results. However, the image processing approach is impracticable for higher frequencies, leaving a range of interest to rely on the accelerometer data.

3.3 Properties of the Cables. Rubber bands are employed as cables due to their low Young's modulus and extensive elastic range, enabling small input loads to induce large displacements without plastic deformation. Furthermore, as the relaxed length of the bands is shorter than the distance between nodes, they are initially pre-stressed, reducing the occurrence of slack cables in the analysis. An experiment is conducted to find the Young's modulus of the rubber. A hook scale pulls a 0.083 m long band, and the normal force is acquired for every 0.01 m or 0.005 m displacement, yielding the results shown in Table 1.

Since the rubber material exhibits a nonlinear stress–strain behavior, we use the Young's modulus from the stress–strain relation observed on the prototype, which never exceeds 30%. Therefore, the best-fitting Young's modulus for the prototype of 3.00 MPa is obtained using the first six experimental stress–strain test data points, as shown in Fig. 5.

3.4 Relevance of the Force Density Term. It is reasonable to question the importance of the force density s_k compared to the classical bar stiffness EA/l. Since its contribution to the global stiffness might not be significant [58], this term could be removed to simplify the methodology. This subsection focuses on showing the relevance of such term and why it should not be removed in this study. For a horizontal element of length l, cross-sectional area A, and Young's modulus E under the action of a regular force f, the members' matrix is defined by Eq. (21).

Table 1 Rubber band strain results

l (m)	f (N)	ϵ	σ (Pa)
0.083	0.000	0	0
0.090	0.883	0.08	3.92×10^5
0.095	1.275	0.14	5.67×10^5
0.100	1.668	0.20	7.41×10^5
0.105	1.962	0.27	8.72×10^5
0.110	2.256	0.33	1.00×10^6
0.120	2.747	0.45	1.22×10^6
0.130	2.943	0.57	1.31×10^6
0.140	3.335	0.69	1.48×10^6
0.150	3.630	0.81	1.61×10^6

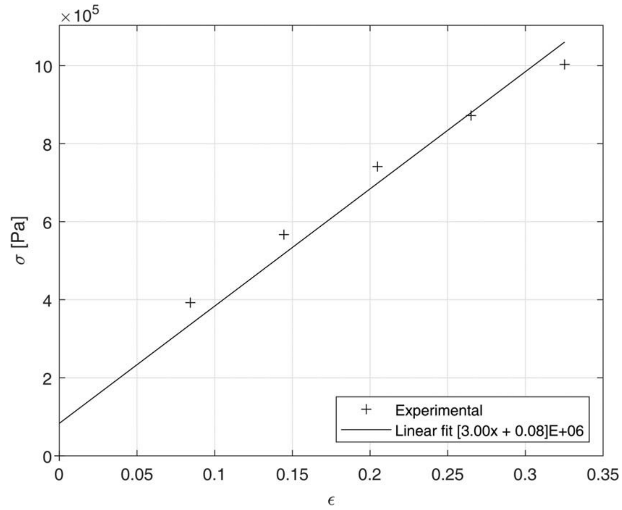

Fig. 5 Stress strain diagram of the rubber material

$$\mathbf{M} = \mathbf{N}\mathbf{C}^T = \begin{bmatrix} 0 & l \\ 0 & 0 \end{bmatrix}\begin{bmatrix} -1 \\ 1 \end{bmatrix} = \begin{bmatrix} l \\ 0 \end{bmatrix} \tag{21}$$

$\mathbf{L_1}$ and $\mathbf{K_G}$ matrices are built (Eqs. (22) and (23)) following the methodology described in Section 2.1.

$$\mathbf{L_1} = s_k\left(I - \frac{\begin{bmatrix} l \\ 0 \end{bmatrix}\begin{bmatrix} l & 0 \end{bmatrix}}{l^2}\right) + K_B\frac{\begin{bmatrix} l \\ 0 \end{bmatrix}\begin{bmatrix} l & 0 \end{bmatrix}}{l^2} = \begin{bmatrix} K_B & 0 \\ 0 & s_k \end{bmatrix} = \begin{bmatrix} \frac{EA}{l} & 0 \\ 0 & \frac{f}{l} \end{bmatrix} \tag{22}$$

$$\mathbf{K_G} = \begin{bmatrix} 1 & -1 \\ -1 & 1 \end{bmatrix} \otimes \mathbf{L_1} = \begin{bmatrix} \mathbf{L_1} & -\mathbf{L_1} \\ -\mathbf{L_1} & \mathbf{L_1} \end{bmatrix} = \begin{bmatrix} \frac{EA}{l} & 0 & \frac{-EA}{l} & 0 \\ 0 & \frac{f}{l} & 0 & \frac{-f}{l} \\ \frac{-EA}{l} & 0 & \frac{EA}{l} & 0 \\ 0 & \frac{-f}{l} & 0 & \frac{f}{l} \end{bmatrix} \tag{23}$$

The stiffness K_B and force density s_k contribute directly to the stiffness matrix. The first one is assumed to be constant, but the second one is not, as the normal force f changes depending on the loads. The tension σ does not exceed 3MPa in this study, therefore we may plot the comparison between s_k and K_B versus tension σ

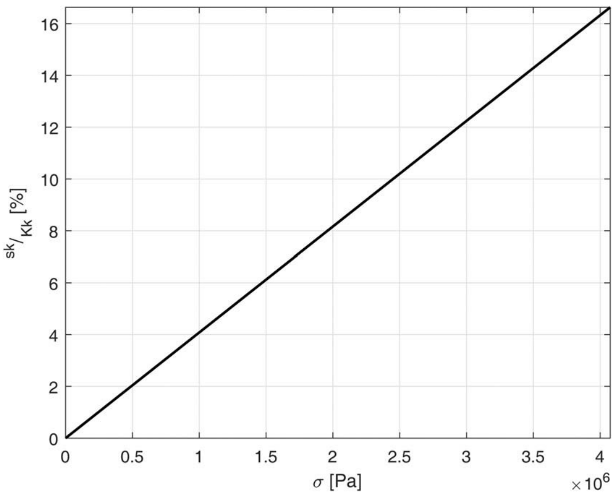

Fig. 6 Relevance of s_k

(Fig. 6). Since s_k reaches up to 12% of stiffness K_B, the contribution of the force density must be considered in the stiffness matrix of the present prototype.

4 Results and Discussion

4.1 Nonlinear Static Analysis. The prototype's response and the simulation results are represented by dashed and solid lines, respectively (Figs. 7(*a*)–7(*e*)). Thick lines represent the struts, and thin lines stand for the cables. The circles show the 10 mm radius tolerance of the experiment regarding node positions. The total weight of the structure (290 g) is equally distributed among the 12 bars, and the cables are considered massless. The Young's modulus of the bars is considered to be 2 GPa, and they are assumed to have a Hookean behavior. The final lengths of the pulling cable are 0.61 m, 0.49 m, 0.40 m, 0.28 m, and 0.16 m for configurations 0, 1, 2, 3, and 4, respectively.

Because the structure is hung upside down, gravity points upwards in the graphs as shown in Figs. 7(*a*)–7(*e*). The first graph contains data from the experiment and simulation without any loads in the pulling cable (under self-weight only). Therefore, the tip of the beam holds its own weight, and the base supports the weight of the whole structure, causing more significant deformation of the sections close to the support. All the other four graphs contain the guying cable, each with a different final length.

Despite showing a slightly nonlinear behavior (Fig. 5), which brings errors to the graphs in Figs. 7(*a*)–7(*e*), the rubber bands are helpful in reducing the number of discontinuities (transitions between slack to tensioned states) in the analysis. Additionally, despite the geometric constraints of the bars that force the experiment to remain two-dimensional, they exhibit slight bending, allowing for a small displacement in depth. Using the tip position as a reference, the modeling error relative to the beam length is calculated (Table 2). Most of the experimental data points align with the simulations, and the maximum error in the tip position is 3.51% in configuration 1, indicating the robustness of the model.

4.2 Polynomial Interpolation of Nodal Positions. The trajectory of each node is mapped (Fig. 8) for 150 load increments from configuration 1 to configuration 4.

To simplify access to these results and approximate any intermediate configuration, the polynomials are expressed in matrix form (Eq. (10)). The coefficient matrices **X** and **Y** are defined in

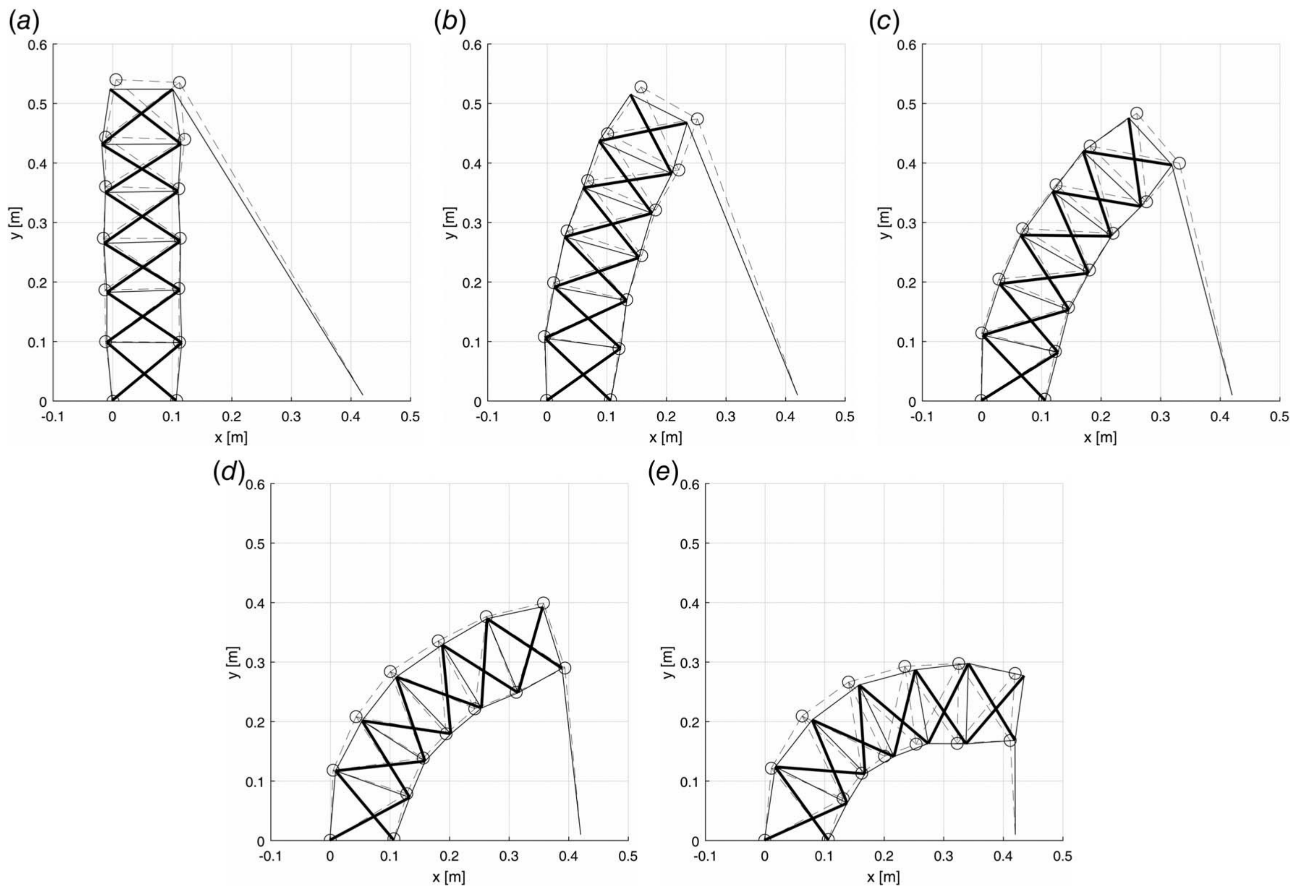

Fig. 7 Static analysis: (*a*) configuration 0, (*b*) configuration 1, (*c*) configuration 2, (*d*) configuration 3, and (*e*) configuration 4

Table 2 Tip positions of configurations 0–4 obtained from experimental and numerical approaches

	Experimental		Numerical		
Config.	x (m)	y (m)	x (m)	y (m)	Error (%)
0	0.112	0.535	0.101	0.524	2.97
1	0.252	0.474	0.235	0.468	3.51
2	0.332	0.400	0.319	0.400	2.49
3	0.394	0.290	0.389	0.290	1.02
4	0.411	0.168	0.420	0.169	1.64

Eqs. (24) and (25) for generating x (**i**) and y (**j**) coordinates in millimeters.

$$\mathbf{X} = \begin{bmatrix} 0 & 0 & 0 & 0 & -1.10 \\ 11.0 & -32.4 & 43.6 & -63.2 & 31.1 \\ 17.7 & -53.9 & 70.8 & -162 & 117 \\ 13.7 & -29.4 & 22.8 & -242 & 220 \\ -0.07 & 47.9 & -157 & -227 & 321 \\ -2.06 & 122 & -394 & -154 & 406 \\ 25.5 & 91.5 & -603 & 1.99 & 473 \\ 0 & 0 & 0 & 0 & 106 \\ -3.70 & -0.08 & -3.78 & -19.8 & 143 \\ -11.3 & 8.46 & -46.5 & -12.2 & 174 \\ -14.7 & 7.26 & -110 & 8.01 & 222 \\ -7.87 & -15.5 & -185 & 40.1 & 276 \\ 1.86 & -52.0 & -278 & 111 & 328 \\ 22.3 & -71.5 & -454 & 198 & 400 \end{bmatrix} \tag{24}$$

$$\mathbf{Y} = \begin{bmatrix} 0 & 0 & 0 & 0 & 0 \\ 4.09 & -13.2 & 12.4 & -37.6 & 133 \\ -10.0 & 27.1 & -63.7 & 30.2 & 199 \\ -30.6 & 81.8 & -194 & 180 & 227 \\ -40.0 & 81.4 & -285 & 390 & 204 \\ -32.5 & 5.21 & -301 & 596 & 163 \\ -38.7 & -114 & -174 & 756 & 94.4 \\ 0 & 0 & 0 & 0 & 0 \\ -4.36 & 20.2 & -25.5 & 58.7 & 49.2 \\ -9.12 & 23.2 & -27.9 & 118 & 83.2 \\ -19.9 & 20.89 & -24.8 & 204 & 89.6 \\ -37.4 & 8.50 & -6.37 & 305 & 84.2 \\ -64.5 & -5.86 & 36.2 & 416 & 52.4 \\ -84.2 & -69.0 & 80.0 & 588 & 11.8 \end{bmatrix} \tag{25}$$

The computational cost of a polynomial evaluation for each node is about 3×10^5 less than running a nonlinear static analysis of this model. This fast transformation allows this technique to be implemented in real-time vibration control strategies.

4.3 Modal Analysis. The first set of graphs (Figs. 15, 16, 17, 18, and 19) contains the numerical results displaying the two first vibration modes and their natural frequencies. The experimental results acquired through image processing and the accelerometer (impact hammer test) are presented in Figs. 20–25 and Figs. 26–30, respectively (these figures are available in the Appendix). In Figs. 20–25, the thin lines represent the frequency spectrum of different points in the same capture or different captures, while the thick line in each graph represents the mean spectral value. Some of the frequency responses show the first two natural frequencies in the same spectrum (positions 0 and 2), but two analyses are required to extract each frequency in position 1. In Figs. 26–30, each thin line represents the spectrum of a different external input, and the thick line in each graph is the mean spectral value. Finally, the results for natural frequencies are compiled and compared in Table 3.

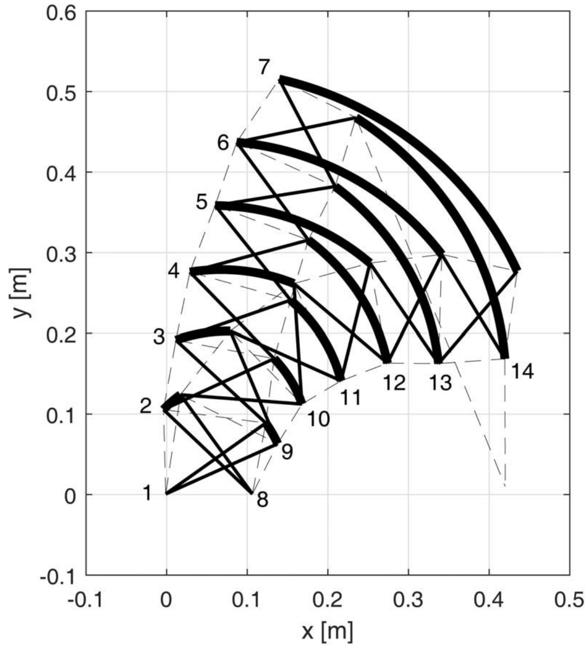

Fig. 8 Polynomial approximation of the static results

The *Error* column compares the experimental and numerical results and shows the lowest experimental error. Configurations 0, 1, 3, and 4 report a good agreement between numerical and experimental results, but there is a considerable error in the first mode of configuration 2. The resolutions of the spectrum obtained through image processing are approximately 0.4 Hz, which fit in the 7% error that has garnered attention. These discrepancies primarily stem from the experimental data capturing damped frequencies and the uncertainties associated with material properties and geometry. Furthermore, the peaks shown in the spectra are considerably wide, encompassing the natural frequencies obtained through simulations within their width. The second frequency of configuration 4 could not be extracted through image processing, but was acquired by the accelerometer and concurred with the numerically predicted result. Due to the hardware limitations of the uniaxial accelerometer, some vibration modes where the displacement is mostly orthogonal to the sensor could not be extracted. This limitation is noticeable in the second vibration mode of configurations 0, 1, 2, and 3 and the first mode of configuration 2. Moreover, a high damping ratio may affect the accurate extraction of higher mode natural frequencies through experimental methods. In this study, this issue is present in the second mode of configuration 3, where the damping factor is more significant (Table 4).

The increase in stiffness in a more tensioned structure is gradual because some cables of the tensegrity become slack under larger deformations, reducing the growth rate of the global stiffness. Contrarily, as the geometry of the tensegrity changes, its effective length decreases, leading to higher natural frequencies in these deformed configurations. In other words, shortening the guying cable causes a few tendons to become slack, but it also places more stress on the taut tendons and shortens the beam, causing an overall increase in the global stiffness. This pattern is more evident in the numerical results for all intermediate configurations (Fig. 9), where higher loads lead to higher natural frequencies.

The vertical axis compares the final length l_f of the pulling cable in each configuration to the starting length l_0 (configuration 0), therefore keeping the ratio between 0 (maximum load) and 1 (no load). The axis orientation is reversed to follow the pattern used in the work presented in Ref. [45]. Also, the best-fitting

Table 3 Natural frequencies extracted from experiments (image processing and accelerometer data) and numerical analyses

Configuration	Mode	Numerical (Hz)	Image processing (Hz)	Accelerometer (Hz)	Error (%)
0	1st	2.80	2.36	2.87	2.5
	2nd	4.45	4.38	–	1.6
1	1st	2.89	2.93	–	1.4
	2nd	4.41	4.40	–	0.2
2	1st	2.99	3.20	3.50	7.0
	2nd	4.56	4.37	–	4.2
3	1st	3.19	3.67	3.25	1.9
	2nd	4.96	–	–	–
4	1st	3.40	3.44	3.38	0.6
	2nd	5.82	–	6.12	5.2

Table 4 Damping ratio and natural frequency obtained using Prony's method

	Modal parameters	
Configuration	Natural frequency (Hz)	Damping ratio (%)
0	2.72	32.5
1	2.95	32.3
2	3.09	17.4
3	3.33	49.4
4	3.76	18.8

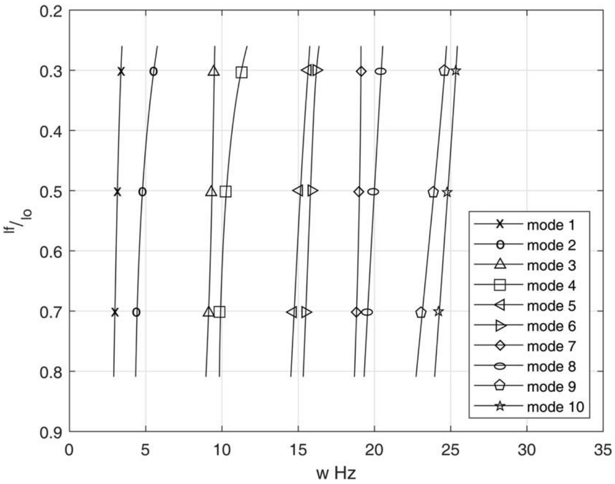

Fig. 9 Ten first natural frequencies obtained numerically for all static positions between configurations 1 and 4

experimental results for the first two modes are compared to numerical outputs (lines) in Fig. 10.

4.4 Damping. Free damped responses for configurations 0–4 (Fig. 11) are obtained from the video recordings used in Sec. 4.3 to determine the natural frequencies of the tensegrity.

Prony's method is applied for all five configurations. The first mode natural frequencies and damping ratios of each configuration are presented in Table 4. Based on previous studies [45], the damping ratio in intermediate configurations can be reliably estimated from five states using a low-order polynomial interpolation. The steepest descent algorithm is applied to solve the optimization problem, and the proportional damping parameters are listed in Table 5.

The numerical results for natural frequencies presented in Table 5 exhibit good agreement with the experimental results shown in

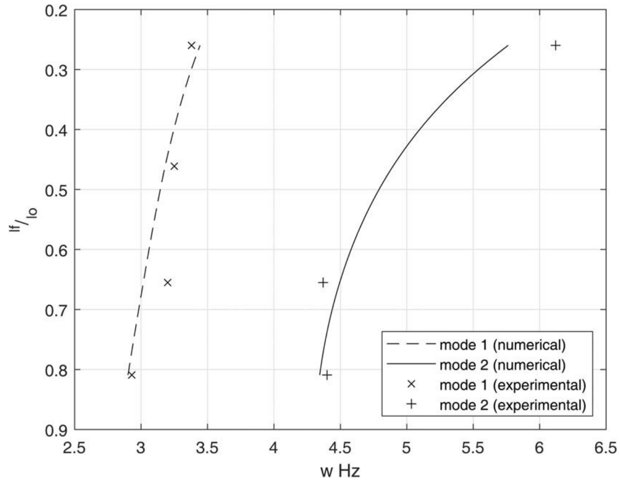

Fig. 10 Experimental and numerical solutions of the two first natural frequencies

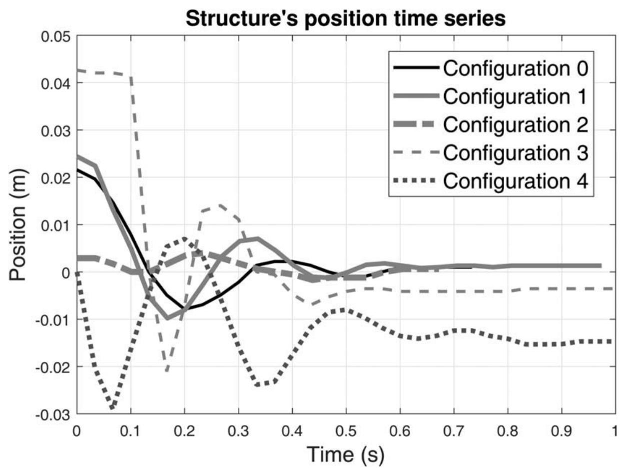

Fig. 11 Free damped response obtained through image processing. Results presented for five configurations.

Table 4 under a maximum relative difference of 7.45%. Therefore, the proportional damping assumption is considered satisfactory in this scenario.

4.5 Control. To evaluate the proposed procedures, the dynamical characteristics of configuration 2 are used as inputs for the

Table 5 Natural frequencies and damping ratio of the first mode's system with estimated proportional damping

Config.	$\alpha \cdot 10^3$ (1/s)	$\beta \cdot 10^3$ (s)	Natural frequency (Hz)	Damping ratio (%)
	Parameters			
0	4.0	36.7	2.83	32.5
1	1.5	35.1	2.95	32.3
2	7.3	18.6	3.05	17.4
3	10.8	51.8	3.29	49.4
4	6.39	37.8	3.48	18.8

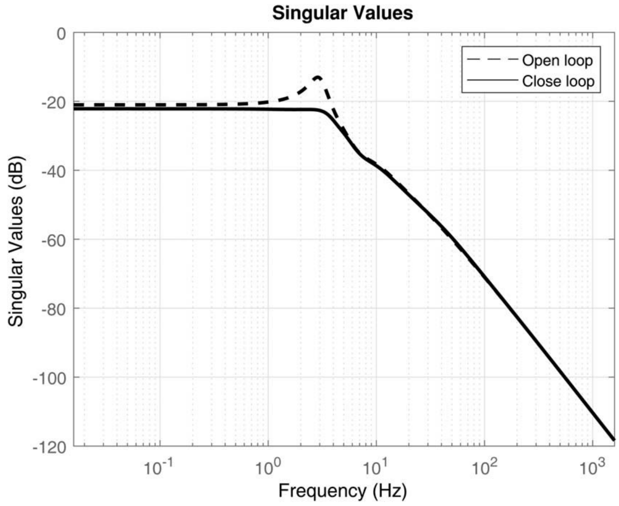

Fig. 12 Frequency response for controlled and uncontrolled vibration on configuration 2

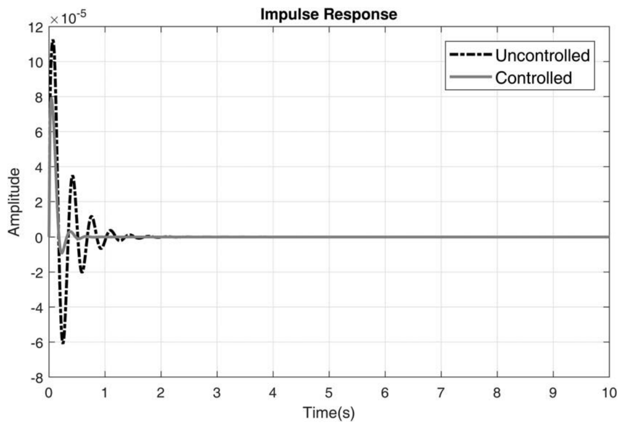

Fig. 13 Controlled and uncontrolled responses under an impulse load on the tensegrity beam tip on configuration 2

H_∞ control strategy. This configuration is selected because it presents the lowest damping factor and the structure is in an intermediate shape between configurations 0 and 4. The filters replicate those used in Ref. [45] but with adjusted gains to satisfy the different structural dynamics. The open- and closed-loop systems are compared in Fig. 12 in terms of singular values. The frequency peak at 2.88 Hz is significantly reduced by the controller. Additionally, an impulse force (Fig. 13) and a 2 N root-mean-square (RMS) random vibration (Fig. 14) are loaded on the tensegrity beam tip node in both directions. The infinite norm is 0.224 and 0.078 for the system without and with control, respectively. The controlled response to an impulse input shows a higher vibration suppression

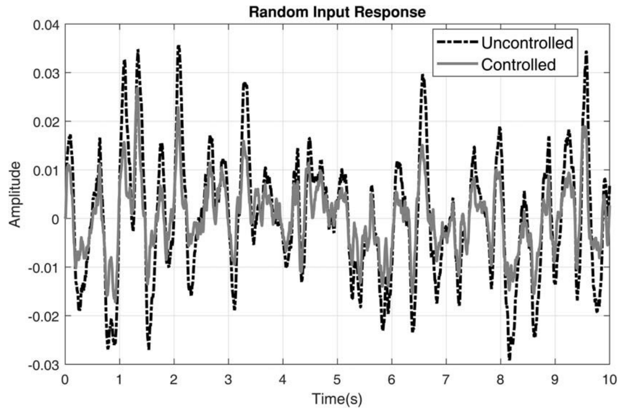

Fig. 14 Controlled and uncontrolled responses under a random load on the tensegrity beam tip on configuration 2

compared to the random input response. This suggests that this control technique is less efficient under random inputs for this model. Still, the vibration levels of the controlled response to random inputs are approximately 36% lower than the uncontrolled response. The control results regarding configurations 0, 1, 3, and 4 are equivalent in behavior to configuration 2.

5 Conclusions

A lightweight, long, and flexible 2D tensegrity cable guyed beam was both modeled and built. The model accounted for self-weight and was verified in static experiments with five different loads. The proposed methodology offers reliable results through a more straightforward process compared to current techniques. It involves combining Euler's incremental loads method for solving nonlinear problems in finite element analysis with a procedure designed to calculate linear statics of pre-stressed tensegrity structures. The incremental loads procedure is convenient to implement, but also less efficient than other methodologies. However, the structure under study requires modeling very few elements, which keeps the computational cost of the simulation low and highlights the advantages of simpler implementation. Most of the experimental data aligned with the simulation outputs, indicating the accuracy of the proposed methodology. The image processing technique provides closer results to the numerical outcomes than the accelerometer data for low frequencies, which are not far from the minimum range of the instrument (1 Hz). However, image processing is limited by the camera's fps, narrowing the acquisition range. Advantages such as high accuracy, ease of use, low cost, quick data acquisition, and absence of instrumentation attached to the structure justify its use in low-frequency experiments. Damping ratios were estimated through an optimization technique comparing image processing and numerical data using Prony's method. This study estimates the damping ratio for five configurations of the structure, with intermediate points reliably predicted by a low-order polynomial interpolation. The numerical natural frequencies obtained through Prony's method showed good agreement with experimental results, with a maximum difference of 7.45%. Finally, a numerical H_∞ control strategy is applied to suppress vibrations in the tensegrity beam using the presented dynamical model. Future research steps involve assessing the influence of environmental factors on the behavior of the structure, such as wind and temperature loads, and performing experiments to verify the numerical control results and optimize the controller.

Acknowledgment

The authors thank Conselho Nacional de Desenvolvimento Científico e Tecnológico (CNPq), Brazil's research support foundation, for sponsoring this work.

Conflict of Interest

There are no conflicts of interest.

Data Availability Statement

The authors attest that all data for this study are included in the paper.

Nomenclature

b = number of nodes
c = final to initial length ratio
f = normal force (N)
l = member length (m)
q = structure's mass (kg)
s = force density (N/m)
t = time (s)
u = actuator force (N)
w = number of struts
x = position in x direction (m)
y = position in y direction (m)
$\mathbf{b}$ = force input vector
$\mathbf{c}$ = connectivity vector
$\mathbf{e}$ = auxiliary connectivity vector
$\mathbf{f}$ = external loads vector (N)
$\mathbf{m}$ = member vector (m)
$\mathbf{n}$ = position vector (m)
$\mathbf{r}$ = position vector in the static analysis (m)
$\mathbf{u}$ = displacements vector (m)
$\mathbf{w}$ = disturbance forces (N)
$\mathbf{x}$ = position vector in the dynamical analysis (m)
$\mathbf{z}$ = order reduction auxiliary vector
A = cross-sectional area (m^2)
D = number of vibration modes
E = Young's modulus (Pa)
J = cost function
P = amplitude
$\mathbf{B}$ = disturbance input vector
$\mathbf{C}$ = connectivity matrix
$\mathbf{D}$ = damping matrix (N s/m)
$\mathbf{G}$ = order reduction auxiliary matrix
$\mathbf{H}$ = mass matrix (kg)
$\mathbf{K}$ = stiffness matrix (Pa)
$\mathbf{L}$ = stiffness matrix auxiliary component (Pa)
$\mathbf{M}$ = members matrix (m)
$\mathbf{N}$ = node matrix (m)
$\mathbf{Q}$ = order reduction auxiliary matrix
$\mathbf{X}$ = x coefficients matrix (m)
$\mathbf{Y}$ = y coefficients matrix (m)
ft = fitting function

Greek Symbols

α = mass associated damping parameter
β = stiffness associated damping parameter
λ = pole
ξ = damping ratio
σ = internal normal stress (Pa)
ω = natural frequency (rad/s)
Ω = damped frequency (rad/s)

Superscripts and Subscripts

d = vibration mode
exp = experimental
f = final
G = global
i = node index
j = node index
k = element index
num = numerical
o = initial
Σ = pre-stress component
Φ = material component

Appendix A: Numerical Modal Analyses on Configurations 0–4

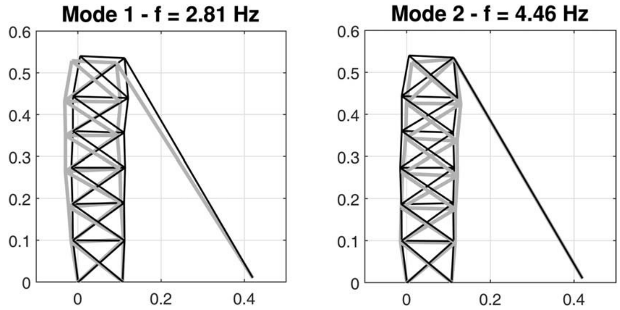

Fig. 15 Configuration 0

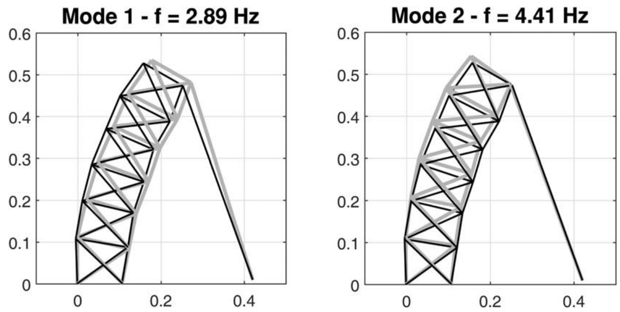

Fig. 16 Configuration 1

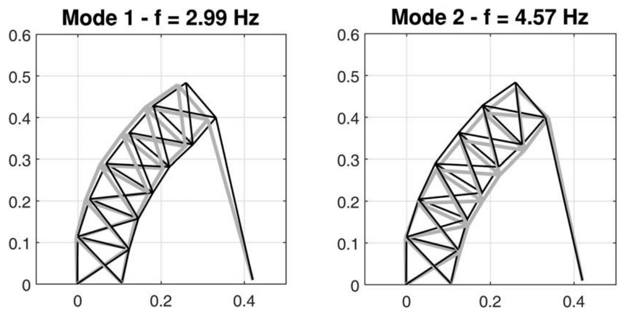

Fig. 17 Configuration 2

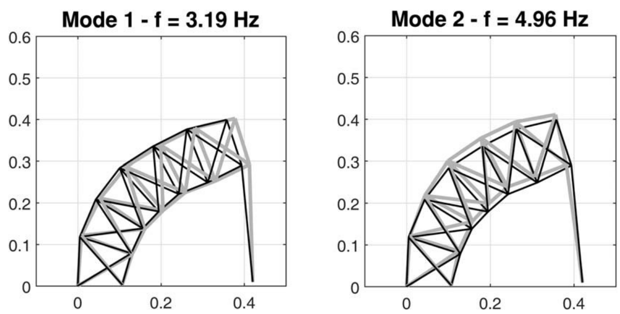

Fig. 18 Configuration 3

Appendix B: Frequency Responses Obtained Through Image Processing

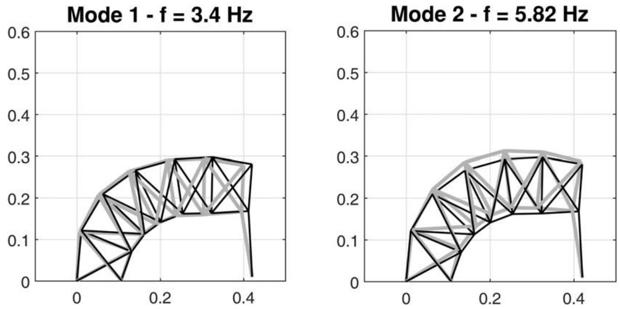

Fig. 19 Configuration 4

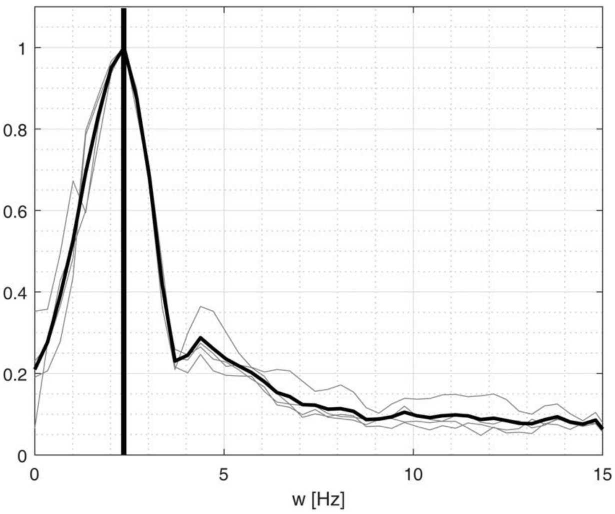

Fig. 20 Configuration 0

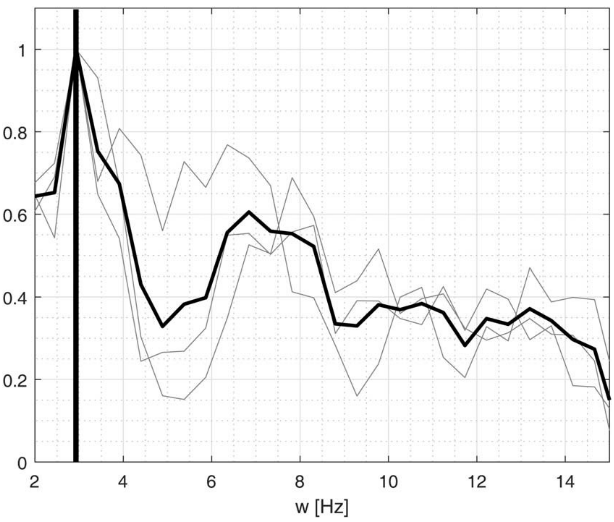

Fig. 21 Configuration 1

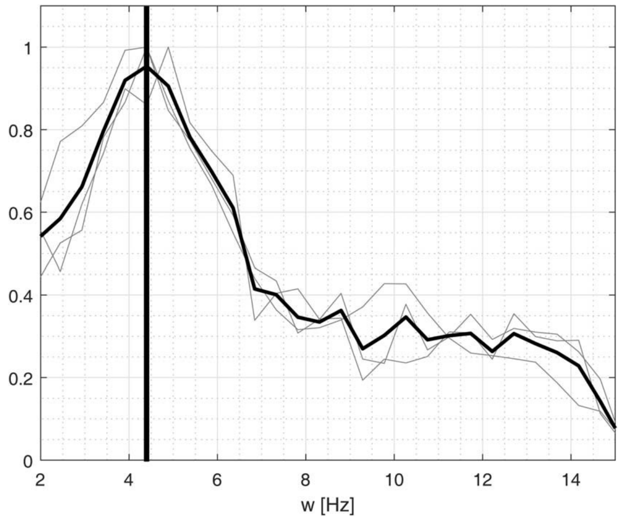

Fig. 22 Configuration 1—second mode

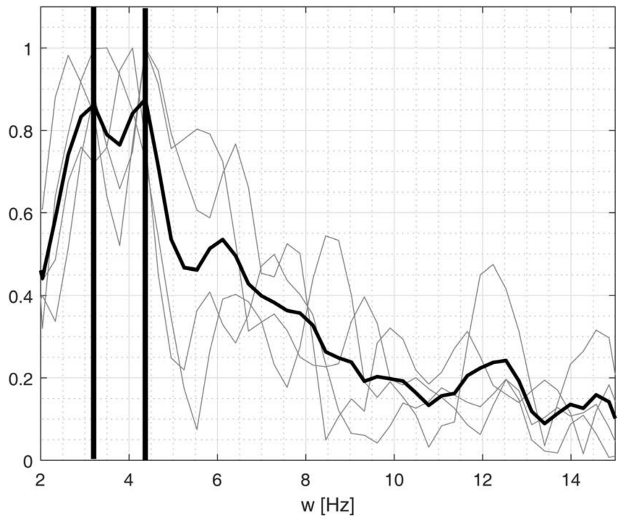

Fig. 23 Configuration 2

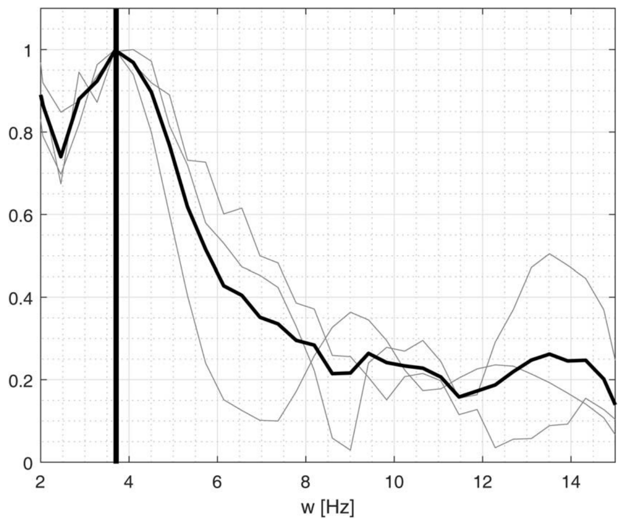

Fig. 24 Configuration 3

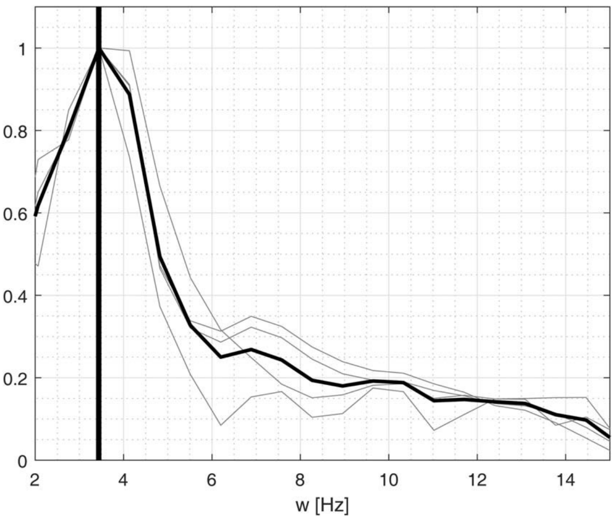

Fig. 25 Configuration 4

Appendix C: Frequency Responses Obtained Through Accelerometer Data

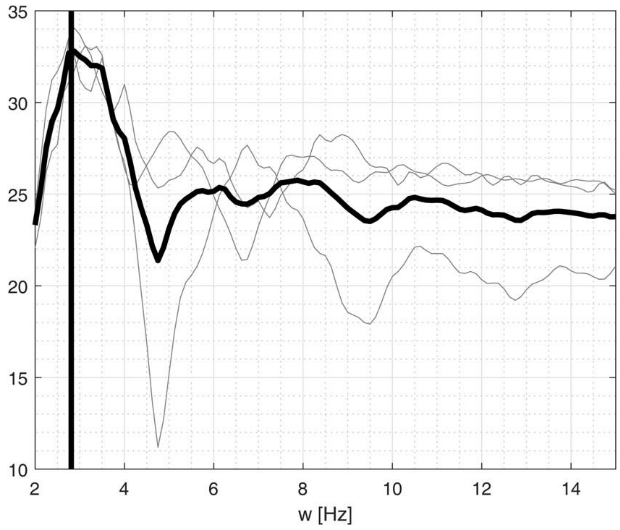

Fig. 26 Configuration 0

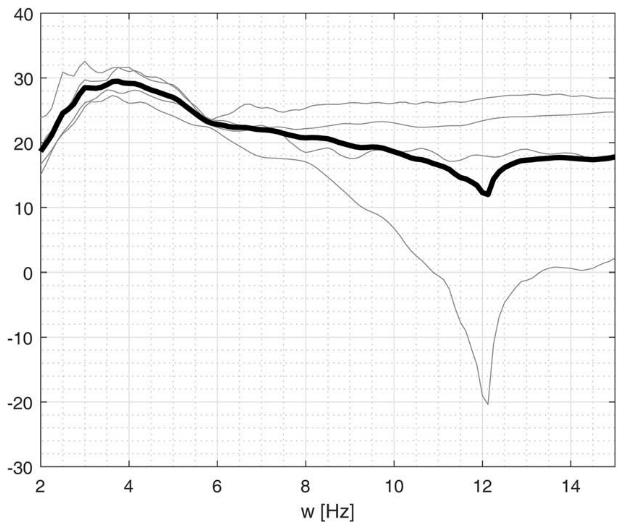

Fig. 27 Configuration 1

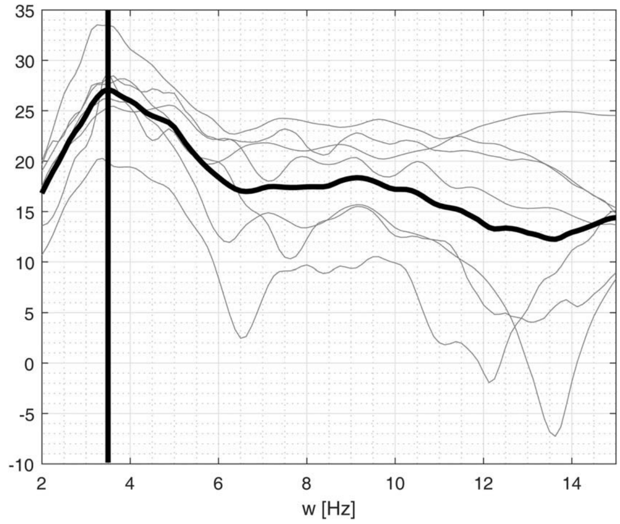

Fig. 28 Configuration 2

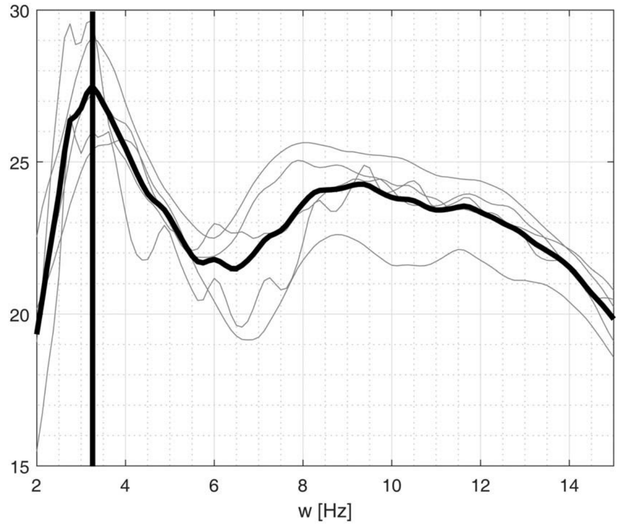

Fig. 29 Configuration 3

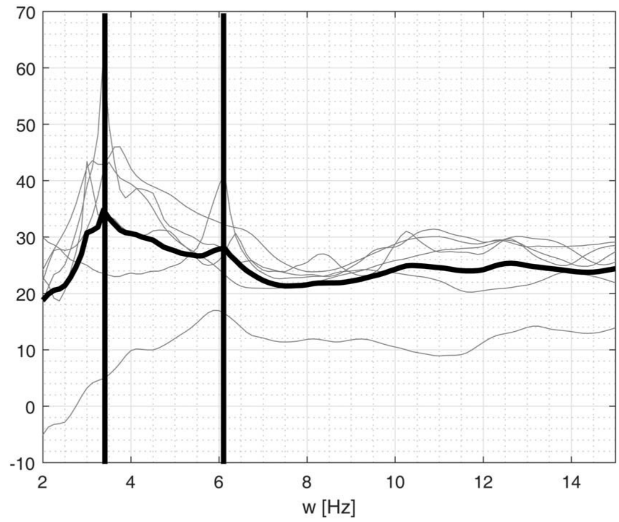

Fig. 30 Configuration 4

References

[1] Fuller, R. B., and Applewhite, E. J., 1975, *Synergetics: Explorations in the Geometry of Thinking*, Macmillan, Sebastopol, CA.

[2] Zhang, J. Y., and Ohsaki, M., 2015, *Tensegrity Structures—Form, Stability and Symmetry*, Springer, New York.

[3] Motro, R., 1992, "Tensegrity Systems: The State of the Art," Int. J. Space Struct., **7**(2), pp. 75–83.

[4] Estrada, G. G., Bungartz, H. -J., and Mohrdieck, C., 2006, "Numerical Form-Finding of Tensegrity Structures," Int. J. Solids Struct., **43**(22), pp. 6855–6868.

[5] Kan, Z., Peng, H., Chen, B., Xie, X., and Sun, L., 2019, "Investigation of Strut Collision in Tensegrity Statics and Dynamics," Int. J. Solids Struct., **167**, pp. 202–219.

[6] Kan, Z., Song, N., Peng, H., Chen, B., and Song, X., 2021, "A Comprehensive Framework for Multibody System Analysis With Clustered Cables: Examples of Tensegrity Structures," Int. J. Solids Struct., **210**, pp. 289–309.

[7] Ashwear, N., and Eriksson, A., 2014, "Natural Frequencies Describe the Pre-stress in Tensegrity Structures," Comput. Struct., **136**, pp. 162–171.

[8] Zhang, J., and Ohsaki, M., 2006, "Adaptive Force Density Method for Form-Finding Problem of Tensegrity Structures," Int. J. Solids Struct., **43**(18), pp. 5658–5673.

[9] Paul, C., Valero-Cuevas, F. J., and Lipson, H., 2006, "Design and Control of Tensegrity Robots for Locomotion," IEEE Trans. Rob., **22**(5), pp. 944–957.

[10] Goyal, R., Skelton, R. E., and Peraza Hernandez, E. A., 2020, "Efficient Design of Lightweight Reinforced Tensegrities Under Local and Global Failure Constraints," ASME J. Appl. Mech., **87**(11), p. 111005.

[11] Ali, N. B. H., and Smith, I., 2010, "Dynamic Behavior and Vibration Control of a Tensegrity Structure," Int. J. Solids Struct., **47**(9), pp. 1285–1296.

[12] Yang, S., and Sultan, C., 2019, "Deployment of Foldable Tensegrity-Membrane Systems Via Transition Between Tensegrity Configurations and Tensegrity-Membrane Configurations," Int. J. Solids Struct., **160**, pp. 103–119.

[13] Zhu, D., and Deng, H., 2020, "Deployment of Tensegrities Subjected to Load-Carrying Stiffness Constraints," Int. J. Solids Struct., **206**, pp. 224–235.

[14] Tibert, A. G., and Pellegrino, S., 2003, "Deployable Tensegrity Masts," 44th AIAA/ASME/ASCE/AHS/ASC Structures, Structural Dynamics, and Materials Conference, Norfolk, VA, Apr. 7–10, p. 1978.

[15] Sultan, C., and Skelton, R., 2003, "Deployment of Tensegrity Structures," Int. J. Solids Struct., **40**(18), pp. 4637–4657.

[16] Feng, X., Miah, M. S., and Ou, Y., 2018, "Dynamic Behavior and Vibration Mitigation of a Spatial Tensegrity Beam," Eng. Struct., **171**, pp. 1007–1016.

[17] Schorr, P., Chavez, J., Zentner, L., and Böhm, V., 2021, "Reconfiguration of Planar Quadrilateral Linkages Utilizing the Tensegrity Principle," Mech. Mach. Theory, **156**, p. 104172.

[18] Begey, J., Vedrines, M., Andreff, N., and Renaud, P., 2020, "Selection of Actuation Mode for Tensegrity Mechanisms: The Case Study of the Actuated Snelson Cross," Mech. Mach. Theory, **152**, p. 103881.

[19] Muralidharan, V., and Wenger, P., 2021, "Optimal Design and Comparative Study of Two Antagonistically Actuated Tensegrity Joints," Mech. Mach. Theory, **159**, p. 104249.

[20] Chen, L.-H., Kim, K., Tang, E., Li, K., House, R., Zhu, E. L., Fountain, K., Agogino, A. M., Agogino, A., and Sunspiral, V., 2017, "Soft Spherical Tensegrity Robot Design Using Rod-Centered Actuation and Control," ASME J. Mech. Rob., **9**(2), p. 025001.

[21] Fazli, N., and Abedian, A., 2011, "Design of Tensegrity Structures for Supporting Deployable Mesh Antennas," Sci. Iranica, **18**(5), pp. 1078–1087.

[22] Scoccia, C., Carbonari, L., Palmieri, G., Callegari, M., Rossi, M., Munafó, P., Marchione, F., and Chiappini, G., 2022, "Design of a Tensegrity Servo-actuated Structure for Civil Applications," ASME J. Mech. Des., **144**(4), p. 043302.

[23] Bansod, Y. D., Matsumoto, T., Nagayama, K., and Bursa, J., 2018, "A Finite Element Bendo-tensegrity Model of Eukaryotic Cell," ASME J. Biomech. Eng., **140**(10), p. 101001.

[24] Raafat, M., and Baz, A., 2022, "Damping and Bandgap Characteristics of a Viscoelastic Tensegrity Damper," ASME J. Vib. Acoust., **144**(1), p. 011001.

[25] Pham, N. K., and Peraza Hernandez, E. A., 2021, "Modeling and Design Exploration of a Tensegrity-Based Twisting Wing," ASME J. Mech. Rob., **13**(3), p. 031019.

[26] Vasquez, R. E., Crane III, C. D., and Correa, J. C., 2014, "Analysis of a Planar Tensegrity Mechanism for Ocean Wave Energy Harvesting," ASME J. Mech. Rob., **6**(3), p. 031015.

[27] Dong, W., Stafford, P. J., and Ruiz-Teran, A. M., 2019, "Inverse Form-Finding for Tensegrity Structures," Comput. Struct., **215**, pp. 27–42.

[28] Yuan, S., and Yang, B., 2019, "The Fixed Nodal Position Method for Form Finding of High-Precision Lightweight Truss Structures," Int. J. Solids Struct., **161**, pp. 82–95.

[29] Koohestani, K., 2020, "Innovative Numerical Form-Finding of Tensegrity Structures," Int. J. Solids Struct., **206**, pp. 304–313.

[30] Wang, Y., and Senatore, G., 2020, "Extended Integrated Force Method for the Analysis of Prestress-Stable Statically and Kinematically Indeterminate Structures," Int. J. Solids Struct., **202**, pp. 798–815.

[31] Wang, Y., Xu, X., and Luo, Y., 2020, "Topology Design of General Tensegrity With Rigid Bodies," Int. J. Solids Struct., **202**, pp. 278–298.

[32] Su, Y., Zhang, J., Ohsaki, M., and Wu, Y., 2020, "Topology Optimization and Shape Design Method for Large-Span Tensegrity Structures With Reciprocal Struts," Int. J. Solids Struct., **206**, pp. 9–22.

[33] Wang, Y., Xu, X., and Luo, Y., 2021, "A Unifying Framework for Form-Finding and Topology-Finding of Tensegrity Structures," Comput. Struct., **247**, p. 106486.

[34] Fernández-Ruiz, M. A., Hernández-Montes, E., Carbonell-Márquez, J. F., and Gil-Martín, L. M., 2019, "Octahedron Family: The Double-Expanded Octahedron Tensegrity," Int. J. Solids Struct., **165**, pp. 1–13.

[35] Fernández-Ruiz, M. A., Hernandez-Montes, E., and Gil-Martin, L. M., 2021, "The Octahedron Family as a Source of Tensegrity Families: The X-Octahedron Family," Int. J. Solids Struct., **208–209**, pp. 1–12.

[36] Liu, S., Li, Q., Wang, P., and Guo, F., 2020, "Kinematic and Static Analysis of a Novel Tensegrity Robot," Mech. Mach. Theory, **149**, p. 103788.

[37] Zhu, D., Deng, H., and Wu, X., 2020, "Selecting Active Members to Drive the Mechanism Displacement of Tensegrities," Int. J. Solids Struct., **191–192**, pp. 278–292.

[38] Kebiche, K., Kazi-Aoual, M., and Motro, R., 1999, "Geometrical Non-linear Analysis of Tensegrity Systems," Eng. Struct., **21**(9), pp. 864–876.

[39] Kan, Z., Peng, H., and Chen, B., 2018, "Complementarity Framework for Nonlinear Analysis of Tensegrity Structures With Slack Cables," AIAA J., **56**(12), pp. 5013–5027.

[40] Shi, C., Guo, H., Cheng, Y., Liu, R., and Deng, Z., 2020, "Design and Multi-objective Comprehensive Optimization of Cable-Strut Tensioned Antenna Mechanism," Acta Astronaut., **1**(178), pp. 406–422.

[41] Tran, H. C., and Lee, J., 2011, "Geometric and Material Nonlinear Analysis of Tensegrity Structures," Acta Mech. Sin., **27**(6), pp. 938–949.

[42] Zhang, L.-Y., Li, Y., Cao, Y.-P., Feng, X.-Q., and Gao, H., 2013, "A Numerical Method for Simulating Nonlinear Mechanical Responses of Tensegrity Structures Under Large Deformations," J. Appl. Mech., **80**(6), p. 061018.

[43] Furet, M., and Wenger, P., 2019, "Kinetostatic Analysis and Actuation Strategy of a Planar Tensegrity 2-X Manipulator," J. Mech. Rob., **11**(6), p. 060904.

[44] Kurka, P., Izuka, J., Gonzalez, P., Burdick, J., and Elfes, A., 2014, "Vibration of a Long, Tip Pulled Deflected Beam," AIAA J., **52**(7), pp. 1559–1563.

[45] Kurka, P., Izuka, J., Gonzalez, P., and Teixeira, L., 2016, "Large Deflections and Vibrations of a Tip Pulled Beam With Variable Transversal Section," Mech. Syst. Signal Process., **79**, pp. 271–288.

[46] Ramos, P., Izuka, J., and Kurka, P., 2016, "Experimental Robust Control of Vibration of a Long Elastic Guyed Beam Arm With Large Deformation and Variable Transversal Section," Proceedings of ISMA2016 Including USD2016, Leuven, Belgium, Sept. 19–21, pp. 155–170.

[47] Lai, G., Plummer, A., and Cleaver, D., 2020, "Distributed Actuation and Control of a Morphing Tensegrity Structure," ASME J. Dyn. Syst. Meas. Control, **142**(7), p. 071006.

[48] Skelton, R. E., and de Oliveira, M., 2009, *Tensegrity Systems*, Springer US, New York, pp. 45–72.

[49] Nelson, C. A., 2015, "A Software Tool for Analyzing Motions and Loading in Spatial Tensegrity Structures," International Design Engineering Technical Conferences and Computers and Information in Engineering Conference, Boston, MA, Aug. 2–5.

[50] Crisfield, M. A., 1991, *Non-linear Finite Element Analysis of Solids and Structures*, John Wiley & Sons, Chichester, UK.

[51] Bathe, K. J., and Cimento, A. P., 1980, "Some Practical Procedures for the Solution of Nonlinear Finite Element Equations," Comput. Methods Appl. Mech. Eng., **22**(1), pp. 59–85.

[52] Boehler, Q., Charpentier, I., Vedrines, M. S., and Renaud, P., 2015, "Definition and Computation of Tensegrity Mechanism Workspace," ASME J. Mech. Rob., **7**(4), p. 044502.

[53] Sultan, C., 2009, "Designing Structures for Dynamical Properties Via Natural Frequencies Separation: Application to Tensegrity Structures Design," Mech. Syst. Signal Process., **23**(4), pp. 1112–1122.

[54] Sultan, C., 2010, "Proportional Damping Approximation Using the Energy Gain and Simultaneous Perturbation Stochastic Approximation," Mech. Syst. Signal Process., **24**(7), pp. 2210–2224.

[55] Kurka, P. R. G., 2015, *Vibrações de sistemas dinâmicos – anâlise e síntese*, LTC, Barueri.

[56] Holland, D. B., Virgin, L. N., and Plaut, R. H., 2008, "Large Deflections and Vibration of a Tapered Cantilever Pulled at Its Tip by a Cable," J. Sound Vib., **310**(1–2), pp. 433–441.

[57] Zhao, W., Pashkevich, A., Klimchik, A., and Chablat, D., 2022, "Elastostatic Modeling of Multi-link Flexible Manipulator Based on Two-Dimensional Dual-Triangle Tensegrity Mechanism," ASME J. Mech. Rob., **14**(2), p. 021002.

[58] Arsenault, M., 2011, "Stiffness Analysis of a 2DOF Planar Tensegrity Mechanism," ASME J. Mech. Rob., **3**(2), p. 021011.

5 ANALYTICAL DEFINITIONS FOR TENSEGRITY PRISMS

The article entitled "Analytical definitions of connectivity, incidence and node matrices for t-struts tensegrity prisms" (Paiva *et al.*, 2024b) is presented in this chapter. It is authored by Victor A. S. M. Paiva, Jaime H. Izuka and Paulo R. G. Kurka and is presented with permission from Elsevier (Appendix B). The paper has been published in the Mechanics Research Communications journal, vol. 137, p. 104271, 2024. DOI: 10.1016/j.mechrescom.2024.104271.

This paper addresses a common gap in the literature regarding the structural analysis of regular tensegrity prism modules. While numerous research articles have explored these modules, particularly in forming grids and towers, they often define connectivity and node matrices specific to their entire structures. However, a general definition applicable to the basic modules themselves has not been formally established. This paper formalizes sets of definitions for the connectivity, incidence, and node matrices that are valid for any tensegrity prism formed by four or more struts. The definitions are grounded in geometry and offer simple, general formulations by applying floor and ceiling operators. Additionally, the paper covers both clockwise and counterclockwise rotated modules, providing a comprehensive framework for these structures.

Chapter 7 includes a discussion that integrates this paper with the rest of the thesis and its importance to complete the development of the paper discussed in Chapter 6.

Mechanics Research Communications 137 (2024) 104271

Contents lists available at ScienceDirect

Mechanics Research Communications

journal homepage: www.elsevier.com/locate/mechrescom

Analytical definitions of connectivity, incidence and node matrices for t-struts tensegrity prisms

Victor A.S.M. Paiva [a,*], Paulo R.G. Kurka [a], Jaime H. Izuka [b]

[a] Faculdade de Engenharia Mecânica, Universidade Estadual de Campinas, Rua Mendeleyev, 200, Campinas, 13083-860, SP, Brazil
[b] Faculdade de Ciências Aplicadas, Universidade Estadual de Campinas, Rua Pedro Zaccaria, 1300, Campinas, 13484-350, SP, Brazil

ARTICLE INFO

Keywords:
Tensegrity
Analytical
Floor
Ceiling

ABSTRACT

Regular tensegrity prism modules are widely used by researchers. Numerous research articles combine them to form grids and towers under various assembly strategies. Most of them define connectivity and node matrices that satisfy their structures as a whole, but a general definition for the basic modules has not been formally reported. This paper formalizes sets of definitions for the connectivity, incidence, and node matrices that are valid for any tensegrity prism formed by four struts or more. The definitions are based on geometry and provide simple and general formulations by applying floor and ceiling operators. Both clockwise and counterclockwise rotated modules are covered.

1. Introduction

Tensegrity systems are formed by a set of cables in traction and rigid bodies (usually struts) in compression. They have been availed for numerous innovative applications, such as earthquake-proof and wind resistant constructions [1], solar modules [2], wave energy harvesting [3], space lander [4], animal mimicking [5] and morphing airfoil [6], as well as traditional uses in robots [7], beams [8] and bridges [9,10], for example. Therefore, tensegrity structures have significant scientific value.

Prismatic or cylindrical tensegrity structures are formed by two polygonal parallel bases. A regular t-struts prism is formed by two t-sided polygons, formed by t cables each, connected by t struts and t vertical cables. These modules can also be called triplex, quadruplex... t-plex, according to the number of struts [11]. Tensegrity prism modules have been widely explored [12–15]. Many researchers combine them to assemble masts [16] and grids [17]. The number of struts in a tensegrity prism assigns it a specific shape, leading to associated node and connectivity matrices. The community has applied modules with 3-struts (triplex) [16,18], 4-struts (quadruplex) [10,17,19], 5-struts (pentaplex) [10], 6-struts [10] and so forth. Even though most articles define their node and connectivity matrices, only a few researchers have investigated the derivation of general definitions for node and connectivity matrices. Node positions can be generated by popular form-finding techniques, such as force density [20], dynamic relaxation [21] and kinematical methods [22], but most of them require a connectivity matrix as an input. The adapted force density approach presented in [23] can be applied to model T-4 tensegrity structures, which include regular prisms such as the quadruplex module that appears in several studies. However, it applies numerical procedures to generate the connectivity matrix and then checks which members are bars or cables. An analytical approach that builds it directly from geometry could be more efficient. This challenge is partially solved, the methodology to obtain the connectivity of a 3-struts tensegrity prism is covered in [24]. Also, they assemble a global connectivity matrix for combinations of 3-struts prisms, either stacked to form towers or aligned to build grids. The reach of that work is extended in [25], where they derive a general definition for the node matrix of tensegrity plates of any complexity formed by 3-struts prisms. In addition, they cover assembles of reinforced 3-struts prisms, with extra cables to increase stiffness. Still, analytical definitions for node and connectivity matrices that satisfy prisms with more than three struts are missing.

The stiffness matrix can be obtained from node and connectivity matrices [26], but research groups from other fields, such as materials science [27] and biomechanics [28], may prefer to apply the finite element method (FEM). FEM usually requires an incidence matrix, which carries the same information as the connectivity matrix, but is rarely provided in tensegrity research papers. This paper provides analytical definitions of node (Section 2), incidence (Section 3), and connectivity (Section 4) matrices covering t-struts tensegrity prisms in both clockwise and counterclockwise rotations with $t > 3$. These definitions apply floor and ceiling operators, which have not been explored by the community in tensegrity related research, but provide a convenient manner to analytically work with indexes and favor later implementation.

* Corresponding author.
E-mail address: v140962@dac.unicamp.br (V.A.S.M. Paiva).

https://doi.org/10.1016/j.mechrescom.2024.104271
Received 10 February 2024; Received in revised form 11 March 2024; Accepted 29 March 2024
Available online 30 March 2024

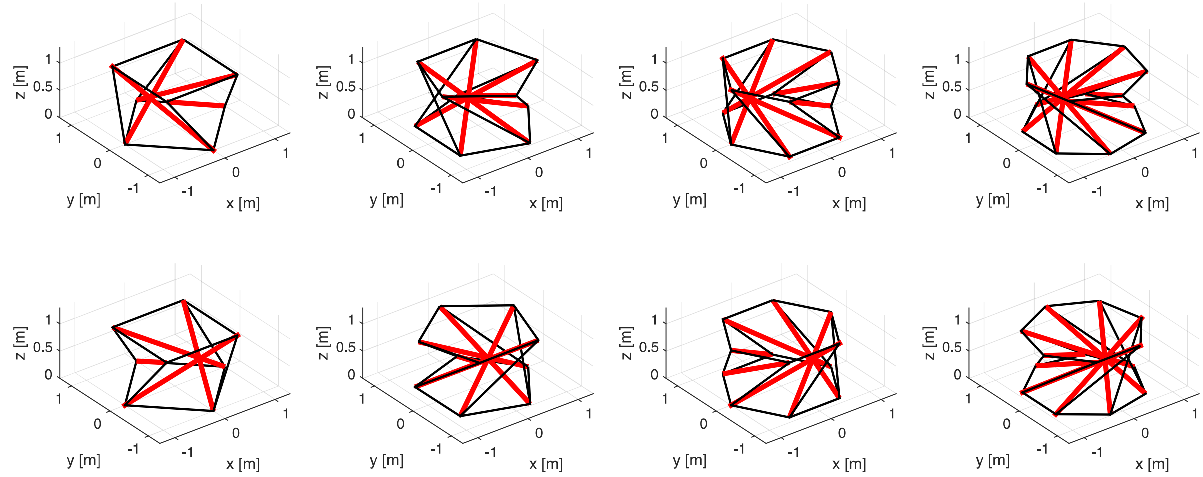

Fig. 1. Regular tensegrity prisms formed by 4 to 7 struts in clockwise (upper row) and counterclockwise (bottom row) rotations.

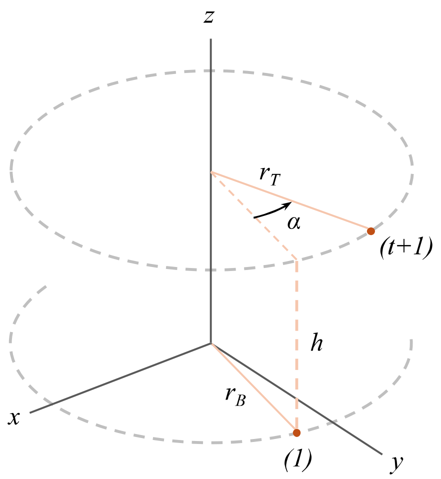

Fig. 2. Scheme of a tensegrity prism highlighting the twist angle formed between node 1 and the projection of node (t+1).

1.1. Limitations and assumptions

The proposed methodology generates a viable structure for $t = 3$, but the rotation inverts, i.e. the clockwise formulation generates a counterclockwise module and vice versa. Therefore, the lower limit is defined as $t > 3$. Also, the upper limit is not covered in this paper, as it is mostly imposed by construction parameters rather than geometrical relations. Static and material parameters, such as mass, stiffness and pre-stress, are not considered in this methodology, the equations shown in this work derive from geometry and pattern recognition. The following assumptions are taken:

1. Top or bottom base nodes are coplanar and concentric.
2. Top and bottom bases are parallel.
3. Both bases are formed by regular t-sided polygons.
4. All members are thin and do not clash.

2. Node matrix

The top base of a cylindrical tensegrity is rotated relative to its bottom base. The rotation can be clockwise (or right-handed) and counterclockwise (or left-handed [29]). Fig. 1 shows examples of tensegrity prisms under both rotations, where thick and light lines stand for bars and cables, respectively. The twist angle α that stabilizes a t-struts prism is $\alpha = \frac{\pi}{2} - \frac{\pi}{t}$ [30]. The bottom $\mathbf{N_B}$ and top $\mathbf{N_T}$ node coordinates are defined by Eqs. (1) and (2), where r_B and r_T are the bottom and top base radii, h is the height of the prism, and $\mathbf{n_i}$ (Eq. (3)) defines the node coordinates of the ith node. The methodology presented in this section is valid for regular prisms, i.e. prisms whose bases are regular polygons in parallel planes (Fig. 2).

$$\mathbf{N_B} = \begin{bmatrix} \mathbf{n_1} & \mathbf{n_2} & \dots & \mathbf{n_t} \end{bmatrix} \tag{1}$$

$$\mathbf{N_T} = \begin{bmatrix} \mathbf{n_{t+1}} & \mathbf{n_{t+2}} & \dots & \mathbf{n_{2t}} \end{bmatrix} \tag{2}$$

$$\begin{cases} \mathbf{n_i} = \begin{Bmatrix} x_i \\ y_i \\ z_i \end{Bmatrix} = \begin{Bmatrix} r_B cos(\frac{i2\pi}{t}) \\ r_B sin(\frac{i2\pi}{t}) \\ 0 \end{Bmatrix} \text{if } i \le t \\ \mathbf{n_i} = \begin{Bmatrix} x_i \\ y_i \\ z_i \end{Bmatrix} = \begin{Bmatrix} r_T cos(\frac{i2\pi}{t} + \alpha) \\ r_T sin(\frac{i2\pi}{t} + \alpha) \\ h \end{Bmatrix} \text{if } i > t \end{cases} \tag{3}$$

The global nodes matrix $\mathbf{N}$ is assembled by $\mathbf{N} = \begin{bmatrix} \mathbf{N_B} & \mathbf{N_T} \end{bmatrix}$. To obtain the node coordinates of a counterclockwise module, the twist angle is multiplied by -1.

3. Incidence matrix

The global incidence matrix can be split in four $t \times 2$ blocks: bars (Eq. (4)), bottom cables (Eq. (5)), top cables (Eq. (6)) and vertical cables (Eq. (7)). Each line in the incidence matrix indicates the first and second nodes connected by their associated element. The vertical cables connect a bottom to a top base nodes, but it is important to alert that their orientation are usually inclined and may even be horizontal in non-regular tensegrity prisms.

Incidence matrices derive from inspection of the pattern of connecting elements. In a clockwise 5-struts tensegrity (Fig. 3), a bar connects the top node 6 to the bottom node 4, while in a 6-struts prism (Fig. 4), the top node 7 also connects to the bottom node 4 by a strut. The top node can be easily inferred as $t + 1$ to lead to 6 when $t = 5$ and to 7 when $t = 6$. But the bottom node poses a challenge to assemble a single mathematical function that satisfies both cases. Floor and ceiling functions are helpful to solve this issue, the floor operator $\lfloor x \rfloor$ rounds a real number x to the largest integer less than or equal to x, while the ceiling operator $\lceil x \rceil$ rounds a real number x to the lowest integer greater than or equal to x. In the example, $\lfloor 5/2 \rfloor = 2$ and $\lceil 5/2 \rceil = 3$.

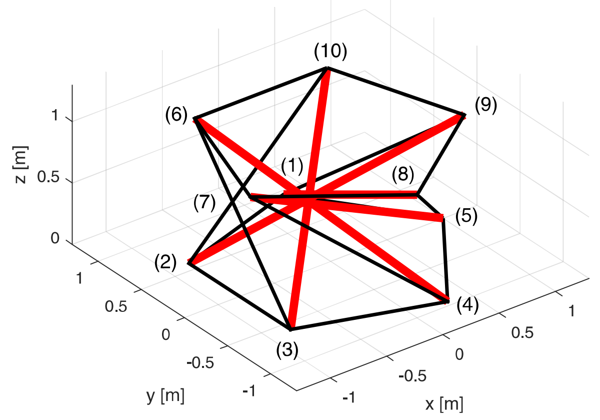

Fig. 3. Example of a clockwise 5-struts tensegrity prism. Node numbers are highlighted.

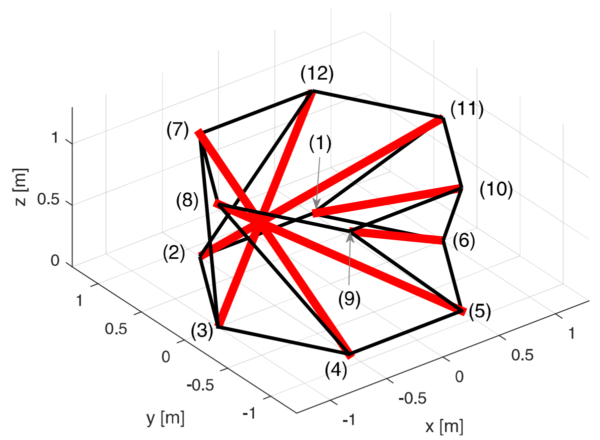

Fig. 4. Example of a clockwise 6-struts tensegrity prism. Node numbers are highlighted.

Therefore, the bottom node, which must be 4 for both $t = 5$ and $t = 6$, can be defined as $\lceil t/2 \rceil + 1$, resulting $\lceil 5/2 \rceil + 1 = 4$ and $\lceil 6/2 \rceil + 1 = 4$. The next incidences sum 1 in both indexes until the bottom node reaches its maximum (t), then it starts counting from 1.

$$\mathbf{I_B} = \begin{bmatrix} \mathbf{I_{B1}} \\ \mathbf{I_{B2}} \\ \vdots \\ \mathbf{I_{B\lfloor t/2 \rfloor}} \\ \mathbf{I_{B\lfloor t/2 \rfloor+1}} \\ \mathbf{I_{B\lfloor t/2 \rfloor+2}} \\ \vdots \\ \mathbf{I_{Bt}} \end{bmatrix} = \begin{bmatrix} t+1 & \lceil t/2 \rceil + 1 \\ t+2 & \lceil t/2 \rceil + 2 \\ \vdots & \\ \lfloor t/2 \rfloor + t & t \\ \lfloor t/2 \rfloor + t + 1 & 1 \\ \lfloor t/2 \rfloor + t + 2 & 2 \\ \vdots & \\ 2t & \lceil t/2 \rceil \end{bmatrix} \tag{4}$$

$$\mathbf{I_{BC}} = \begin{bmatrix} \mathbf{I_{BC1}} \\ \mathbf{I_{BC2}} \\ \vdots \\ \mathbf{I_{BCt-1}} \\ \mathbf{I_{BCt}} \end{bmatrix} = \begin{bmatrix} 1 & 2 \\ 2 & 3 \\ \vdots & \\ t-1 & t \\ t & 1 \end{bmatrix} \tag{5}$$

$$\mathbf{I_{TC}} = \begin{bmatrix} \mathbf{I_{TC1}} \\ \mathbf{I_{TC2}} \\ \vdots \\ \mathbf{I_{TCt-1}} \\ \mathbf{I_{TCt}} \end{bmatrix} = \begin{bmatrix} t+1 & t+2 \\ t+2 & t+3 \\ \vdots & \\ 2t-1 & 2t \\ 2t & t+1 \end{bmatrix} \tag{6}$$

$$\mathbf{I_{VC}} = \begin{bmatrix} \mathbf{I_{VC1}} \\ \mathbf{I_{VC2}} \\ \vdots \\ \mathbf{I_{VC\lfloor t/2 \rfloor+1}} \\ \mathbf{I_{VC\lfloor t/2 \rfloor+2}} \\ \mathbf{I_{VC\lfloor t/2 \rfloor+3}} \\ \vdots \\ \mathbf{I_{VCt}} \end{bmatrix} = \begin{bmatrix} \lceil t/2 \rceil & t+1 \\ \lceil t/2 \rceil + 1 & t+2 \\ \vdots & \\ t & \lfloor t/2 \rfloor + t + 1 \\ 1 & \lfloor t/2 \rfloor + t + 2 \\ 2 & \lfloor t/2 \rfloor + t + 3 \\ \vdots & \\ \lceil t/2 \rceil - 1 & 2t \end{bmatrix} \tag{7}$$

These equations cover the clockwise case. The incidences of bars $\mathbf{I_B}$ and vertical cables $\mathbf{I_{VC}}$ are defined in Eqs. (8) and (9) for counterclockwise tensegrity prisms.

$$\mathbf{I_B} = \begin{bmatrix} \mathbf{I_{B1}} \\ \mathbf{I_{B2}} \\ \vdots \\ \mathbf{I_{B\lceil t/2 \rceil}} \\ \mathbf{I_{B\lceil t/2 \rceil+1}} \\ \mathbf{I_{B\lceil t/2 \rceil+2}} \\ \vdots \\ \mathbf{I_{Bt}} \end{bmatrix} = \begin{bmatrix} t+1 & \lfloor t/2 \rfloor + 1 \\ t+2 & \lfloor t/2 \rfloor + 2 \\ \vdots & \\ \lceil t/2 \rceil + t & t \\ \lceil t/2 \rceil + t + 1 & 1 \\ \lceil t/2 \rceil + t + 2 & 2 \\ \vdots & \\ 2t & \lfloor t/2 \rfloor \end{bmatrix} \tag{8}$$

$$\mathbf{I_{VC}} = \begin{bmatrix} \mathbf{I_{VC1}} \\ \mathbf{I_{VC2}} \\ \vdots \\ \mathbf{I_{VC\lceil t/2 \rceil-1}} \\ \mathbf{I_{VC\lceil t/2 \rceil}} \\ \mathbf{I_{VC\lceil t/2 \rceil+1}} \\ \vdots \\ \mathbf{I_{VCt}} \end{bmatrix} = \begin{bmatrix} \lfloor t/2 \rfloor + 2 & t+1 \\ \lfloor t/2 \rfloor + 3 & t+2 \\ \vdots & \\ t & \lceil t/2 \rceil + t - 1 \\ 1 & \lceil t/2 \rceil + t \\ 2 & \lceil t/2 \rceil + t + 1 \\ \vdots & \\ \lfloor t/2 \rfloor + 1 & 2t \end{bmatrix} \tag{9}$$

Note that $t = 3$ leads to $\alpha = \frac{\pi}{6}$, with n_5 in the fourth quadrant connected to n_1 in the second quadrant by a bar. Conversely, for all configurations with $t > 3$, n_1 resides in the first quadrant, connected by a bar to a top node in the fourth quadrant. This characteristic generates an inverted rotation in 3-strut prisms.

4. Connectivity matrix

The connectivity matrix $\mathbf{C}$ carries the same information as the incidence matrix, but in a different manner. It is composed of connectivity vectors $\mathbf{c}$ (Eq. (10)), each representing a member of the structure. The connectivity vectors are $2t$ long and filled with zeros except for two positions, which are replaced by -1 and 1 indicating the first and second nodes connected by that member. Therefore, each connectivity vector can be built by combining two $2t$ long unit vectors $\mathbf{e_i}$, which are filled with zeros and contain 1 in the ith position.

$$\mathbf{C}^\mathrm{T} = \begin{bmatrix} \mathbf{c_1} & \mathbf{c_2} & \dots & \mathbf{c_{4t}} \end{bmatrix} \tag{10}$$

The global connectivity matrix $\mathbf{C}$ can be split in four $t \times 2t$ blocks: bars (Eq. (11)), bottom cables (Eq. (12)), top cables (Eq. (13)) and vertical cables (Eq. (14)).

$$\mathbf{C_B} = \begin{bmatrix} \mathbf{c_{B1}}^T \\ \mathbf{c_{B2}}^T \\ \vdots \\ \mathbf{c_{B\lfloor t/2 \rfloor}}^T \\ \mathbf{c_{B\lfloor t/2 \rfloor+1}}^T \\ \mathbf{c_{B\lfloor t/2 \rfloor+2}}^T \\ \vdots \\ \mathbf{c_{Bt}}^T \end{bmatrix} = \begin{bmatrix} \left[\mathbf{e_{\lceil t/2 \rceil+1}} - \mathbf{e_{t+1}}\right]^T \\ \left[\mathbf{e_{\lceil t/2 \rceil+2}} - \mathbf{e_{t+2}}\right]^T \\ \vdots \\ \left[\mathbf{e_t} - \mathbf{e_{\lfloor t/2 \rfloor+t}}\right]^T \\ \left[\mathbf{e_1} - \mathbf{e_{\lfloor t/2 \rfloor+t+1}}\right]^T \\ \left[\mathbf{e_2} - \mathbf{e_{\lfloor t/2 \rfloor+t+2}}\right]^T \\ \vdots \\ \left[\mathbf{e_{\lceil t/2 \rceil}} - \mathbf{e_{2t}}\right]^T \end{bmatrix} \tag{11}$$

$$\mathbf{C_{BC}} = \begin{bmatrix} \mathbf{c_{BC1}}^T \\ \mathbf{c_{BC2}}^T \\ \vdots \\ \mathbf{c_{BCt-1}}^T \\ \mathbf{c_{BCt}}^T \end{bmatrix} = \begin{bmatrix} \left[\mathbf{e_2} - \mathbf{e_1}\right]^T \\ \left[\mathbf{e_3} - \mathbf{e_2}\right]^T \\ \vdots \\ \left[\mathbf{e_t} - \mathbf{e_{t-1}}\right]^T \\ \left[\mathbf{e_1} - \mathbf{e_t}\right]^T \end{bmatrix} \tag{12}$$

$$\mathbf{C_{BT}} = \begin{bmatrix} \mathbf{c_{TC1}}^T \\ \mathbf{c_{TC2}}^T \\ \vdots \\ \mathbf{c_{TCt-1}}^T \\ \mathbf{c_{TCt}}^T \end{bmatrix} = \begin{bmatrix} \left[\mathbf{e_{t+2}} - \mathbf{e_{t+1}}\right]^T \\ \left[\mathbf{e_{t+3}} - \mathbf{e_{t+2}}\right]^T \\ \vdots \\ \left[\mathbf{e_{2t}} - \mathbf{e_{2t-1}}\right]^T \\ \left[\mathbf{e_{t+1}} - \mathbf{e_{2t}}\right]^T \end{bmatrix} \tag{13}$$

$$\mathbf{C_{VC}} = \begin{bmatrix} \mathbf{c_{VC1}}^T \\ \mathbf{c_{VC2}}^T \\ \vdots \\ \mathbf{c_{VC\lfloor t/2 \rfloor+1}}^T \\ \mathbf{c_{VC\lfloor t/2 \rfloor+2}}^T \\ \mathbf{c_{VC\lfloor t/2 \rfloor+3}}^T \\ \vdots \\ \mathbf{c_{VCt}}^T \end{bmatrix} = \begin{bmatrix} \left[\mathbf{e_{t+1}} - \mathbf{e_{\lceil t/2 \rceil}}\right]^T \\ \left[\mathbf{e_{t+2}} - \mathbf{e_{\lceil t/2 \rceil+1}}\right]^T \\ \vdots \\ \left[\mathbf{e_{\lfloor t/2 \rfloor+t+1}} - \mathbf{e_t}\right]^T \\ \left[\mathbf{e_{\lfloor t/2 \rfloor+t+2}} - \mathbf{e_1}\right]^T \\ \left[\mathbf{e_{\lfloor t/2 \rfloor+t+3}} - \mathbf{e_2}\right]^T \\ \vdots \\ \left[\mathbf{e_{2t}} - \mathbf{e_{\lceil t/2 \rceil-1}}\right]^T \end{bmatrix} \tag{14}$$

The bar $\mathbf{C_B}$ and vertical cable $\mathbf{C_{VC}}$ connectivities of a counterclockwise module are defined in Eqs. (15) and (16).

$$\mathbf{C_B} = \begin{bmatrix} \mathbf{c_{B1}}^T \\ \mathbf{c_{B2}}^T \\ \vdots \\ \mathbf{c_{B\lceil t/2 \rceil}}^T \\ \mathbf{c_{B\lceil t/2 \rceil+1}}^T \\ \mathbf{c_{B\lceil t/2 \rceil+2}}^T \\ \vdots \\ \mathbf{c_{Bt}}^T \end{bmatrix} = \begin{bmatrix} \left[\mathbf{e_{\lfloor t/2 \rfloor+1}} - \mathbf{e_{t+1}}\right]^T \\ \left[\mathbf{e_{\lfloor t/2 \rfloor+2}} - \mathbf{e_{t+2}}\right]^T \\ \vdots \\ \left[\mathbf{e_t} - \mathbf{e_{\lceil t/2 \rceil+t}}\right]^T \\ \left[\mathbf{e_1} - \mathbf{e_{\lceil t/2 \rceil+t+1}}\right]^T \\ \left[\mathbf{e_2} - \mathbf{e_{\lceil t/2 \rceil+t+2}}\right]^T \\ \vdots \\ \left[\mathbf{e_{\lfloor t/2 \rfloor}} - \mathbf{e_{2t}}\right]^T \end{bmatrix} \tag{15}$$

$$\mathbf{C_{VC}} = \begin{bmatrix} \mathbf{c_{VC1}}^T \\ \mathbf{c_{VC2}}^T \\ \vdots \\ \mathbf{c_{VC\lceil t/2 \rceil-1}}^T \\ \mathbf{c_{VC\lceil t/2 \rceil}}^T \\ \mathbf{c_{VC\lceil t/2 \rceil+1}}^T \\ \vdots \\ \mathbf{c_{VCt}}^T \end{bmatrix} = \begin{bmatrix} \left[\mathbf{e_{t+1}} - \mathbf{e_{\lfloor t/2 \rfloor+2}}\right]^T \\ \left[\mathbf{e_{t+2}} - \mathbf{e_{\lfloor t/2 \rfloor+3}}\right]^T \\ \vdots \\ \left[\mathbf{e_{\lceil t/2 \rceil+t-1}} - \mathbf{e_t}\right]^T \\ \left[\mathbf{e_{\lceil t/2 \rceil+t}} - \mathbf{e_1}\right]^T \\ \left[\mathbf{e_{\lceil t/2 \rceil+t+1}} - \mathbf{e_2}\right]^T \\ \vdots \\ \left[\mathbf{e_{2t}} - \mathbf{e_{\lfloor t/2 \rfloor+1}}\right]^T \end{bmatrix} \tag{16}$$

5. Conclusions

It has been observed that tensegrity prisms are mostly applied with three or four struts, even on theoretical builds, possibly due to their simpler node and connectivity matrices. The lack of a general and analytical definition of those matrices might have been a bottleneck in the study of prisms with a higher number of struts. This paper brings general definitions for node, connectivity and incidence matrices of t-struts tensegrity prisms with t greater than 3 under clockwise and counterclockwise rotations. These definitions derive from geometry and assume thin members, therefore they do not cover element clashes or stress-related results. Also, examples for 4, 5, 6 and 7-struts prisms are presented. Future research should include the definitions of those matrices for prism assemblies, such as tensegrity towers and grids, and the application of these definitions on form-finding methods.

CRediT authorship contribution statement

Victor A.S.M. Paiva: Writing – review & editing, Writing – original draft, Validation, Methodology, Investigation, Formal analysis, Conceptualization. **Paulo R.G. Kurka:** Writing – review & editing, Validation, Supervision. **Jaime H. Izuka:** Writing – review & editing, Validation, Supervision.

Declaration of competing interest

The authors declare that they have no known competing financial interests or personal relationships that could have appeared to influence the work reported in this paper.

Data availability

No data was used for the research described in the article.

Appendix. Node, incidence and connectivity matrices for $r_B = r_T = h = 1m$ and $t \in [4, 5, 6, 7]$

This appendix covers popular arrangements studied by the community, but the formulae developed in this study are not limited to the results presented in this section. Node (Table A.1), incidence (Tables A.2–A.5) and connectivity (Tables A.6–A.9) matrices for $r_B = r_T = h = 1m$ and $t \in [4, 5, 6, 7]$ are presented for both clockwise (CW) and counterclockwise (CCW) configurations.

Table A.1
Transpose node matrices for $t \in [4, 5, 6, 7]$ in CW and CCW rotations.

t	$\mathbf{N_B^T}$	$\mathbf{N_T^T}$ CW	$\mathbf{N_T^T}$ CCW
4	$\begin{bmatrix} 0.000 & 1.000 & 0 \\ -1.000 & 0.000 & 0 \\ 0.000 & -1.000 & 0 \\ 1.000 & -0.000 & 0 \end{bmatrix}$	$\begin{bmatrix} -0.707 & 0.707 & 1 \\ -0.707 & -0.707 & 1 \\ 0.707 & -0.707 & 1 \\ 0.707 & 0.707 & 1 \end{bmatrix}$	$\begin{bmatrix} 0.707 & 0.707 & 1 \\ -0.707 & 0.707 & 1 \\ -0.707 & -0.707 & 1 \\ 0.707 & -0.707 & 1 \end{bmatrix}$
5	$\begin{bmatrix} 0.309 & 0.951 & 0 \\ -0.809 & 0.588 & 0 \\ -0.809 & -0.588 & 0 \\ 0.309 & -0.951 & 0 \\ 1.000 & -0.000 & 0 \end{bmatrix}$	$\begin{bmatrix} -0.588 & 0.809 & 1 \\ -0.951 & -0.309 & 1 \\ -0.000 & -1.000 & 1 \\ 0.951 & -0.309 & 1 \\ 0.588 & 0.809 & 1 \end{bmatrix}$	$\begin{bmatrix} 0.951 & 0.309 & 1 \\ 0.000 & 1.000 & 1 \\ -0.951 & 0.309 & 1 \\ -0.588 & -0.809 & 1 \\ 0.588 & -0.809 & 1 \end{bmatrix}$
6	$\begin{bmatrix} 0.500 & 0.866 & 0 \\ -0.500 & 0.866 & 0 \\ -1.000 & 0.000 & 0 \\ -0.500 & -0.866 & 0 \\ 0.500 & -0.866 & 0 \\ 1.000 & 0.000 & 0 \end{bmatrix}$	$\begin{bmatrix} -0.500 & 0.866 & 1 \\ -1.000 & 0.000 & 1 \\ -0.500 & -0.866 & 1 \\ 0.500 & -0.866 & 1 \\ 1.000 & -0.000 & 1 \\ 0.500 & 0.866 & 1 \end{bmatrix}$	$\begin{bmatrix} 1.000 & 0.000 & 1 \\ 0.500 & 0.866 & 1 \\ -0.500 & 0.866 & 1 \\ -1.000 & 0.000 & 1 \\ -0.500 & -0.866 & 1 \\ 0.500 & -0.866 & 1 \end{bmatrix}$
7	$\begin{bmatrix} 0.624 & 0.782 & 0 \\ -0.223 & 0.975 & 0 \\ -0.901 & 0.434 & 0 \\ -0.901 & -0.434 & 0 \\ -0.223 & -0.975 & 0 \\ 0.624 & -0.782 & 0 \\ 1.000 & 0.000 & 0 \end{bmatrix}$	$\begin{bmatrix} -0.434 & 0.901 & 1 \\ -0.975 & 0.223 & 1 \\ -0.782 & -0.624 & 1 \\ 0.000 & -1.000 & 1 \\ 0.782 & -0.624 & 1 \\ 0.975 & 0.223 & 1 \\ 0.434 & 0.901 & 1 \end{bmatrix}$	$\begin{bmatrix} 0.975 & -0.223 & 1 \\ 0.782 & 0.624 & 1 \\ 0.000 & 1.000 & 1 \\ -0.782 & 0.624 & 1 \\ -0.975 & -0.223 & 1 \\ -0.434 & -0.901 & 1 \\ 0.434 & -0.901 & 1 \end{bmatrix}$

Table A.2
Incidence matrices for a 4-struts tensegrity prism.

$\mathbf{I_B}$ CW	$\mathbf{I_B}$ CCW	$\mathbf{I_{TC}}$	$\mathbf{I_{BC}}$	$\mathbf{I_{VC}}$ CW	$\mathbf{I_{VC}}$ CCW
$\begin{bmatrix} 5 & 3 \\ 6 & 4 \\ 7 & 1 \\ 8 & 2 \end{bmatrix}$	$\begin{bmatrix} 5 & 3 \\ 6 & 4 \\ 7 & 1 \\ 8 & 2 \end{bmatrix}$	$\begin{bmatrix} 5 & 6 \\ 6 & 7 \\ 7 & 8 \\ 8 & 5 \end{bmatrix}$	$\begin{bmatrix} 1 & 2 \\ 2 & 3 \\ 3 & 4 \\ 4 & 1 \end{bmatrix}$	$\begin{bmatrix} 2 & 5 \\ 3 & 6 \\ 4 & 7 \\ 1 & 8 \end{bmatrix}$	$\begin{bmatrix} 4 & 5 \\ 1 & 6 \\ 2 & 7 \\ 3 & 8 \end{bmatrix}$

Table A.3
Incidence matrices for a 5-struts tensegrity prism.

$\mathbf{I_B}$ CW	$\mathbf{I_B}$ CCW	$\mathbf{I_{TC}}$	$\mathbf{I_{BC}}$	$\mathbf{I_{VC}}$ CW	$\mathbf{I_{VC}}$ CCW
$\begin{bmatrix} 6 & 4 \\ 7 & 5 \\ 8 & 1 \\ 9 & 2 \\ 10 & 3 \end{bmatrix}$	$\begin{bmatrix} 6 & 3 \\ 7 & 4 \\ 8 & 5 \\ 9 & 1 \\ 10 & 2 \end{bmatrix}$	$\begin{bmatrix} 6 & 7 \\ 7 & 8 \\ 8 & 9 \\ 9 & 10 \\ 10 & 6 \end{bmatrix}$	$\begin{bmatrix} 1 & 2 \\ 2 & 3 \\ 3 & 4 \\ 4 & 5 \\ 5 & 1 \end{bmatrix}$	$\begin{bmatrix} 3 & 6 \\ 4 & 7 \\ 5 & 8 \\ 1 & 9 \\ 2 & 10 \end{bmatrix}$	$\begin{bmatrix} 4 & 6 \\ 5 & 7 \\ 1 & 8 \\ 2 & 9 \\ 3 & 10 \end{bmatrix}$

Table A.4
Incidence matrices for a 6-struts tensegrity prism.

$\mathbf{I_B}$ CW	$\mathbf{I_B}$ CCW	$\mathbf{I_{TC}}$	$\mathbf{I_{BC}}$	$\mathbf{I_{VC}}$ CW	$\mathbf{I_{VC}}$ CCW
$\begin{bmatrix} 7 & 4 \\ 8 & 5 \\ 9 & 6 \\ 10 & 1 \\ 11 & 2 \\ 12 & 3 \end{bmatrix}$	$\begin{bmatrix} 7 & 4 \\ 8 & 5 \\ 9 & 6 \\ 10 & 1 \\ 11 & 2 \\ 12 & 3 \end{bmatrix}$	$\begin{bmatrix} 7 & 8 \\ 8 & 9 \\ 9 & 10 \\ 10 & 11 \\ 11 & 12 \\ 12 & 7 \end{bmatrix}$	$\begin{bmatrix} 1 & 2 \\ 2 & 3 \\ 3 & 4 \\ 4 & 5 \\ 5 & 6 \\ 6 & 1 \end{bmatrix}$	$\begin{bmatrix} 3 & 7 \\ 4 & 8 \\ 5 & 9 \\ 6 & 10 \\ 1 & 11 \\ 2 & 12 \end{bmatrix}$	$\begin{bmatrix} 5 & 7 \\ 6 & 8 \\ 1 & 9 \\ 2 & 10 \\ 3 & 11 \\ 4 & 12 \end{bmatrix}$

Table A.5
Incidence matrices for a 7-struts tensegrity prism.

$\mathbf{I_B}$ CW	$\mathbf{I_B}$ CCW	$\mathbf{I_{TC}}$	$\mathbf{I_{BC}}$	$\mathbf{I_{VC}}$ CW	$\mathbf{I_{VC}}$ CCW
$\begin{bmatrix} 8 & 5 \\ 9 & 6 \\ 10 & 7 \\ 11 & 1 \\ 12 & 2 \\ 13 & 3 \\ 14 & 4 \end{bmatrix}$	$\begin{bmatrix} 8 & 4 \\ 9 & 5 \\ 10 & 6 \\ 11 & 7 \\ 12 & 1 \\ 13 & 2 \\ 14 & 3 \end{bmatrix}$	$\begin{bmatrix} 8 & 9 \\ 9 & 10 \\ 10 & 11 \\ 11 & 12 \\ 12 & 13 \\ 13 & 14 \\ 14 & 8 \end{bmatrix}$	$\begin{bmatrix} 1 & 2 \\ 2 & 3 \\ 3 & 4 \\ 4 & 5 \\ 5 & 6 \\ 6 & 7 \\ 7 & 1 \end{bmatrix}$	$\begin{bmatrix} 4 & 8 \\ 5 & 9 \\ 6 & 10 \\ 7 & 11 \\ 1 & 12 \\ 2 & 13 \\ 3 & 14 \end{bmatrix}$	$\begin{bmatrix} 5 & 8 \\ 6 & 9 \\ 7 & 10 \\ 1 & 11 \\ 2 & 12 \\ 3 & 13 \\ 4 & 14 \end{bmatrix}$

Table A.6
Transpose connectivity matrices for a 4-struts tensegrity prism.

$\mathbf{C_B}^T$ CW	$\mathbf{C_B}^T$ CCW	$\mathbf{C_{TC}}^T$	$\mathbf{C_{BC}}^T$	$\mathbf{C_{VC}}^T$ CW	$\mathbf{C_{VC}}^T$ CCW
$\begin{bmatrix} [\mathbf{e}_3-\mathbf{e}_5]^T \\ [\mathbf{e}_4-\mathbf{e}_6]^T \\ [\mathbf{e}_1-\mathbf{e}_7]^T \\ [\mathbf{e}_2-\mathbf{e}_8]^T \end{bmatrix}$	$\begin{bmatrix} [\mathbf{e}_3-\mathbf{e}_5]^T \\ [\mathbf{e}_4-\mathbf{e}_6]^T \\ [\mathbf{e}_1-\mathbf{e}_7]^T \\ [\mathbf{e}_2-\mathbf{e}_8]^T \end{bmatrix}$	$\begin{bmatrix} [\mathbf{e}_6-\mathbf{e}_5]^T \\ [\mathbf{e}_7-\mathbf{e}_6]^T \\ [\mathbf{e}_8-\mathbf{e}_7]^T \\ [\mathbf{e}_5-\mathbf{e}_8]^T \end{bmatrix}$	$\begin{bmatrix} [\mathbf{e}_2-\mathbf{e}_1]^T \\ [\mathbf{e}_3-\mathbf{e}_2]^T \\ [\mathbf{e}_4-\mathbf{e}_3]^T \\ [\mathbf{e}_1-\mathbf{e}_4]^T \end{bmatrix}$	$\begin{bmatrix} [\mathbf{e}_5-\mathbf{e}_2]^T \\ [\mathbf{e}_6-\mathbf{e}_3]^T \\ [\mathbf{e}_7-\mathbf{e}_4]^T \\ [\mathbf{e}_8-\mathbf{e}_1]^T \end{bmatrix}$	$\begin{bmatrix} [\mathbf{e}_5-\mathbf{e}_4]^T \\ [\mathbf{e}_6-\mathbf{e}_1]^T \\ [\mathbf{e}_7-\mathbf{e}_2]^T \\ [\mathbf{e}_8-\mathbf{e}_3]^T \end{bmatrix}$

Table A.7
Transpose connectivity matrices for a 5-struts tensegrity prism.

$\mathbf{C_B}^T$ CW	$\mathbf{C_B}^T$ CCW	$\mathbf{C_{TC}}^T$	$\mathbf{C_{BC}}^T$	$\mathbf{C_{VC}}^T$ CW	$\mathbf{C_{VC}}^T$ CCW
$\begin{bmatrix} [\mathbf{e}_4-\mathbf{e}_6]^T \\ [\mathbf{e}_5-\mathbf{e}_7]^T \\ [\mathbf{e}_1-\mathbf{e}_8]^T \\ [\mathbf{e}_2-\mathbf{e}_9]^T \\ [\mathbf{e}_3-\mathbf{e}_{10}]^T \end{bmatrix}$	$\begin{bmatrix} [\mathbf{e}_4-\mathbf{e}_3]^T \\ [\mathbf{e}_5-\mathbf{e}_4]^T \\ [\mathbf{e}_1-\mathbf{e}_5]^T \\ [\mathbf{e}_2-\mathbf{e}_6]^T \\ [\mathbf{e}_3-\mathbf{e}_7]^T \end{bmatrix}$	$\begin{bmatrix} [\mathbf{e}_6-\mathbf{e}_7]^T \\ [\mathbf{e}_7-\mathbf{e}_8]^T \\ [\mathbf{e}_8-\mathbf{e}_9]^T \\ [\mathbf{e}_9-\mathbf{e}_{10}]^T \\ [\mathbf{e}_{10}-\mathbf{e}_6]^T \end{bmatrix}$	$\begin{bmatrix} [\mathbf{e}_1-\mathbf{e}_2]^T \\ [\mathbf{e}_2-\mathbf{e}_3]^T \\ [\mathbf{e}_3-\mathbf{e}_4]^T \\ [\mathbf{e}_4-\mathbf{e}_5]^T \\ [\mathbf{e}_5-\mathbf{e}_1]^T \end{bmatrix}$	$\begin{bmatrix} [\mathbf{e}_3-\mathbf{e}_6]^T \\ [\mathbf{e}_4-\mathbf{e}_7]^T \\ [\mathbf{e}_5-\mathbf{e}_8]^T \\ [\mathbf{e}_1-\mathbf{e}_9]^T \\ [\mathbf{e}_2-\mathbf{e}_{10}]^T \end{bmatrix}$	$\begin{bmatrix} [\mathbf{e}_5-\mathbf{e}_6]^T \\ [\mathbf{e}_6-\mathbf{e}_7]^T \\ [\mathbf{e}_1-\mathbf{e}_8]^T \\ [\mathbf{e}_2-\mathbf{e}_9]^T \\ [\mathbf{e}_3-\mathbf{e}_{10}]^T \end{bmatrix}$

Table A.8
Transpose connectivity matrices for a 6-struts tensegrity prism.

$\mathbf{C_B}^T$ CW	$\mathbf{C_B}^T$ CCW	$\mathbf{C_{TC}}^T$	$\mathbf{C_{BC}}^T$	$\mathbf{C_{VC}}^T$ CW	$\mathbf{C_{VC}}^T$ CCW
$\begin{bmatrix} [\mathbf{e}_8-\mathbf{e}_4]^T \\ [\mathbf{e}_9-\mathbf{e}_5]^T \\ [\mathbf{e}_{10}-\mathbf{e}_6]^T \\ [\mathbf{e}_{11}-\mathbf{e}_1]^T \\ [\mathbf{e}_{12}-\mathbf{e}_2]^T \\ [\mathbf{e}_1-\mathbf{e}_3]^T \end{bmatrix}$	$\begin{bmatrix} [\mathbf{e}_8-\mathbf{e}_4]^T \\ [\mathbf{e}_9-\mathbf{e}_5]^T \\ [\mathbf{e}_{10}-\mathbf{e}_6]^T \\ [\mathbf{e}_{11}-\mathbf{e}_1]^T \\ [\mathbf{e}_{12}-\mathbf{e}_2]^T \\ [\mathbf{e}_1-\mathbf{e}_3]^T \end{bmatrix}$	$\begin{bmatrix} [\mathbf{e}_8-\mathbf{e}_7]^T \\ [\mathbf{e}_9-\mathbf{e}_8]^T \\ [\mathbf{e}_{10}-\mathbf{e}_9]^T \\ [\mathbf{e}_{11}-\mathbf{e}_{10}]^T \\ [\mathbf{e}_{12}-\mathbf{e}_{11}]^T \\ [\mathbf{e}_7-\mathbf{e}_{12}]^T \end{bmatrix}$	$\begin{bmatrix} [\mathbf{e}_2-\mathbf{e}_1]^T \\ [\mathbf{e}_3-\mathbf{e}_2]^T \\ [\mathbf{e}_4-\mathbf{e}_3]^T \\ [\mathbf{e}_5-\mathbf{e}_4]^T \\ [\mathbf{e}_6-\mathbf{e}_5]^T \\ [\mathbf{e}_1-\mathbf{e}_6]^T \end{bmatrix}$	$\begin{bmatrix} [\mathbf{e}_6-\mathbf{e}_7]^T \\ [\mathbf{e}_7-\mathbf{e}_8]^T \\ [\mathbf{e}_2-\mathbf{e}_9]^T \\ [\mathbf{e}_3-\mathbf{e}_{10}]^T \\ [\mathbf{e}_4-\mathbf{e}_{11}]^T \\ [\mathbf{e}_5-\mathbf{e}_{12}]^T \end{bmatrix}$	$\begin{bmatrix} [\mathbf{e}_7-\mathbf{e}_5]^T \\ [\mathbf{e}_8-\mathbf{e}_6]^T \\ [\mathbf{e}_9-\mathbf{e}_1]^T \\ [\mathbf{e}_{10}-\mathbf{e}_2]^T \\ [\mathbf{e}_{11}-\mathbf{e}_3]^T \\ [\mathbf{e}_{12}-\mathbf{e}_4]^T \end{bmatrix}$

Table A.9
Transpose connectivity matrices for a 7-struts tensegrity prism.

$\mathbf{C_B}^T$ CW	$\mathbf{C_B}^T$ CCW	$\mathbf{C_{TC}}^T$	$\mathbf{C_{BC}}^T$	$\mathbf{C_{VC}}^T$ CW	$\mathbf{C_{VC}}^T$ CCW
$\begin{bmatrix} [\mathbf{e}_{13}-\mathbf{e}_8]^T \\ [\mathbf{e}_{14}-\mathbf{e}_5]^T \\ [\mathbf{e}_1-\mathbf{e}_6]^T \\ [\mathbf{e}_2-\mathbf{e}_7]^T \\ [\mathbf{e}_3-\mathbf{e}_8]^T \\ [\mathbf{e}_4-\mathbf{e}_9]^T \end{bmatrix}$	$\begin{bmatrix} [\mathbf{e}_{14}-\mathbf{e}_8]^T \\ [\mathbf{e}_1-\mathbf{e}_9]^T \\ [\mathbf{e}_2-\mathbf{e}_{10}]^T \\ [\mathbf{e}_3-\mathbf{e}_{11}]^T \\ [\mathbf{e}_4-\mathbf{e}_{12}]^T \\ [\mathbf{e}_5-\mathbf{e}_{13}]^T \\ [\mathbf{e}_6-\mathbf{e}_{14}]^T \end{bmatrix}$	$\begin{bmatrix} [\mathbf{e}_9-\mathbf{e}_8]^T \\ [\mathbf{e}_{10}-\mathbf{e}_9]^T \\ [\mathbf{e}_{11}-\mathbf{e}_{10}]^T \\ [\mathbf{e}_{12}-\mathbf{e}_{11}]^T \\ [\mathbf{e}_{13}-\mathbf{e}_{12}]^T \\ [\mathbf{e}_{14}-\mathbf{e}_{13}]^T \\ [\mathbf{e}_8-\mathbf{e}_{14}]^T \end{bmatrix}$	$\begin{bmatrix} [\mathbf{e}_2-\mathbf{e}_1]^T \\ [\mathbf{e}_3-\mathbf{e}_2]^T \\ [\mathbf{e}_4-\mathbf{e}_3]^T \\ [\mathbf{e}_5-\mathbf{e}_4]^T \\ [\mathbf{e}_6-\mathbf{e}_5]^T \\ [\mathbf{e}_7-\mathbf{e}_6]^T \\ [\mathbf{e}_1-\mathbf{e}_7]^T \end{bmatrix}$	$\begin{bmatrix} [\mathbf{e}_{12}-\mathbf{e}_4]^T \\ [\mathbf{e}_{13}-\mathbf{e}_5]^T \\ [\mathbf{e}_{14}-\mathbf{e}_6]^T \\ [\mathbf{e}_7-\mathbf{e}_1]^T \\ [\mathbf{e}_8-\mathbf{e}_2]^T \\ [\mathbf{e}_9-\mathbf{e}_3]^T \\ [\mathbf{e}_{10}-\mathbf{e}_4]^T \end{bmatrix}$	$\begin{bmatrix} [\mathbf{e}_8-\mathbf{e}_5]^T \\ [\mathbf{e}_9-\mathbf{e}_6]^T \\ [\mathbf{e}_{10}-\mathbf{e}_7]^T \\ [\mathbf{e}_{11}-\mathbf{e}_1]^T \\ [\mathbf{e}_{12}-\mathbf{e}_2]^T \\ [\mathbf{e}_{13}-\mathbf{e}_3]^T \\ [\mathbf{e}_{14}-\mathbf{e}_4]^T \end{bmatrix}$

References

[1] F. Fraternali, J. de Castro Motta, Mechanics of superelastic tensegrity braces for timber frames equipped with buckling-restrained devices, Int. J. Solids Struct. 281 (2023) 112414, http://dx.doi.org/10.1016/j.ijsolstr.2023.112414.

[2] F. Fraternali, J. de Castro Motta, G. Germano, E. Babilio, A. Amendola, Mechanical response of tensegrity-origami solar modules, Appl. Eng. Sci. 17 (2024) 100174, http://dx.doi.org/10.1016/j.apples.2023.100174.

[3] H. Ning, W. Zhou, L. Tuo, C. Liang, C. Chen, S. Li, H. Qu, L. Wan, G. Liu, Tensegrity triboelectric nanogenerator for broadband blue energy harvesting in all-sea areas, Nano Energy 117 (2023) 108906, http://dx.doi.org/10.1016/j.nanoen.2023.108906.

[4] X. Wang, A. Luo, H. Liu, Design and analysis of a double-helix tensegrity spherical lander, Mech. Res. Commun. 129 (2023) 104091, http://dx.doi.org/10.1016/j.mechrescom.2023.104091.

[5] B. Chen, H. Jiang, Swimming performance of a tensegrity robotic fish, Soft Robot. 6 (4) (2019) 520–531, http://dx.doi.org/10.1089/soro.2018.0079.

[6] M. Chen, J. Liu, R.E. Skelton, Design and control of tensegrity morphing airfoils, Mech. Res. Commun. 103 (2020) 103480, http://dx.doi.org/10.1016/j.mechrescom.2020.103480.

[7] Y. Liu, Q. Bi, X. Yue, J. Wu, B. Yang, Y. Li, A review on tensegrity structures-based robots, Mech. Mach. Theory 168 (2022) 104571, http://dx.doi.org/10.1016/j.mechmachtheory.2021.104571.

[8] P.R. Kurka, V.A. Paiva, L.H. Silva-Teixeira, P.G. Ramos, J.H. Izuka, A dynamical model for the control of a guyed tensegrity beam under large displacements, J. Mech. Robot. 16 (9) (2024) http://dx.doi.org/10.1115/1.4064259.

[9] R. Skelton, F. Fraternali, G. Carpentieri, A. Micheletti, Minimum mass design of tensegrity bridges with parametric architecture and multiscale complexity, Mech. Res. Commun. 58 (2014) 124–132, http://dx.doi.org/10.1016/j.mechrescom.2013.10.017.

[10] J. Feron, L. Boucher, V. Denoël, P. Latteur, Optimization of footbridges composed of prismatic tensegrity modules, J. Bridge Eng. 24 (12) (2019) 04019112, http://dx.doi.org/10.1061/(ASCE)BE.1943-5592.0001438.

[11] N. Vassart, R. Motro, Multiparametered formfinding method: application to tensegrity systems, Int. J. Space Struct. 14 (2) (1999) 147–154, http://dx.doi.org/10.1260/0266351991494768.

[12] A. Micheletti, G. Ruscica, F. Fraternali, On the compact wave dynamics of tensegrity beams in multiple dimensions, Nonlinear Dynam. 98 (4) (2019) 2737–2753, http://dx.doi.org/10.1007/s11071-019-04986-8.

[13] X. Xu, Y. Luo, Form-finding of nonregular tensegrities using a genetic algorithm, Mech. Res. Commun. 37 (1) (2010) 85–91, http://dx.doi.org/10.1016/j.mechrescom.2009.09.003.

[14] A. Amendola, G. Carpentieri, M. De Oliveira, R. Skelton, F. Fraternali, Experimental investigation of the softening–stiffening response of tensegrity prisms under compressive loading, Compos. Struct. 117 (2014) 234–243, http://dx.doi.org/10.1016/j.compstruct.2014.06.022.

[15] Y. Ma, Q. Zhang, Y. Dobah, F. Scarpa, F. Fraternali, R.E. Skelton, D. Zhang, J. Hong, Meta-tensegrity: Design of a tensegrity prism with metal rubber, Compos. Struct. 206 (2018) 644–657, http://dx.doi.org/10.1016/j.compstruct.2018.08.067.

[16] H. Furuya, Concept of deployable tensegrity structures in space application, Int. J. Space Struct. 7 (2) (1992) 143–151, http://dx.doi.org/10.1177/026635119200700207.

[17] H.C. Tran, J. Lee, Initial self-stress design of tensegrity grid structures, Comput. Struct. 88 (9–10) (2010) 558–566, http://dx.doi.org/10.1016/j.compstruc.2010.01.011.

[18] F. Fraternali, L. Senatore, C. Daraio, Solitary waves on tensegrity lattices, J. Mech. Phys. Solids 60 (6) (2012) 1137–1144, http://dx.doi.org/10.1016/j.jmps.2012.02.007.

[19] S. Wendling, P. Cañadas, P. Chabrand, Toward a generalised tensegrity model describing the mechanical behaviour of the cytoskeleton structure, Comput. Methods Biomech. Biomed. Eng. 6 (1) (2003) 45–52, http://dx.doi.org/10.1080/1025584021000059413.

[20] J. Zhang, M. Ohsaki, Tensegrity Structures, vol. 7, Springer, 2015, http://dx.doi.org/10.1007/978-4-431-54813-3.

[21] N.B.H. Ali, L. Rhode-Barbarigos, I.F. Smith, Analysis of clustered tensegrity structures using a modified dynamic relaxation algorithm, Int. J. Solids Struct. 48 (5) (2011) 637–647, http://dx.doi.org/10.1016/j.ijsolstr.2010.10.029.

[22] A. Tibert, S. Pellegrino, Review of form-finding methods for tensegrity structures, Int. J. Space Struct. 26 (3) (2011) 241–255, http://dx.doi.org/10.1260/0266-3511.26.3.241.

[23] X. Yu, Y. Yang, Y. Ji, Automatic form-finding of N-4 type tensegrity structures, Lat. Am. J. Solids Struct. 19 (2022) http://dx.doi.org/10.1590/1679-78256735.

[24] K. Nagase, T. Yamashita, N. Kawabata, On a connectivity matrix formula for tensegrity prism plates, Mech. Res. Commun. 77 (2016) 29–43, http://dx.doi.org/10.1016/j.mechrescom.2016.08.003.

[25] S. Jiang, R.E. Skelton, E.A. Peraza Hernandez, Analytical equations for the connectivity matrices and node positions of minimal and extended tensegrity plates, Int. J. Space Struct. 35 (3) (2020) 47–68, http://dx.doi.org/10.1177/0956059920902375.

[26] R.E. Skelton, M. de Oliveira, Tensegrity Systems, Springer US, 2009, pp. 45–72, http://dx.doi.org/10.1007/978-0-387-74242-7.

[27] M. De Angelo, L. Placidi, N. Nejadsadeghi, A. Misra, Non-standard Timoshenko beam model for chiral metamaterial: identification of stiffness parameters, Mech. Res. Commun. 103 (2020) 103462, http://dx.doi.org/10.1016/j.mechrescom.2019.103462.

[28] Y.D. Bansod, T. Matsumoto, K. Nagayama, J. Bursa, A finite element bendo-tensegrity model of eukaryotic cell, J. Biomech. Eng. 140 (10) (2018) 101001, http://dx.doi.org/10.1115/1.4040246.

[29] C. Davini, A. Micheletti, P. Podio-Guidugli, On the impulsive dynamics of T3 tensegrity chains, Meccanica 51 (2016) 2763–2776, http://dx.doi.org/10.1007/s11012-016-0495-y.

[30] R. Connelly, M. Terrell, Globally rigid symmetric tensegrities, Struct. Topol. (1995).

6 FORM-FINDING

The article entitled “A form-finding method for deployable tensegrity arms and inverse kinematics” (Paiva *et al.*, 2024a) is presented in this chapter. It is authored by Victor A. S. M. Paiva, Luis H. Silva-Teixeira, Jaime H. Izuka, Eduardo P. Okabe and Paulo R. G. Kurka and is presented with permission from Springer Nature (Appendix D). The paper has been published in Meccanica, 2024. DOI: 10.1007/s11012-024-01880-5.

This paper explores the development of a form-finding methodology for deployable tensegrity mechanisms composed of cylindrical modules. Using nonlinear programming, the study designs a structure capable of complex shape transformations, such as expanding from a theoretically flat configuration into a tower and bowing into an arch. The work also includes workspace approximation and inverse kinematics using neural networks and optimization algorithms. The methodology is applicable to any stacking of cylindrical tensegrity structures, as demonstrated with a six-quadruplex module example.

Chapter 7 delves deeper into the discussion on the initial guess for the nonlinear programming routine, highlights the importance of alternating the rotation at each level, and presents equations that were omitted in the paper for conciseness.

The MATLAB scripts used in the form-finding method and inverse kinematics are publicly available at <https://github.com/FictorP/Tensegrity/tree/main/formfinding>, including the trained neural network.

Meccanica
https://doi.org/10.1007/s11012-024-01880-5

RESEARCH

A form-finding method for deployable tensegrity arms and inverse kinematics

Victor Paiva · Luis Silva-Teixeira · Jaime Izuka · Eduardo Okabe · Paulo Kurka

Received: 30 June 2024 / Accepted: 7 September 2024

Abstract Manipulator arms in robots can be bulky and difficult to transport. Tensegrity mechanisms, which can be compact, deployed, and shaped to adjustable lengths, offer a promising alternative for robotic manipulators. This work develops a methodology for class 2 tensegrity mechanisms formed by cylindrical modules, using nonlinear programming to design a deployable tower capable of complex shape transformations, such as bowing. The study starts by deploying the structure from a compact shape into a tower, thereby enhancing its transportability and impact resistance. Next, a form-finding procedure assigns a bowing movement to the tower by pulling specific cables, using a kinematical method and nonlinear programming to achieve a stable configuration. Finally, the workspace of the mechanism is approximated through surface fitting, and three inverse kinematics functions are defined using artificial neural networks, sequential quadratic programming and a genetic algorithm. The example presented uses six quadruplex modules, but the floor and ceiling functions applied make it valid for any cylindrical tensegrity stacking.

Keywords Form-finding · Tensegrity · Deployable · Inverse kinematics · Floor and ceiling

Supplementary Information The online version contains supplementary material available at https://doi.org/10.1007/s11012-024-01880-5.

V. Paiva · L. Silva-Teixeira · P. Kurka
Faculdade de Engenharia Mecânica, Universidade Estadual de Campinas, Rua Mendeleyev, 200, Campinas, SP 13083-860, Brazil

V. Paiva (✉)
Insper, Instituto de Ensino e Pesquisa, Rua Quatá, 300, São Paulo, SP 04546-042, Brazil
e-mail: victorasmp@insper.edu.br

J. Izuka · E. Okabe
Faculdade de Ciências Aplicadas, Universidade Estadual de Campinas, Rua Pedro Zaccaria, 1300, Campinas, SP 13484-350, Brazil

1 Introduction

Deployable structures and mechanisms, such as tensegrity and origami systems that transition from a compact state to a larger configuration, hold significant value in various engineering applications. Tensegrity structures consist of rigid elements connected by cables and rely on this network to maintain stability without external forces [1]. When properly optimized, tensegrity systems are lightweight, offer controllable shape [2] and stiffness [3], and can be integrated with origami [4]. These properties provide deployment capabilities and have driven developments in several scientific fields, such as biology [5, 6], architecture [7, 8], robotics [9], civil construction [10, 11] and material science [12]. By extension, multidisciplinary works also apply tensegrity systems [13]. This work focuses on the shape-shifting

Published online: 27 September 2024

characteristic of tensegrity structures, which is calculated through a form-finding technique, and its objective is to design a deployable tower capable of bowing.

Tensegrity robots can be organized into four main categories [14], referencing their shape: prismatic [15], spherical (with straight [16] or curved [17, 18] members), humanoid [19] and bio-inspired [20]. The mechanism studied in this paper mostly fits in the prismatic category because it stacks tensegrity prisms to form an arm.

Shape transformations can be calculated using form-finding methods, which are divided into two main categories: statical and kinematical [21] (or geometrical and topological [22]). Statical methods seek equilibrium configurations that meet specific requirements, allowing the structure to achieve a state of prestress. The force density method [23] is a popular example within the statical category. Raj and Guest [24] suggested a methodology that leverages symmetry to reduce the computational effort. Zhang et. al. [25] proposed a form-finding procedure based on the stiffness matrix (SMFF). Koohestani [26] presented a technique that determines the force densities by minimizing an objective function that generates the desired rank on the force density matrix, where the optimization is performed by a genetic algorithm. Additionally, an analytical approach [27] and an alternative involving nonlinear programming and LU-decomposition of the force density matrix [28] have been presented.

Kinematical methods usually fix the lengths of the bars and minimize the lengths of the cables or vice versa. One branch of this approach is to transform the form-finding of a tensegrity structure into a constrained minimization problem [29] that can be solved by nonlinear programming [30]. But nonlinear programming may not be suitable when there is a large solution space, therefore some researchers prefer a stochastic technique. A binary coded genetic algorithm was used in [31] to find the shape of non-regular tensegrities. Also, a Monte Carlo form-finding method was presented in [32] and demonstrated on numerous tensegrity configurations. The dynamic relaxation method is another significant branch within the kinematic category of form-finding methods. Starting from an initial guess, the member deformations are calculated and transformed into nodal forces using fictitious stiffness. Additionally, a fictitious mass is assigned to the nodes to determine their instantaneous accelerations, and the node equations of motion are solved using finite difference analysis [33]. Along with a damping factor, the parameters of the dynamic relaxation method can be optimized to improve efficiency [34].

The main purpose of this work is to develop a general kinematic study, from deployment and form-finding to inverse kinematics, of tensegrity towers formed by cylindrical prisms. Additionally, since there are not so many form-finding examples in the literature [35], this work aims to extend the collection of documented examples by applying the general methodology to a six quadruplex tower (see Fig. 1 and the video included as a supplementary file). These results contribute to an improved understanding of the paper and assist the community to build upon. A set of procedures is developed to produce the expansion of a transportable packed system into a tensegrity tower and afterward into an arched arm. The lengths of the cables are shortened to deploy the mechanism from the compact configuration into the high aspect ratio tower. Once fully deployed, cable lengths are varied to create irregular modules and assign a manipulator movement to the tower. The modules do not remain regular, therefore form-finding methods that assume symmetry cannot be used in this second part. Bars and base cables do not change their lengths, therefore force density methods may not be the best option.

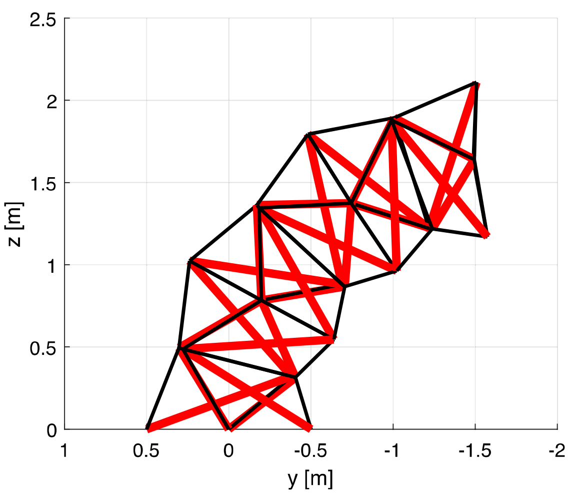

Fig. 1 Deployable tensegrity arm example composed of six quadruplex modules. Red and black lines indicate bars and cables, respectively

Since there is a small number of elements in each module, the nonlinear programming approach is advantageous. Additionally, floor and ceiling functions are applied to generalize the method's formulation for any assembly of cylindrical tensegrities [36]. The dynamic relaxation approach also meets these requirements and is compared to the method developed in this study.

The form-finding procedure determines the node coordinates from a given set of cable lengths. However, most practical applications have a target configuration to reach and require, in real-time, a set of cable lengths as an input. Therefore, an accurate and efficient inverse kinematics function is needed. In this paper, the workspace of the mechanism is approximated by a surface fit from discrete form-finding data. That data is also used as training information for a multilayer perceptron neural network to convert node coordinates in length cables. In the six quadruplex prisms example, the outputs of the inverse kinematics function are compared to four target positions.

The community has applied artificial intelligence to solve form-finding problems in tensegrity, reticulated [37] and origami [38] systems. A deep neural network can be trained using force densities obtained from a differential evolution algorithm [35] and applied to form-finding. The dynamic relaxation method can be combined with feed-forward neural networks [39] or noise-tolerant zeroing neural networks [40] to improve model accuracy and better support active controllers. In this work, inverse kinematics functions based on neural networks, genetic algorithm and sequential quadratic programming are proposed and compared.

2 Expansion of a packed system into a tower

Building a tensegrity system with variable strut lengths is possible [41], but substantially complex. However, the lengths of the cables can be changed by attaching one of their ends to a spool [42]. Still, having too many variable cables increase the overall weight of the structure due to the addition of actuators [43]. In this study, bar lengths b are fixed, and the only variable length cables are those connecting the top and bottom bases of each module. These cables are addressed as cross cables v to follow the pattern established by the community. Bottom nodes are fixed as in [44]. The twist angle (α) of tensegrity prisms can be counterclockwise (Fig. 2a) or clockwise (Fig. 2b), this characteristic has to be defined in advance and cannot be changed without rebuilding the prism. The rotations can also be named right and left-handed [45] referring to clock and counterclockwise, respectively. The mechanism shown in

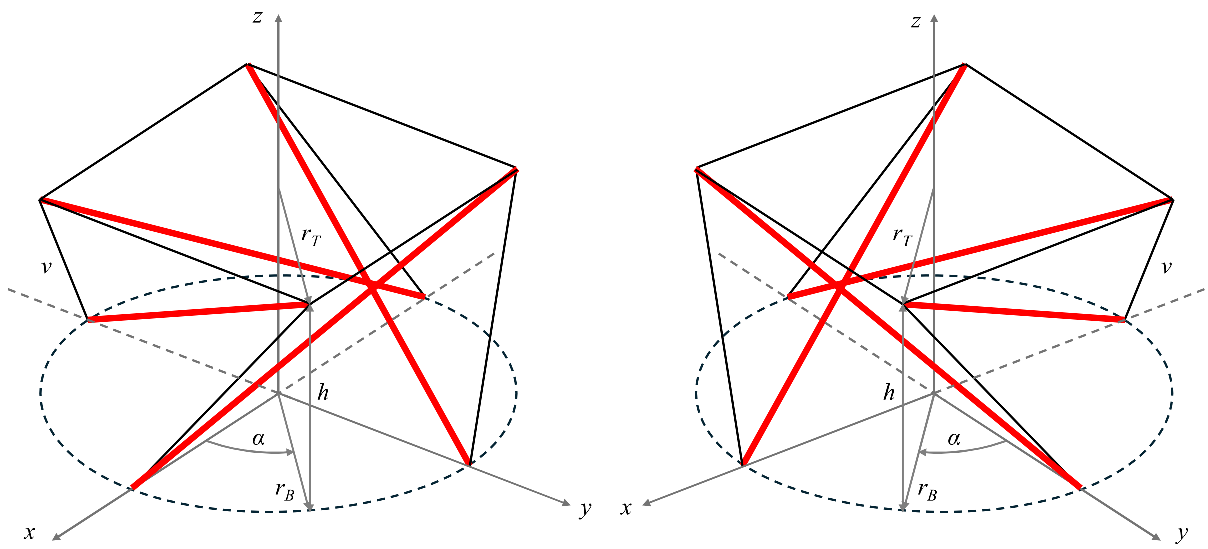

(a) Counterclockwise.

(b) Clockwise.

Fig. 2 Counterclockwise and clockwise examples of 12-struts regular modules this study uses alternate rotation modules to provide a straight bending.

In the expansion stage, all cross cables keep the same length $v_1 = v_2 = ... = v_t = v$. The coordinates of the bottom $\mathbf{N_B}$ and top nodes $\mathbf{N_T}$ of a regular counterclockwise tensegrity prism with t struts can be defined by equations 1 and 2 [36].

$$\mathbf{N_B} = \left[\mathbf{n_1}\ \mathbf{n_2}\ \dots\ \mathbf{n_t}\right] \tag{1}$$

$$\mathbf{N_T} = \left[\mathbf{n_{t+1}}\ \mathbf{n_{t+2}}\ \dots\ \mathbf{n_{2t}}\right] \tag{2}$$

Where h is the height of the prism, r_T and r_B are the top and bottom bases radii, respectively, and $\mathbf{n_i}$ (equation 3) defines the node coordinates of the i^{th} node.

$$\begin{cases} \mathbf{n_i} = \begin{Bmatrix} x_i \\ y_i \\ z_i \end{Bmatrix} = \begin{Bmatrix} r_B cos(\frac{i2\pi}{t}) \\ r_B sin(\frac{i2\pi}{t}) \\ 0 \end{Bmatrix} ||\text{if } \mathbf{n_i} \in \mathbf{N_B}|| \\ \mathbf{n_i} = \begin{Bmatrix} x_i \\ y_i \\ z_i \end{Bmatrix} = \begin{Bmatrix} r_T cos(\frac{i2\pi}{t} + \alpha) \\ r_T sin(\frac{i2\pi}{t} + \alpha) \\ h \end{Bmatrix} ||\text{if } \mathbf{n_i} \in \mathbf{N_T}|| \end{cases} \tag{3}$$

The global nodes matrix is formed by $\mathbf{N} = [\mathbf{N_B}, \mathbf{N_T}]$. The length of a bar b can be evaluated from the distance between nodes $\mathbf{n_{\lceil t/2 \rceil}}$ and $\mathbf{n_{2t}}$ in the clockwise module [36], where the prism height h can be defined (equation 4). Also, v is the distance from node $\mathbf{n_{\lceil t/2 \rceil}}$ to node $\mathbf{n_{t+1}}$ (equation 5).

$$b^2 = ||\mathbf{n_{\lceil t/2 \rceil}} - \mathbf{n_{2t}}||^2 \longrightarrow h^2 = b^2 - (x_{\lceil t/2 \rceil} - x_{2t})^2 - (y_{\lceil t/2 \rceil} - y_{2t})^2 \tag{4}$$

$$v^2 = ||\mathbf{n_{\lceil t/2 \rceil}} - \mathbf{n_{t+1}}||^2 \longrightarrow v^2 = h^2 + (x_{\lceil t/2 \rceil} - x_{t+1})^2 + (y_{\lceil t/2 \rceil} - y_{t+1})^2 \tag{5}$$

These equations provide the length of the cross cables v given the twist angle α. Considering the twist angle α range from 0 to $\frac{\pi}{2} - \frac{\pi}{t}$ (stable α for a tensegrity prism [46]), the expansion of a module from a flat configuration to its maximum height can be calculated. Also, a counterclockwise module can be attached bar to bar on top, generating a class two tensegrity system. These alternate rotation pairs may be repeatedly combined to obtain a tensegrity mechanism that can be deployed from a flat configuration.

Equations 4 and 5 are valid for regular counterclockwise tensegrity modules with four struts or more. The three struts module is not availed in this work because it locks [47] before reaching a flat configuration.

3 Form-finding

All modules in section 2 are regular because $v_1 = v_2 = ... = v_t = v$, which generates a straight expansion across stacked prisms [48]. However, irregular modules are necessary to induce a bowing movement, therefore cross cables are shortened or extended independently in this section.

To find the form of a module, v_1 to v_{t-1} remain fixed and the algorithm finds the minimum length of v_t. The solution can be separated into two smaller tasks:

1. Finding the final shape for a given set of cross cables v_1 to v_t, assuming the structure is possible.
2. Given v_1 to v_{t-1}, find the minimum v_t that generates a viable structure.

The first task can be transformed into a system of nonlinear equations, by geometrical relations, and solved by Newton–Raphson. Other numerical methods could be applied instead, but Newton–Raphson is simple to implement, provides relatively fast convergence and its main drawbacks are conveniently addressed: the derivatives are not complex and a reasonable initial guess can always be determined from the lower base coordinates.

The second task is an optimization problem that can be solved by nonlinear programming. The node coordinates of the bottom base are known for the ground module (equation 1) and the method calculates its top nodes coordinates.

3.1 Finding the final shape from v_1 to v_t

The bar (equation 6), top cables (equation 7) and cross cables (equation 8) incidences of a clockwise tensegrity prism are defined using floor and ceiling functions (for example, $\lceil 1.8 \rceil = 2$ and $\lfloor 1.8 \rfloor = 1$) [36]. For counterclockwise modules, the top base cable incidences remain the same, but bar and cross cable incidences are shown in equations 9 and 10, respectively.

$$\mathbf{I_B} = \begin{bmatrix} \mathbf{I_{B1}} \\ \mathbf{I_{B2}} \\ \vdots \\ \mathbf{I_{B\lfloor t/2 \rfloor}} \\ \mathbf{I_{B\lfloor t/2 \rfloor+1}} \\ \mathbf{I_{B\lfloor t/2 \rfloor+2}} \\ \vdots \\ \mathbf{I_{Bt}} \end{bmatrix} = \begin{bmatrix} t+1 & \lceil t/2 \rceil + 1 \\ t+2 & \lceil t/2 \rceil + 2 \\ \vdots & \\ \lfloor t/2 \rfloor + t & t \\ \lfloor t/2 \rfloor + t + 1 & 1 \\ \lfloor t/2 \rfloor + t + 2 & 2 \\ \vdots & \\ 2t & \lceil t/2 \rceil \end{bmatrix} \tag{6}$$

$$\mathbf{I_{TC}} = \begin{bmatrix} \mathbf{I_{TC1}} \\ \mathbf{I_{TC2}} \\ \vdots \\ \mathbf{I_{TCt-1}} \\ \mathbf{I_{TCt}} \end{bmatrix} = \begin{bmatrix} t+1 & t+2 \\ t+2 & t+3 \\ \vdots & \\ 2t-1 & 2t \\ 2t & t+1 \end{bmatrix} \tag{7}$$

$$\mathbf{I_{VC}} = \begin{bmatrix} \mathbf{I_{VC1}} \\ \mathbf{I_{VC2}} \\ \vdots \\ \mathbf{I_{VC\lfloor t/2 \rfloor+1}} \\ \mathbf{I_{VC\lfloor t/2 \rfloor+2}} \\ \mathbf{I_{VC\lfloor t/2 \rfloor+3}} \\ \vdots \\ \mathbf{I_{VCt}} \end{bmatrix} = \begin{bmatrix} \lceil t/2 \rceil & t+1 \\ \lceil t/2 \rceil + 1 & t+2 \\ \vdots & \\ t & \lfloor t/2 \rfloor + t + 1 \\ 1 & \lfloor t/2 \rfloor + t + 2 \\ 2 & \lfloor t/2 \rfloor + t + 3 \\ \vdots & \\ \lceil t/2 \rceil - 1 & 2t \end{bmatrix} \tag{8}$$

$$\mathbf{I_B} = \begin{bmatrix} \mathbf{I_{B1}} \\ \mathbf{I_{B2}} \\ \vdots \\ \mathbf{I_{B\lceil t/2 \rceil}} \\ \mathbf{I_{B\lceil t/2 \rceil+1}} \\ \mathbf{I_{B\lceil t/2 \rceil+2}} \\ \vdots \\ \mathbf{I_{Bt}} \end{bmatrix} = \begin{bmatrix} t+1 & \lfloor t/2 \rfloor + 1 \\ t+2 & \lfloor t/2 \rfloor + 2 \\ \vdots & \\ \lceil t/2 \rceil + t & t \\ \lceil t/2 \rceil + t + 1 & 1 \\ \lceil t/2 \rceil + t + 2 & 2 \\ \vdots & \\ 2t & \lfloor t/2 \rfloor \end{bmatrix} \tag{9}$$

$$\mathbf{I_{VC}} = \begin{bmatrix} \mathbf{I_{VC1}} \\ \mathbf{I_{VC2}} \\ \vdots \\ \mathbf{I_{VC\lceil t/2 \rceil-1}} \\ \mathbf{I_{VC\lceil t/2 \rceil}} \\ \mathbf{I_{VC\lceil t/2 \rceil+1}} \\ \vdots \\ \mathbf{I_{VCt}} \end{bmatrix} = \begin{bmatrix} \lfloor t/2 \rfloor + 2 & t+1 \\ \lfloor t/2 \rfloor + 3 & t+2 \\ \vdots & \\ t & \lceil t/2 \rceil + t - 1 \\ 1 & \lceil t/2 \rceil + t \\ 2 & \lceil t/2 \rceil + t + 1 \\ \vdots & \\ \lfloor t/2 \rfloor + 1 & 2t \end{bmatrix} \tag{10}$$

In a clockwise tensegrity prism, the distances from node $\mathbf{n_{\lceil t/2 \rceil+1}}$ to $\mathbf{n_{t+1}}$, $\mathbf{n_{\lceil t/2 \rceil+2}}$ to $\mathbf{n_t}$... $\mathbf{n_{t-\lceil t/2 \rceil}}$ to $\mathbf{n_{\lfloor t/2 \rfloor+t}}$ and $\mathbf{n_1}$ to $\mathbf{n_{\lfloor t/2 \rfloor+t+1}}$, $\mathbf{n_2}$ to $\mathbf{n_{\lfloor t/2 \rfloor+t+2}}$... $\mathbf{n_{\lceil t/2 \rceil}}$ to $\mathbf{n_{2t}}$ are equal to the length of a bar b. These relations are represented by a set of functions f_1 to f_t (equation 11).

$$\begin{aligned} f_1 &= \|\mathbf{n_{\lceil t/2 \rceil+1}} - \mathbf{n_{t+1}}\|^2 - b^2 \\ f_2 &= \|\mathbf{n_{\lceil t/2 \rceil+2}} - \mathbf{n_{t+2}}\|^2 - b^2 \\ &\vdots \\ f_{\lfloor t/2 \rfloor} &= \|\mathbf{n_t} - \mathbf{n_{\lfloor t/2 \rfloor+t}}\|^2 - b^2 \\ f_{\lfloor t/2 \rfloor+1} &= \|\mathbf{n_1} - \mathbf{n_{\lfloor t/2 \rfloor+t+1}}\|^2 - b^2 \\ f_{\lfloor t/2 \rfloor+2} &= \|\mathbf{n_2} - \mathbf{n_{\lfloor t/2 \rfloor+t+2}}\|^2 - b^2 \\ &\vdots \\ f_t &= \|\mathbf{n_{\lceil t/2 \rceil}} - \mathbf{n_{2t}}\|^2 - b^2 \end{aligned} \tag{11}$$

Using the base cables constant length l (equation 12), analogous relations f_{t+1} to f_{2t} can be stated to the base cables on top (equation 13) and f_{2t+1} to f_{3t} to the cross cables (equation 14).

$$l = r\sqrt{2\left(1 - cos\left(\frac{2\pi}{t}\right)\right)} \tag{12}$$

$$\begin{aligned} f_{t+1} &= \|\mathbf{n_{t+1}} - \mathbf{n_{t+2}}\|^2 - l^2 \\ f_{t+2} &= \|\mathbf{n_{t+2}} - \mathbf{n_{t+3}}\|^2 - l^2 \\ &\vdots \\ f_{2t-1} &= \|\mathbf{n_{2t-1}} - \mathbf{n_{2t}}\|^2 - l^2 \\ f_{2t} &= \|\mathbf{n_{2t}} - \mathbf{n_{t+1}}\|^2 - l^2 \end{aligned} \tag{13}$$

$$\begin{aligned} f_{2t+1} &= \|\mathbf{n_{\lceil t/2 \rceil}} - \mathbf{n_{t+1}}\|^2 - v_1^2 \\ f_{2t+2} &= \|\mathbf{n_{\lceil t/2 \rceil+1}} - \mathbf{n_{t+2}}\|^2 - v_2^2 \\ &\vdots \\ f_{2t+\lfloor t/2 \rfloor+1} &= \|\mathbf{n_t} - \mathbf{n_{\lfloor t/2 \rfloor+t+1}}\|^2 - v_{\lfloor t/2 \rfloor+1}^2 \\ f_{2t+\lfloor t/2 \rfloor+2} &= \|\mathbf{n_1} - \mathbf{n_{\lfloor t/2 \rfloor+t+2}}\|^2 - v_{2t+\lfloor t/2 \rfloor+2}^2 \\ f_{2t+\lfloor t/2 \rfloor+3} &= \|\mathbf{n_2} - \mathbf{n_{\lfloor t/2 \rfloor+t+3}}\|^2 - v_{\lfloor t/2 \rfloor+3}^2 \\ &\vdots \\ f_{3t} &= \|\mathbf{n_{\lceil t/2 \rceil-1}} - \mathbf{n_{2t}}\|^2 - v_t^2 \end{aligned} \tag{14}$$

The set of relations in a counterclockwise prism are analogous (equations 15, 16 and 17).

$$
\begin{aligned}
f_1 &= \|\mathbf{n}_{\lfloor t/2 \rfloor + 1} - \mathbf{n}_{t+1}\|^2 - b^2 \\
f_2 &= \|\mathbf{n}_{\lfloor t/2 \rfloor + 2} - \mathbf{n}_{t+2}\|^2 - b^2 \\
&\vdots \\
f_{\lceil t/2 \rceil} &= \|\mathbf{n}_{t} - \mathbf{n}_{\lceil t/2 \rceil + t}\|^2 - b^2 \\
f_{\lceil t/2 \rceil + 1} &= \|\mathbf{n}_{1} - \mathbf{n}_{\lceil t/2 \rceil + t + 1}\|^2 - b^2 \\
f_{\lceil t/2 \rceil + 2} &= \|\mathbf{n}_{2} - \mathbf{n}_{\lceil t/2 \rceil + t + 2}\|^2 - b^2 \\
&\vdots \\
f_t &= \|\mathbf{n}_{\lfloor t/2 \rfloor} - \mathbf{n}_{2t}\|^2 - b^2
\end{aligned}
\tag{15}
$$

$$
\begin{aligned}
f_{t+1} &= \|\mathbf{n}_{t+1} - \mathbf{n}_{t+2}\|^2 - l^2 \\
f_{t+2} &= \|\mathbf{n}_{t+2} - \mathbf{n}_{t+3}\|^2 - l^2 \\
&\vdots \\
f_{2t-1} &= \|\mathbf{n}_{2t-1} - \mathbf{n}_{2t}\|^2 - l^2 \\
f_{2t} &= \|\mathbf{n}_{2t} - \mathbf{n}_{t+1}\|^2 - l^2
\end{aligned}
\tag{16}
$$

$$
\begin{aligned}
f_{2t+1} &= \|\mathbf{n}_{\lfloor t/2 \rfloor + 2} - \mathbf{n}_{t+1}\|^2 - v_t^2 \\
f_{2t+2} &= \|\mathbf{n}_{\lfloor t/2 \rfloor + 3} - \mathbf{n}_{t+2}\|^2 - v_1^2 \\
&\vdots \\
f_{2t+\lceil t/2 \rceil - 1} &= \|\mathbf{n}_{t} - \mathbf{n}_{\lceil t/2 \rceil + t - 1}\|^2 - v^2_{2t+\lceil t/2 \rceil - 2} \\
f_{2t+\lceil t/2 \rceil} &= \|\mathbf{n}_{1} - \mathbf{n}_{\lceil t/2 \rceil + t}\|^2 - v^2_{\lceil t/2 \rceil - 1} \\
f_{2t+\lceil t/2 \rceil + 1} &= \|\mathbf{n}_{2} - \mathbf{n}_{\lceil t/2 \rceil + t + 1}\|^2 - v^2_{\lceil t/2 \rceil} \\
&\vdots \\
f_{3t} &= \|\mathbf{n}_{\lfloor t/2 \rfloor + 1} - \mathbf{n}_{2t}\|^2 - v^2_{t-1}
\end{aligned}
\tag{17}
$$

To satisfy the nonlinear system of equations, f must be close enough to zero. A solution vector containing the unknown top node coordinates $\mathbf{x}$ is created. The Jacobian matrix $\mathbf{J}$ can be assembled with the derivatives of f relative to the unknowns. Under a maximum number of iterations it_{MAX}, a Newton–Raphson routine finds a solution to the system. The system is considered to be impossible if it_{MAX} is reached and a solution vector that satisfies the tolerance ϵ has not been found.

A solution vector $\mathbf{x}$ that solves the nonlinear system of equations may not stabilize the tensegrity. For a given set of constant v_1 to v_{t-1}, the tensegrity is stable if v_t cannot be shortened anymore. A long v_t solves the Newton–Raphson routine successfully, while a shorter than necessary v_t suggests an impossible structure and the Newton–Raphson method cannot find a solution. The form-finding routine (Fig. 3) suggested in this paper uses these conditions to find the minimum v_t that satisfies the Newton–Raphson method for a given set of v_1 to v_{t-1}.

This form-finding methodology can be verified by inputting $v_1 = ... = v_{t-1}$ to obtain $v_1 = ... = v_{t-1} = v_t$. Other length combinations lead to irregular modules, which are useful to assign an arch shape to the mechanism. By attaching alternate rotation modules, a class 2 tensegrity mechanism that is capable of bowing is obtained.

3.2 Relevant comments

Top base nodes may not be coplanar, which may compromise the final shape of the tower. This issue can be measured by the volume formed by $\mathbf{n}_{t+1}\mathbf{n}_{t+2}$, $\mathbf{n}_{t+1}\mathbf{n}_{2t}$ and all other top base vectors. Increments on cross cables should be applied to minimize the sum (equation 18) of these volumes.

$$
V = \sum_{i=t+3}^{2t-1} \|(\mathbf{n}_{t+1} - \mathbf{n}_{t+2}) \cdot ((\mathbf{n}_{t+1} - \mathbf{n}_{2t}) \times (\mathbf{n}_{t+1} - \mathbf{n}_{i}))\| \tag{18}
$$

Researchers occasionally avoid using a Newton–Raphson routine because an inconvenient initial guess may lead to inaccurate results. A reasonable guess for the top nodes can be found from the normal unitary vector $\mathbf{u_N}$ that defines the bottom base plane. The initial guess can be calculated by scaling $\mathbf{u_N}$ (equation 19) according to the bar length and adding it to the base nodes. For efficiency purposes, this initial guess strategy remains valid for other solvers, such as the Levenberg-Marquardt method.

$$
\mathbf{u_N} = \frac{(\mathbf{n}_{t+1} - \mathbf{n}_{t+2}) \times (\mathbf{n}_{t+1} - \mathbf{n}_{2t})}{\|(\mathbf{n}_{t+1} - \mathbf{n}_{t+2}) \times (\mathbf{n}_{t+1} - \mathbf{n}_{2t})\|} \tag{19}
$$

4 Inverse kinematics

The form-finding strategy takes a set of cable lengths (v_1 to v_t) as an input and returns its resultant node coordinates. A hypothetical camera or manipulator would be placed in the upper base node coordinates. Therefore, the mean coordinates of the upper base node coordinates $(x, y, z)_{ep}$ are addressed as the end-effector of the mechanism. A discrete definition of the end-effector workspace may be obtained from a large group of cable length sets. Also, a fifth order polynomial (equation 20) that best fits

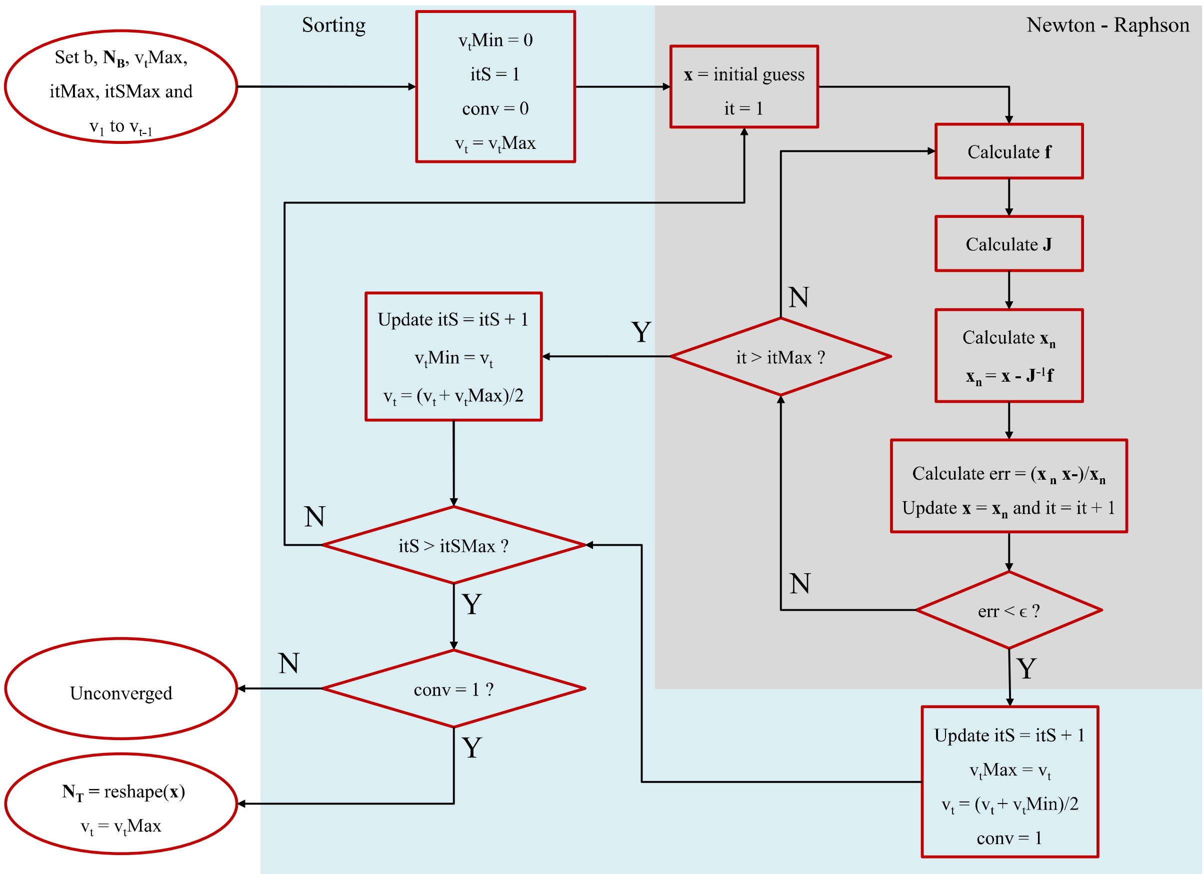

Fig. 3 Kinematical form-finding algorithm for tensegrity prisms

the discrete data can be approximated to represent a continuous shape of the workspace.

$$
\begin{aligned}
f(x,y) = & p_{00} + p_{10}x + p_{01}y + p_{20}x^2 + p_{11}xy \\
& + p_{02}y^2 + p_{30}x^3 + p_{21}x^2y \\
& + p_{12}xy^2 + p_{03}y^3 + p_{40}x^4 + p_{31}x^3y \\
& + p_{22}x^2y^2 + p_{13}xy^3 \\
& + p_{04}y^4 + p_{50}x^5 + 41x^4y + p_{32}x^3y^2 \\
& + p_{23}x^2y^3 + p_{14}xy^4 + p_{05}y^5
\end{aligned}
\tag{20}
$$

The inverse kinematics is necessary because most applications have a target position to place the end-effector and require the cable lengths information to supply the actuators. In this study, the inverse kinematics function converts a desired end-effector position $(x, y, z)_{ep}$ in a set of cable lengths (v_1 to v_{t-1}). The discrete workspace data is used as training information for an artificial neural network. A relatively simple multilayer perceptron network [49, 50] with ten hidden layers and five neurons layer size (Fig. 4) provides reliable results under the Bayesian

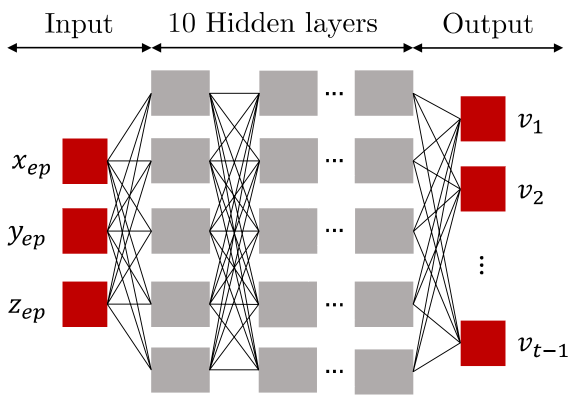

Fig. 4 Neural network diagram

regularization training algorithm. A data set with at least 2000 samples is recommended.

5 Six quadruplex case

5.1 Expansion of the six quadruplex case

The general methodology is applied to a class 2 tensegrity tower formed by six levels of four struts ($t = 4$) prisms. Also, the base radius is half of the bar length ($r = b/2$) to allow a fully flat configuration before expansion. In this study, the bar length is unitary 1 m. The nodes matrix $\mathbf{N}$ is defined in equation 21 as a function of the twist angle $0 \leq \alpha \leq \pi/4$ rad. The height h and the cross cable length v can be calculated by applying $t = 4$ in equations 4 and 5.

$$\mathbf{N} = \begin{bmatrix} 0 & -\frac{b}{2} & 0 & \frac{b}{2} & -\frac{b}{2}cos(\alpha) & -\frac{b}{2}cos(\alpha) & \frac{b}{2}cos(\alpha) & \frac{b}{2}cos(\alpha) \\ \frac{b}{2} & 0 & -\frac{b}{2} & 0 & \frac{b}{2}sin(\alpha) & -\frac{b}{2}sin(\alpha) & -\frac{b}{2}sin(\alpha) & \frac{b}{2}sin(\alpha) \\ 0 & 0 & 0 & 0 & h & h & h & h \end{bmatrix} \tag{21}$$

The process is reproduced in the counterclockwise module. Their bars are attached to generate a class two tensegrity tower that can be deployed from a flat configuration (Fig. 5). The height of the structure in the first position depends on the diameter of the bars, therefore a physical prototype would not be fully flat as in this simulation. Analogously, manufacturing imperfections could integrate irregularities in a fully expanded prototype [51].

5.2 Form-finding of the six quadruplex case

To assign a manipulator shape to the tower, the form-finding procedure is applied. The set of functions for the clockwise and counterclockwise modules are obtained by applying $t = 4$, $b = 1$, $l = b\sqrt{2}/2$ and $r = b/2$. The Jacobian matrix $\mathbf{J}$ for the clockwise (Table 4) and counterclockwise (Table 5) modules are calculated and supplied to the form-finding algorithm.

The form-finding routine calculates the minimum v_4 that satisfies the Newton–Raphson procedure given v_1, v_2 and v_3. As a form of validation, the input $v_1 = v_2 = v_3 = 0.541m$ returns $v_4 = 0.541m$ to build a regular prism. The node coordinates used as an initial guess for the Newton–Raphson method are found by summing the bottom base coordinates with the normal vector (22) that defines its plane.

$$\mathbf{u_N} = \frac{(\mathbf{n_5} - \mathbf{n_6}) \times (\mathbf{n_5} - \mathbf{n_8})}{\|(\mathbf{n_5} - \mathbf{n_6}) \times (\mathbf{n_5} - \mathbf{n_8})\|} \tag{22}$$

To generate a coplanar upper base, each v_1 and v_2 pair is associated with a v_3 whose v_4 provided by the routine minimizes the volume formed by the top nodes vectors (equation 23).

$$V = \|(\mathbf{n_5} - \mathbf{n_7}) \cdot ((\mathbf{n_5} - \mathbf{n_8}) \times (\mathbf{n_5} - \mathbf{n_6}))\| \tag{23}$$

Shorter v_1 and v_2 lead to longer v_3 and v_4. That generates an irregular module, which is useful to assign an arch format to the tower when combined with other prisms. Also, it is convenient to alternate clockwise and counterclockwise modules to avoid a spiral shape while keeping all modules under the same set of cross

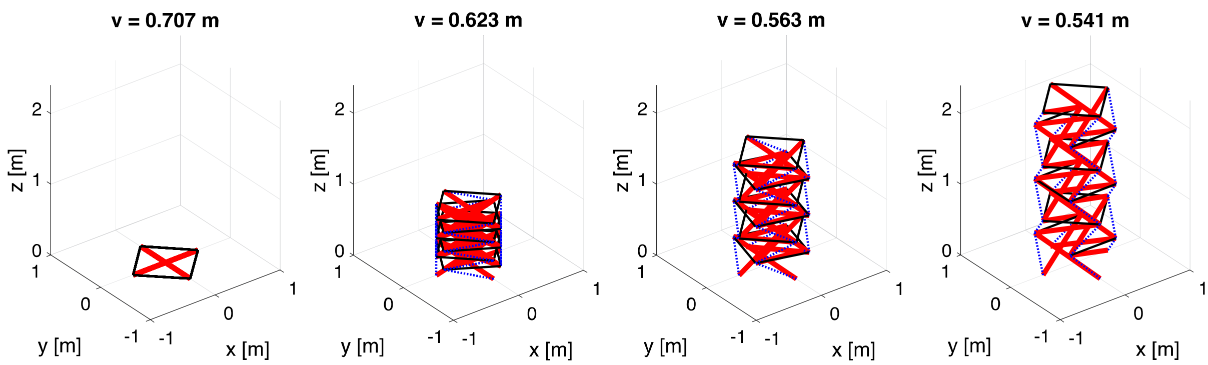

Fig. 5 Deployment of a class two tensegrity tower. Dotted blue lines indicate cables that have shortened compared to the previous stage

cable lengths. Each configuration presented in Fig. 6 is formed by combining prisms with identical v sets.

5.3 Comparison to other form-finding techniques

The dynamic relaxation method is a popular kinematic form-finding approach that has been extensively studied by the community. The traditional version [33] is implemented in this study, but it has been found to be less efficient under equal tolerance requirements (Table 1). This outcome is expected, as the dynamic relaxation method relies on finite difference evaluations of differential equations, which generally require more computational effort than solving a nonlinear system of equations. The mass and stiffness assigned to the mechanism elements are fictitious and can be further adjusted to improve performance, along with a damping factor [34]. However, the significant efficiency gap between this method and alternatives suggests that these enhancements may not justify using the dynamic relaxation algorithm for this purpose when efficiency is a priority.

In a single iteration, the Newton–Raphson method demonstrates significantly higher efficiency. This is expected because the Jacobian matrix is precomputed for this nonlinear system (Tables 4 and 5), while other methods require additional computational resources to obtain the equivalent information. However, for a high number of iterations, the built-in Levenberg-Marquardt function outperforms its alternatives. This advantage arises because the initial call to *fsolve* incurs additional overhead related to initialization and memory allocation, while subsequent calls can reuse some cached components, resulting in faster execution times.

Table 1 Performance comparison for a tolerance of 10^{-21} in square sum of member length error. The time elapsed measurements are obtained using MATLAB version 2022a running in a standard desktop computer (core i5-9400F 16GB RAM)

Iterations	Dynamic relaxation	Levenberg-Marquardt	Newton-Raphson
1	1.037 s	0.712 s	0.088 s
10	9.593 s	0.786 s	0.652 s
100	93.29 s	1.117 s	5.478 s
1000	931.7 s	4.052 s	53.67 s

5.4 Inverse kinematics of the six quadruplex case

A discrete definition of the end-effector workspace is obtained by 2555 sets of cross cable lengths. The fifth-order polynomial, whose coefficients are defined in Table 6, provides a continuous approximation ($R^2 = 0.74$) of that workspace.

The circle markers in Fig. 7 represent the discrete workspace obtained through form-finding from 2555 cable length sets. This form of presentation is qualitatively equivalent to the workspace shown in [52] of a tensegrity arm formed by x-shaped rigid bodies. The artificial neural network contains ten layers, five neurons layer size and is trained with the Bayesian regularization algorithm using 70% of the data for training, 15% for validation and 15% for testing. The time elapsed in the training session ranges from 30 s to 200 s, and from 4 to 12 h to generate the data set in a standard desktop computer (core i5-9400F 16GB RAM), both can vary due to the stochastic nature of the methods.

Four target positions $(x, y, z)_{tg}$ in the surface fit are indicated in Fig. 7 by cross markers. Their x coordinates are zero, y coordinates are $-0.5m$, $-1.0m$, $-1.5m$ and $-2m$, and z coordinates are estimated by the polynomial approximation of the workspace. Their respective

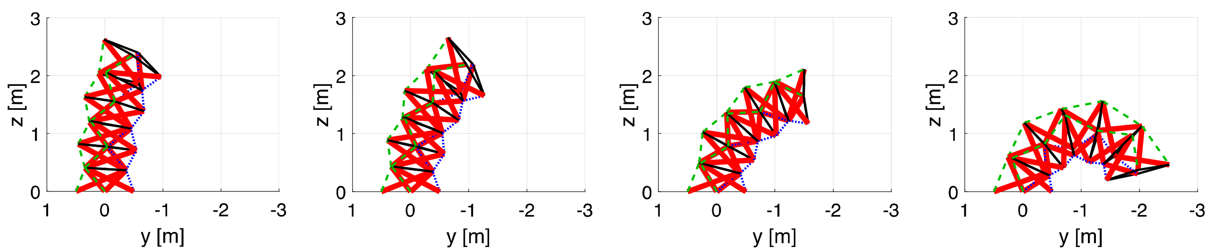

Fig. 6 Arching of a class two tensegrity tower. Dashed green lines indicate cables that have lengthened compared to the previous stage

Table 2 Sets of cross cable lengths obtained by the inverse kinematics function based on neural networks and their respective v_4 found by the form-finding procedure

Target	$(x, y, z)_{tg}[m]$	v_{1nn} [m]	v_{2nn} [m]	v_{3nn} [m]	v_{4ff} [m]	$(x, y, z)_{ep}$ [m]
1	(0, − 0.5, 2.341)	0.5486	0.5277	0.5362	0.5537	(− 0.001, − 0.500, 2.340)
2	(0, − .0, 2.182)	0.5572	0.5130	0.5300	0.5719	(0.004, − 0.985, 2.171)
3	(0, − 1.5, 1.641)	0.5726	0.4862	0.5205	0.6184	(− 0.002, − 1.516, 1.638)
4	(0, − 2.0, 0.329)	0.6101	0.4500	0.5135	0.6924	(− 0.013, − 1.974, 0.335)

Table 3 Relative error of the end-effector coordinates obtained by the model from inverse kinematics functions based on neural network, SQP and genetic algorithms

Target	Neural network %	SQP %	Genetic algorithm %
1	0.0470	17.241	0.0389
2	0.7981	17.105	4.7794
3	0.7274	38.244	0.2917
4	1.4828	28.562	1.4430

$(v_1, v_2, v_3)_{nn}$ sets calculated by the trained neural network are presented in Table 2. These cross cable sets are applied in the form-finding function (configurations in Fig. 6) to obtain v_{4ff} and the actual end-effector positions $(x, y, z)_{ep}$ (plus markers in Fig. 7) and remained within a maximum relative error of 1.48% relative to the target length (Table 3).

As an alternative approach, optimization techniques can be employed to minimize the squared error between the target and calculated end-effector coordinates. In this

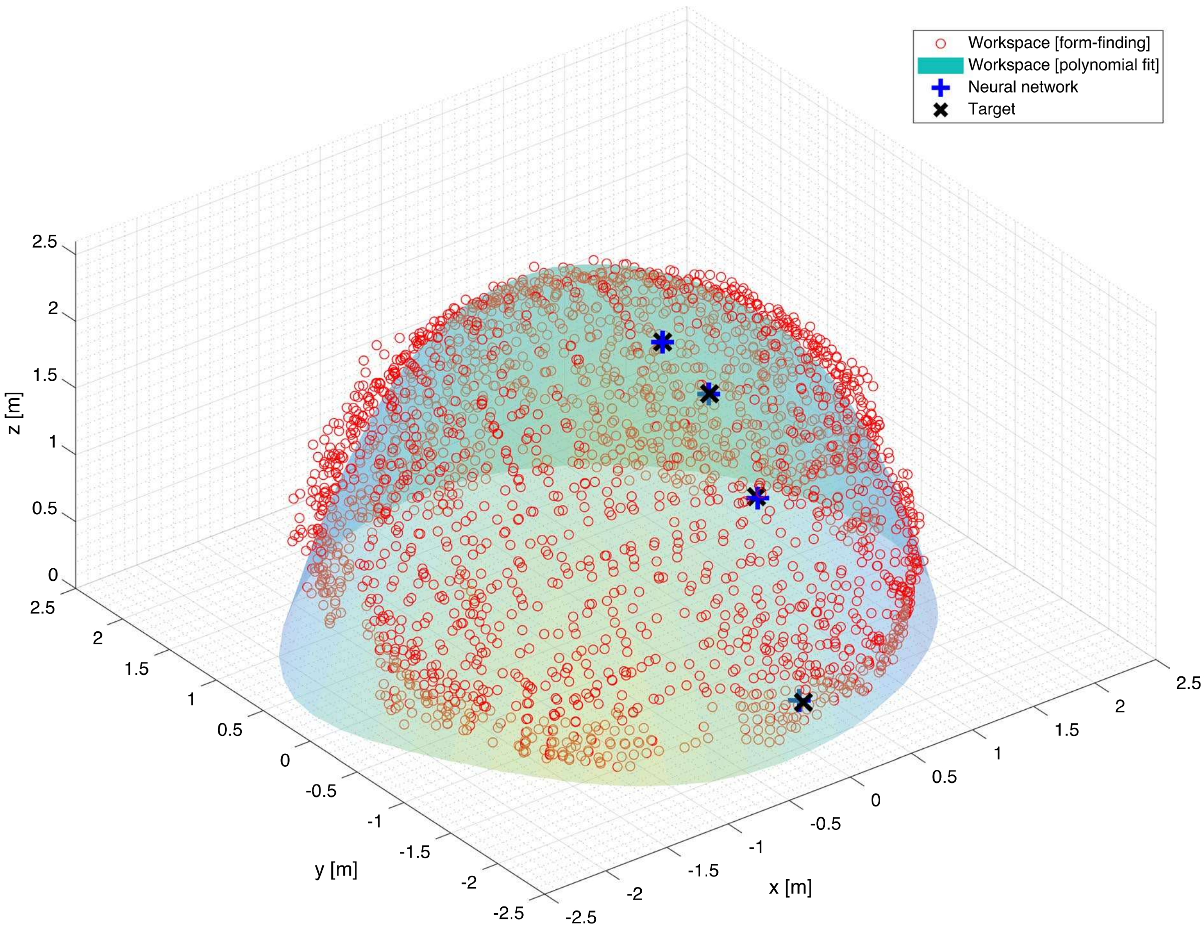

Fig. 7 Discrete and continuous definitions of the workspace, target positions and outputs from the inverse kinematics function

study, we utilize the Sequential Quadratic Programming (SQP) [53] method and the Genetic Algorithm (GA) [54] to solve the inverse kinematics problem. The relative errors produced by their respective inverse kinematics solutions are presented in Table 3. Both SQP and GA routines are performed in MATLAB version 2022a with default parameters, except for the 100 population size in GA and $0.541m$ cable length as initial guess for the SQP method. The lower and upper bounds for cable lengths are set as $0.4m$ and $0.7m$.

The error between the target and calculated coordinates is highly nonlinear and generates numerous local minimum points. This characteristic is adverse to the performance of the SQP method, which may converge to a local minimum that is closer to the initial guess. Combinations of initial guesses have been employed, but no significant gain in accuracy has been observed in this particular example. On the other hand, stochastic methods make them usually more efficient in escaping local optimum points. The GA presents satisfactory relative errors for the four targets, which suggests it could be reliably employed as an inverse kinematics function for this tensegrity arm example. The processing time is the main drawback of these optimization techniques in this context. Therefore, for applications that require a real-time computation, a previously trained neural network is recommended to perform the inverse kinematics over SQP or GA optimization methods.

6 Conclusions

The methodologies for deployment, form-finding, and inverse kinematics of a tensegrity tower mechanism are presented. The tower is formed by attaching cylindrical modules base to base to generate a class 2 tensegrity. The deployment of the structure from a flat configuration into a high aspect ratio mast is detailed. A kinematical form-finding method to determine the final form of the structure from a given set of cross cable lengths is developed. The procedure converts form-finding into an optimization problem and solves it by nonlinear programming. The details of the routine are presented. A strategy that shifts the shape of the tower into an arch is shown, and a discrete definition of the mechanism workspace is calculated through form-finding. A fifth-order polynomial approximation is used to define a continuous surface that fits the discrete workspace. The discrete workspace and its cable length sets are also used as training data for an artificial neural network with five hidden layers and five neurons layer size. The suggested methods are functional for any number of cylindrical tensegrity modules due to the floor and ceiling functions, six quadruplex are used as an example. However, poorly selected member lengths may lock the structure before reaching a fully flat configuration or require more modules to produce a tower that is capable of arching.

The inverse kinematics function generated by the trained neural network model approximates four target positions with a maximum relative error of 1.48% in a very low computing time. The inverse kinematics function based on the genetic algorithm presents a maximum relative error of 4.78% without spending computational resources on training sessions and data sets generation. However, each evaluation requires high computational effort, leading to a very long computing time. Therefore, neural networks are recommended to build the inverse kinematics model employed real-time applications that rely on fast responses, such as control.

Compared to other form-finding methods, this kinematic approach requires more input data, such as strut lengths and ground base coordinates. However, many applications benefit from having constant member lengths and do not permit variable base coordinates. Additionally, the methodology proposed in this study has shown greater efficiency than the traditional dynamic relaxation algorithm when applied to the quadruplex example. Future work will involve analysing the possibility of creating an S shape by combining modules with different cross cable sets, constructing the mechanism and conducting experiments to further validate its effectiveness as a deployable mechanism.

Funding No funding was received to assist with the preparation of this manuscript

Declarations

Conflict of interest The authors have no Conflict of interest to declare.

Appendix A Workspace coefficients and Jacobian matrices

This appendix contains the Jacobian matrices (Tables 4 and 5) of a clockwise and counterclockwise quadruplex modules and the coefficients of the mechanism workspace surface approximated by a fifth order polynomial (Table 6).

Table 4 Jacobian matrix for the clockwise tensegrity prism

Eq.	$\frac{\partial}{\partial x_5}$	$\frac{\partial}{\partial y_5}$	$\frac{\partial}{\partial z_5}$	$\frac{\partial}{\partial x_6}$	$\frac{\partial}{\partial y_6}$	$\frac{\partial}{\partial z_6}$
f_1	$2(x_5 - x_3)$	$2(y_5 - y_3)$	$2(z_5 - z_3)$	0	0	0
f_2	0	0	0	$2(x_6 - x_4)$	$2(y_6 - y_4)$	$2(y_6 - y_4)$
f_3	0	0	0	0	0	0
f_4	0	0	0	0	0	0
f_5	$2(x_5 - x_6)$	$2(y_5 - y_6)$	$2(z_5 - z_6)$	$2(x_6 - x_5)$	$2(y_6 - y_5)$	$2(z_6 - z_5)$
f_6	0	0	0	$2(x_6 - x_7)$	$2(y_6 - y_7)$	$2(z_6 - z_7)$
f_7	0	0	0	0	0	0
f_8	$2(x_5 - x_8)$	$2(y_5 - y_8)$	$2(z_5 - z_8)$	0	0	0
f_9	$2(x_5 - x_2)$	$2(y_5 - y_2)$	$2(z_5 - z_2)$	0	0	0
f_{10}	0	0	0	$2(x_6 - x_3)$	$2(y_6 - y_3)$	$2(z_6 - z_3)$
f_{11}	0	0	0	0	0	0
f_{12}	0	0	0	0	0	0
Eq.	$\frac{\partial}{\partial x_7}$	$\frac{\partial}{\partial y_7}$	$\frac{\partial}{\partial z_7}$	$\frac{\partial}{\partial x_8}$	$\frac{\partial}{\partial y_8}$	$\frac{\partial}{\partial z_8}$
f_1	0	0	0	0	0	0
f_2	0	0	0	0	0	0
f_3	$2(x_7 - x_1)$	$2(y_7 - y_1)$	$2(z_7 - z_1)$	0	0	0
f_4	0	0	0	$2(x_8 - x_2)$	$2(y_8 - y_2)$	$2(z_8 - z_2)$
f_5	0	0	0	0	0	0
f_6	$2(x_7 - x_6)$	$2(y_7 - y_6)$	$2(z_7 - z_6)$	0	0	0
f_7	$2(x_7 - x_8)$	$2(y_7 - y_8)$	$2(z_7 - z_8)$	$2(x_8 - x_7)$	$2(y_8 - y_7)$	$2(z_8 - z_7)$
f_8	0	0	0	$2(x_8 - x_5)$	$2(y_8 - y_5)$	$2(z_8 - z_5)$
f_9	0	0	0	0	0	0
f_{10}	0	0	0	0	0	0
f_{11}	$2(x_7 - x_4)$	$2(y_7 - y_4)$	$2(z_7 - z_4)$	0	0	0
f_{12}	0	0	0	$2(x_8 - x_1)$	$2(y_8 - y_1)$	$2(z_8 - z_1)$

Table 5 Jacobian matrix for the counterclockwise tensegrity prism

Eq.	$\frac{\partial}{\partial x_5}$	$\frac{\partial}{\partial y_5}$	$\frac{\partial}{\partial z_5}$	$\frac{\partial}{\partial x_6}$	$\frac{\partial}{\partial y_6}$	$\frac{\partial}{\partial z_6}$
f_1	$2(x_5 - x_3)$	$2(y_5 - y_3)$	$2(z_5 - z_3)$	0	0	0
f_2	0	0	0	$2(x_6 - x_4)$	$2(y_6 - y_4)$	$2(y_6 - y_4)$
f_3	0	0	0	0	0	0
f_4	0	0	0	0	0	0
f_5	$2(x_5 - x_6)$	$2(y_5 - y_6)$	$2(z_5 - z_6)$	$2(x_6 - x_5)$	$2(y_6 - y_5)$	$2(z_6 - z_5)$
f_6	0	0	0	$2(x_6 - x_7)$	$2(y_6 - y_7)$	$2(z_6 - z_7)$
f_7	0	0	0	0	0	0
f_8	$2(x_5 - x_8)$	$2(y_5 - y_8)$	$2(z_5 - z_8)$	0	0	0
f_9	$2(x_5 - x_4)$	$2(y_5 - y_4)$	$2(z_5 - z_4)$	0	0	0
f_{10}	0	0	0	$2(x_6 - x_1)$	$2(y_6 - y_1)$	$2(z_6 - z_1)$
f_{11}	0	0	0	0	0	0
f_{12}	0	0	0	0	0	0

Eq.	$\frac{\partial}{\partial x_7}$	$\frac{\partial}{\partial y_7}$	$\frac{\partial}{\partial z_7}$	$\frac{\partial}{\partial x_8}$	$\frac{\partial}{\partial y_8}$	$\frac{\partial}{\partial z_8}$
f_1	0	0	0	0	0	0
f_2	0	0	0	0	0	0
f_3	$2(x_7 - x_1)$	$2(y_7 - y_1)$	$2(z_7 - z_1)$	0	0	0
f_4	0	0	0	$2(x_8 - x_2)$	$2(y_8 - y_2)$	$2(z_8 - z_2)$
f_5	0	0	0	0	0	0
f_6	$2(x_7 - x_6)$	$2(y_7 - y_6)$	$2(z_7 - z_6)$	0	0	0
f_7	$2(x_7 - x_8)$	$2(y_7 - y_8)$	$2(z_7 - z_8)$	$2(x_8 - x_7)$	$2(y_8 - y_7)$	$2(z_8 - z_7)$
f_8	0	0	0	$2(x_8 - x_5)$	$2(y_8 - y_5)$	$2(z_8 - z_5)$
f_9	0	0	0	0	0	0
f_{10}	0	0	0	0	0	0
f_{11}	$2(x_7 - x_2)$	$2(y_7 - y_2)$	$2(z_7 - z_2)$	0	0	0
f_{12}	0	0	0	$2(x_8 - x_3)$	$2(y_8 - y_3)$	$2(z_8 - z_3)$

Table 6 Surface fit coefficients and 95% confidence bounds

Coefficient	Average value	Confidence bounds
p_{00}	2.35500	(2.28600, 2.42400)
p_{10}	− 0.05612	(− 0.17760, 0.06538)
p_{01}	− 0.03196	(− 0.15540, 0.09145)
p_{20}	− 0.23170	(− 0.30960, -0.15370)
p_{11}	0.01159	(− 0.07329, 0.09647)
p_{02}	− 0.08932	(− 0.16770, -0.01089)
p_{30}	0.06654	(− 0.03178, 0.16490)
p_{21}	0.09260	(− 0.03390, 0.21910)
p_{12}	0.04508	(− 0.08186, 0.17200)
p_{03}	0.01422	(− 0.08598, 0.11440)
p_{40}	− 0.06075	(− 0.07924, − 0.04225)
p_{31}	− 0.04199	(− 0.06814, − 0.01585)
p_{22}	− 0.19340	(− 0.22320, − 0.16360)
p_{13}	0.02814	(0.00281, 0.05347)
p_{04}	− 0.10140	(− 0.11970, − 0.08306)
p_{50}	− 0.01764	(− 0.03682, 0.00154)
p_{41}	− 0.01434	(− 0.04473, 0.01604)
p_{32}	− 0.01338	(− 0.05251, 0.02574)
p_{23}	− 0.02329	(− 0.06270, 0.01612)
p_{14}	− 0.01637	(− 0.04651, 0.01376)
p_{05}	− 0.00010	(− 0.01947, 0.01926)

References

1. Skelton RE, De Oliveira MC (2009) Tensegrity Systems, vol 1. Springer, New York
2. Su Y, Zhang J, Ohsaki M, Wu Y (2020) Topology optimization and shape design method for large-span tensegrity structures with reciprocal struts. Int J Sol Struct 206:9–22. https://doi.org/10.1016/j.ijsolstr.2020.09.002
3. Amendola A, Krushynska A, Daraio C, Pugno NM, Fraternali F (2018) Tuning frequency band gaps of tensegrity mass-spring chains with local and global prestress. Int J Sol Struct 155:47–56. https://doi.org/10.1016/j.ijsolstr.2018.07.002
4. Ma S, Chen M, Zhang H, Skelton RE (2023) Statics of integrated origami and tensegrity systems. Int J Sol Struct 279:112361. https://doi.org/10.1016/j.ijsolstr.2023.112361
5. Ingber DE (2003) Tensegrity i. cell structure and hierarchical systems biology. J Cell Sci 116(7):1157–1173. https://doi.org/10.1242/jcs.00359
6. Giverso C, Loy N, Lucci G, Preziosi L (2023) Cell orientation under stretch: a review of experimental findings and mathematical modelling. J Theor Biology. https://doi.org/10.1016/j.jtbi.2023.111564
7. Carpentieri G, Modano M, Fabbrocino F, Feo L, Fraternali F (2017) On the minimal mass reinforcement of masonry structures with arbitrary shapes. Meccanica 52:1561–1576. https://doi.org/10.1007/s11012-016-0493-0
8. Jáuregui VG (2020) Tensegrity structures and their application to architecture. Universidad de Cantabria, Cantabria
9. Kurka PR, Paiva VA, Silva-Teixeira LH, Ramos PG, Izuka JH (2024) A dynamical model for the control of a guyed tensegrity beam under large displacements. J Mech Robotics. https://doi.org/10.1115/1.4064259
10. Mirzaaghazadeh K, Abedi K, Shekastehband B (2021) An efficient self-stress design of tensegrity shell structures. Meccanica 56:147–168. https://doi.org/10.1007/s11012-020-01260-9
11. Fraternali F, Castro Motta J (2023) Mechanics of superelastic tensegrity braces for timber frames equipped with buckling-restrained devices. Int J Sol Struct 281:112414. https://doi.org/10.1016/j.ijsolstr.2023.112414
12. Yin X, Gao Z-Y, Zhang S, Zhang L-Y, Xu G-K (2020) Truncated regular octahedral tensegrity-based mechanical metamaterial with tunable and programmable poisson's ratio. Int J Mechanical Sci 167:105285. https://doi.org/10.1016/j.ijmecsci.2019.105285
13. Kim SY, Baines R, Booth J, Vasios N, Bertoldi K, Kramer-Bottiglio R (2019) Reconfigurable soft body trajectories using unidirectionally stretchable composite laminae. Nat commun 10(1):3464. https://doi.org/10.1038/s41467-019-11294-7
14. Liu Y, Bi Q, Yue X, Wu J, Yang B, Li Y (2022) A review on tensegrity structures-based robots. Mech Machine Theory 168:104571. https://doi.org/10.1016/j.mechmachtheory.2021.104571
15. Arsenault M, Gosselin CM (2009) Kinematic and static analysis of a 3-pups spatial tensegrity mechanism. Mech Machine Theory 44(1):162–179. https://doi.org/10.1016/j.mechmachtheory.2008.02.005
16. Agogino AK, SunSpiral V, Atkinson D (2018) Super ball bot-structures for planetary landing and exploration. Technical report, NASA
17. Schorr P, Li ERC, Kaufhold T, Hernández JAR, Zentner L, Zimmermann K, Böhm V (2021) Kinematic analysis of a rolling tensegrity structure with spatially curved members. Meccanica 56:953–961. https://doi.org/10.1007/s11012-020-01199-x
18. Jahn H, Böhm V, Zentner L (2024) Analysis of deformation in tensegrity structures with curved compressed members. Meccanica. https://doi.org/10.1007/s11012-024-01833-y
19. Lessard S, Castro D, Asper W, Chopra SD, Baltaxe-Admony LB, Teodorescu M, SunSpiral V, Agogino A (2016) A bio-inspired tensegrity manipulator with multi-dof, structurally compliant joints. In: 2016 IEEE/RSJ International conference on intelligent robots and systems (IROS), pp. 5515–5520. https://doi.org/10.1109/IROS.2016.7759811 . IEEE
20. Liu R, Yao Y-A (2019) A novel serial-parallel hybrid worm-like robot with multi-mode undulatory locomotion. Mech Machine Theory 137:404–431
21. Tibert A, Pellegrino S (2011) Review of form-finding methods for tensegrity structures. Int J Sp Struct 26(3):241–255. https://doi.org/10.1260/0266-3511.26.3.241
22. Liu K, Paulino GH (2019) Tensegrity topology optimization by force maximization on arbitrary ground

structures. Struct Multidiscip Optimization 59:2041–2062. https://doi.org/10.1007/s00158-018-2172-3
23. Zhang J, Ohsaki M (2006) Adaptive force density method for form-finding problem of tensegrity structures. Int J Sol Struct 43(18–19):5658–5673. https://doi.org/10.1016/j.ijsolstr.2005.10.011
24. Raj RP, Guest S (2006) Using symmetry for tensegrity form-finding. J Int Association Shell Spatial Struct 47(3):245–252
25. Zhang L-Y, Li Y, Cao Y-P, Feng X-Q (2014) Stiffness matrix based form-finding method of tensegrity structures. Eng Struct 58:36–48. https://doi.org/10.1016/j.engstruct.2013.10.014
26. Koohestani K (2012) Form-finding of tensegrity structures via genetic algorithm. Int J Sol Struct 49(5):739–747. https://doi.org/10.1016/j.ijsolstr.2011.11.015
27. Koohestani K (2017) On the analytical form-finding of tensegrities. Composite Struct 166:114–119. https://doi.org/10.1016/j.compstruct.2017.01.059
28. Koohestani K (2020) Innovative numerical form-finding of tensegrity structures. Int J Sol Struct 206:304–313. https://doi.org/10.1016/j.ijsolstr.2020.09.034
29. Pellegrino S (1986) Mechanics of kinematically indeterminate structures. PhD thesis, University of Cambridge
30. Ohsaki M, Zhang J (2015) Nonlinear programming approach to form-finding and folding analysis of tensegrity structures using fictitious material properties. Int J Sol Struct 69:1–10. https://doi.org/10.1016/j.ijsolstr.2015.06.020
31. Xu X, Luo Y (2010) Form-finding of nonregular tensegrities using a genetic algorithm. Mech Res Commun 37(1):85–91. https://doi.org/10.1016/j.mechrescom.2009.09.003
32. Li Y, Feng X-Q, Cao Y-P, Gao H (2010) A monte carlo form-finding method for large scale regular and irregular tensegrity structures. Int J Sol Struct 47(14–15):1888–1898. https://doi.org/10.1016/j.ijsolstr.2010.03.026
33. Barnes MR (1999) Form finding and analysis of tension structures by dynamic relaxation. Int J sp struct 14(2):89–104. https://doi.org/10.1260/0266351991494722
34. Ali NBH, Rhode-Barbarigos L, Smith IF (2011) Analysis of clustered tensegrity structures using a modified dynamic relaxation algorithm. Int J Sol Struct 48(5):637–647. https://doi.org/10.1016/j.ijsolstr.2010.10.029
35. Lee S, Lieu QX, Vo TP, Lee J (2022) Deep neural networks for form-finding of tensegrity structures. Mathematics 10(11):1822. https://doi.org/10.3390/math10111822
36. Paiva VA, Kurka PR, Izuka JH (2024) Analytical definitions of connectivity, incidence and node matrices for t-struts tensegrity prisms. Mech Res Commun. https://doi.org/10.1016/j.mechrescom.2024.104271
37. Tam K-M, Maia Avelino R, Kudenko D, Van Mele T, Block P (2024) Well-conditioned ai-assisted sub-matrix selection for numerically stable constrained form-finding of reticulated shells using geometric deep q-learning. Meccanica. https://doi.org/10.1007/s11012-024-01769-3
38. Zhang D, Qin A, Chen Y, Lu G (2023) A machine learning approach to predicting mechanical behaviour of non-rigid foldable square-twist origami. Eng Struct 278:115497. https://doi.org/10.1016/j.engstruct.2022.115497
39. Domer B, Fest E, Lalit V, Smith IF (2003) Combining dynamic relaxation method with artificial neural networks to enhance simulation of tensegrity structures. J Struct Eng 129(5):672–681. https://doi.org/10.1061/(ASCE)0733-9445(2003)129:5(672)
40. Sun Z, Zhao L, Liu K, Jin L, Yu J, Li C (2022) An advanced form-finding of tensegrity structures aided with noise-tolerant zeroing neural network. Neural CompütAppl. https://doi.org/10.1007/s00521-021-06745-6
41. Liu K, Wu J, Paulino GH, Qi HJ (2017) Programmable deployment of tensegrity structures by stimulus-responsive polymers. Scientific reports 7(1):3511. https://doi.org/10.1038/s41598-017-03412-6
42. Caluwaerts K, Despraz J, Işçen A, Sabelhaus AP, Bruce J, Schrauwen B, SunSpiral V (2014) Design and control of compliant tensegrity robots through simulation and hardware validation. J Royal Society Interface 11(98):20140520. https://doi.org/10.1098/rsif.2014.0520
43. Christoforou EG, Phocas MC, Matheou M, Müller A (2019) Experimental implementation of the 'effective 4-bar method'on a reconfigurable articulated structure. Structures 20:157–165. https://doi.org/10.1016/j.istruc.2019.03.009. **(Elsevier)**
44. Oppenheim I, Williams W (2000) Geometric effects in an elastic tensegrity structure. J Elast Phys Sci Sol 59(1):51–65. https://doi.org/10.1023/A:1011092811824
45. Davini C, Micheletti A, Podio-Guidugli P (2016) On the impulsive dynamics of t3 tensegrity chains. Meccanica 51:2763–2776. https://doi.org/10.1007/s11012-016-0495-y
46. Connelly R, Terrell M (1995) Globally rigid symmetric tensegrities. Struct Topology
47. Fraternali F, Carpentieri G, Amendola A (2015) On the mechanical modeling of the extreme softening/stiffening response of axially loaded tensegrity prisms. J Mech Phys Sol 74:136–157. https://doi.org/10.1016/j.jmps.2014.10.010
48. Chen Y, Yan J, Sareh P, Feng J (2019) Nodal flexibility and kinematic indeterminacy analyses of symmetric tensegrity structures using orbits of nodes. Int J Mech Sci 155:41–49. https://doi.org/10.1016/j.ijmecsci.2019.02.021
49. Phil K (2017) Matlab Deep Learning with Machine Learning. Neural Networks and Artificial Intelligence. Apress, New York
50. Rojas R (1996) Neural Networks: a Systematic Introduction. Springer, Berlin
51. Song K, Scarpa F, Schenk M (2024) Manufacturing sensitivity study of tensegrity structures using monte carlo simulations. Int J Sol Struct. https://doi.org/10.1016/j.ijsolstr.2024.112878
52. Herrmann D, Schaeffer L, Schmitt L, Körber W, Merker L, Zentner L, Böhm V (2024) Compliant robotic arm based on a tensegrity structure with x-shaped members.

In: 2024 IEEE 7th international conference on soft robotics (RoboSoft), pp. 1042–1047. IEEE
53. Boggs PT, Tolle JW (1995) Sequential quadratic programming. Acta numerica 4:1–51. https://doi.org/10.1017/S0962492900002518
54. Mirjalili S, Mirjalili S (2019) Genetic algorithm. Evolutionary algorithms neural netw: Theory appl. https://doi.org/10.1007/978-3-319-93025-1

7 DISCUSSION

This chapter synthesizes the findings from the preceding studies, highlighting the interconnections between them and their broader implications. By examining the methodologies, results, and potential applications, this discussion aims to provide a cohesive understanding of how each chapter contributes to the overall research objectives. The chapter is divided into subsections to address key themes, including educational purposes of the research, relevant reports not available in the papers, and the relevance of tensegrity structures across different fields.

7.1 Education in physics and engineering

Accelerometers have been widely used by the engineering community due to their high accuracy and frequency range. However, they can be expensive, introduce load errors in light structures, and may require wired connections to transfer data.

The membrane (Chapter 4) and tensegrity beam (Chapter 5) works applied image processing and presented equivalent accuracy. Recently, the use of image processing has been increasing in popularity because cameras have become more accessible as their technology and manufacturing have advanced. Nowadays, most people have access to cameras in their smartphones, therefore, the experiments reported in this thesis may also serve as inspiration for educational experiments by teachers in school laboratories, which were only possible at universities with a dedicated set of sensors. The limited frames per second (FPS) is the main drawback of using image processing to acquire vibration data compared to accelerometer-based instruments. Still, cameras with higher FPS rates have been developed by many industries, followed by a decrease in their prices, which favors image processing as a promising method for acquiring low vibration frequencies in light structures. Additionally, tensegrity systems offer challenges in the manufacturing process and material selection, which generates the possibility to integrate units of study in a multidisciplinary project.

7.2 Relevant reports

The tensegrity beam paper presents a static analysis addressing large displacements. This introduces nonlinearity of a geometric nature, as member stiffness varies with their orientations, and of a force-density nature, since stiffness increases with internal stresses. However, it is important to clarify that the modal analysis performed on the deformed configurations is linear. Additionally, the occurrence of slack cables is an important topic in the research community (Kan *et al.*, 2018b). Since cables can only withstand tensile forces, they slack if subjected to compressive forces, introducing another form of nonlinearity that must be addressed. In the nonlinear static analysis presented in the tensegrity beam study (Chapter 4), cable stiffness is set to zero whenever their length becomes shorter than their natural length. To delay the occurrence of slack cables in this study, the elastic bands are pre-stressed at the start of the experiment. This is an improvement of the methodology in (Paiva, 2019), where elastic tendons were initially relaxed. In that earlier work, the tendons alternated between slack and stressed states as the guying load increased, leading to nonlinearities in the load versus natural frequency plots. The camera used in the static and vibration experiments has a resolution of 4160x3120 pixels, 13 MP, f/2.0 aperture, 30 fps and was placed 2.5 meters away from the structure to minimize perspective errors.

Section *6.3.2 Relevant comments* in the form-finding paper (Chapter 6) highlights an issue regarding the method related to the initial guess for the nonlinear programming routine. Since there are two possible solutions, an inconvenient initial guess might not converge or lead to an upside down module (Figure 7.1), which compromises the whole mechanism. The normal vector suggested to provide an educated initial guess can be graphically represented in Figure 7.2. Also, section *5.2 Form-finding of the six quadruplex case* mentions it is convenient to alternate clockwise and counterclockwise modules to avoid a spiral shape. Figure 7.3 shows that scenario, which may be useful in other applications, but is undesirable in this arm design. The expansion equations that define the height h and vertical cable v generated by the direct application of $t = 4$ (four struts) lead to equations 7.1 and 7.2, respectively, and the form-finding functions f are described in equations 7.3 and 7.4 for clockwise and counterclockwise modules, respectively. Where, x, y and z represent the node coordinates associated to an $\mathbf{n}$ position vector, and b and l are the bar and horizontal cable, respectively. These three figures, expansion equations and form-finding functions have been removed from the paper for conciseness, but fit the scope of this thesis.

$$b^2 = \|\mathbf{n_2} - \mathbf{n_8}\|^2 \longrightarrow h^2 = b^2 - (x_2 - x_8)^2 - (y_2 - y_8)^2 \tag{7.1}$$

$$v^2 = \|\mathbf{n_2} - \mathbf{n_5}\|^2 \longrightarrow v^2 = h^2 + (x_2 - x_5)^2 + (x_2 - x_5)^2 \tag{7.2}$$

The neural network applied in the paper is described in terms of size and training parameters, but is not thoroughly explained. The model was developed using MATLAB's neural network toolbox, with training based on the Bayesian regularization algorithm. The selection of these parameters was achieved through an iterative process of trial and error. Various configurations and training algorithms available within the MATLAB toolbox were evaluated to find a model that best balanced performance accuracy with computational effort. Bayesian regularization minimizes a combination of squared errors and weights, adjusting the network's configuration throughout training to enhance generalization (Foresee; Hagan, 1997; MacKay, 1992). This regularization operates within the Levenberg-Marquardt algorithm, where backpropagation calculates the Jacobian of performance with respect to network weights and biases.

$$
\begin{aligned}
f_1 &= (x_3 - x_5)^2 + (y_3 - y_5)^2 + (z_3 - z_5)^2 - b^2 \\
f_2 &= (x_4 - x_6)^2 + (y_4 - y_6)^2 + (z_4 - z_6)^2 - b^2 \\
f_3 &= (x_1 - x_7)^2 + (y_1 - y_7)^2 + (z_1 - z_7)^2 - b^2 \\
f_4 &= (x_2 - x_8)^2 + (y_2 - y_8)^2 + (z_2 - z_8)^2 - b^2 \\
f_5 &= (x_5 - x_6)^2 + (y_5 - y_6)^2 + (z_5 - z_6)^2 - l^2 \\
f_6 &= (x_6 - x_7)^2 + (y_6 - y_7)^2 + (z_6 - z_7)^2 - l^2 \\
f_7 &= (x_7 - x_8)^2 + (y_7 - y_8)^2 + (z_7 - z_8)^2 - l^2 \\
f_8 &= (x_8 - x_5)^2 + (y_8 - y_5)^2 + (z_8 - z_5)^2 - l^2 \\
f_9 &= (x_2 - x_5)^2 + (y_2 - y_5)^2 + (z_2 - z_5)^2 - v_1^2 \\
f_{10} &= (x_3 - x_6)^2 + (y_3 - y_6)^2 + (z_3 - z_6)^2 - v_2^2 \\
f_{11} &= (x_4 - x_7)^2 + (y_4 - y_7)^2 + (z_4 - z_7)^2 - v_3^2 \\
f_{12} &= (x_1 - x_8)^2 + (y_1 - y_8)^2 + (z_1 - z_8)^2 - v_4^2
\end{aligned}
\tag{7.3}
$$

$$
\begin{aligned}
f_1 &= (x_3 - x_5)^2 + (y_3 - y_5)^2 + (z_3 - z_5)^2 - b^2 \\
f_2 &= (x_4 - x_6)^2 + (y_4 - y_6)^2 + (z_4 - z_6)^2 - b^2 \\
f_3 &= (x_1 - x_7)^2 + (y_1 - y_7)^2 + (z_1 - z_7)^2 - b^2 \\
f_4 &= (x_2 - x_8)^2 + (y_2 - y_8)^2 + (z_2 - z_8)^2 - b^2 \\
f_5 &= (x_5 - x_6)^2 + (y_5 - y_6)^2 + (z_5 - z_6)^2 - l^2 \\
f_6 &= (x_6 - x_7)^2 + (y_6 - y_7)^2 + (z_6 - z_7)^2 - l^2 \\
f_7 &= (x_7 - x_8)^2 + (y_7 - y_8)^2 + (z_7 - z_8)^2 - l^2 \\
f_8 &= (x_8 - x_5)^2 + (y_8 - y_5)^2 + (z_8 - z_5)^2 - l^2 \\
f_9 &= (x_4 - x_5)^2 + (y_4 - y_5)^2 + (z_4 - z_5)^2 - v_4^2 \\
f_{10} &= (x_1 - x_6)^2 + (y_1 - y_6)^2 + (z_1 - z_6)^2 - v_1^2 \\
f_{11} &= (x_2 - x_7)^2 + (y_2 - y_7)^2 + (z_2 - z_7)^2 - v_2^2 \\
f_{12} &= (x_3 - x_8)^2 + (y_3 - y_8)^2 + (z_3 - z_8)^2 - v_3^2
\end{aligned}
\tag{7.4}
$$

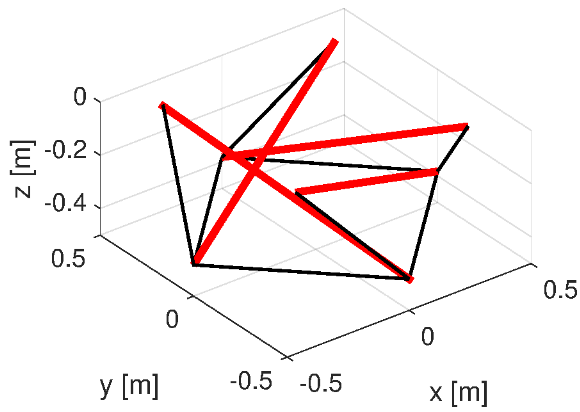

Figure 7.1 – Upside down quadruplex module.

7.3 Interconnection between papers

The methodology for nonlinear static analysis presented in Sections *2.1 Static Analysis of Tensegrity Structures* and *2.2 Nonlinear Static Analysis* of the tensegrity beam paper (Chapter 4) can be validated using results from ANSYS, applying the same commands used in the membrane paper (Chapter 3). This can be done by modeling the bars and cables, including the guying cable, with LINK180 elements. A fictitious thermal expansion constant can be assigned to the material of the guying cable, and a negative temperature load can be ap-

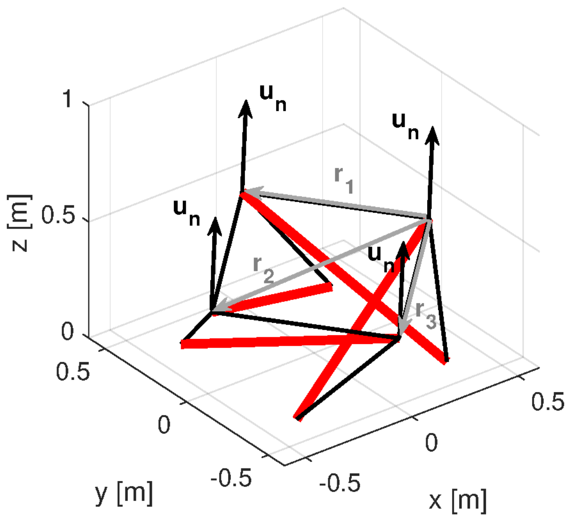

Figure 7.2 – Normal vector of the top base.

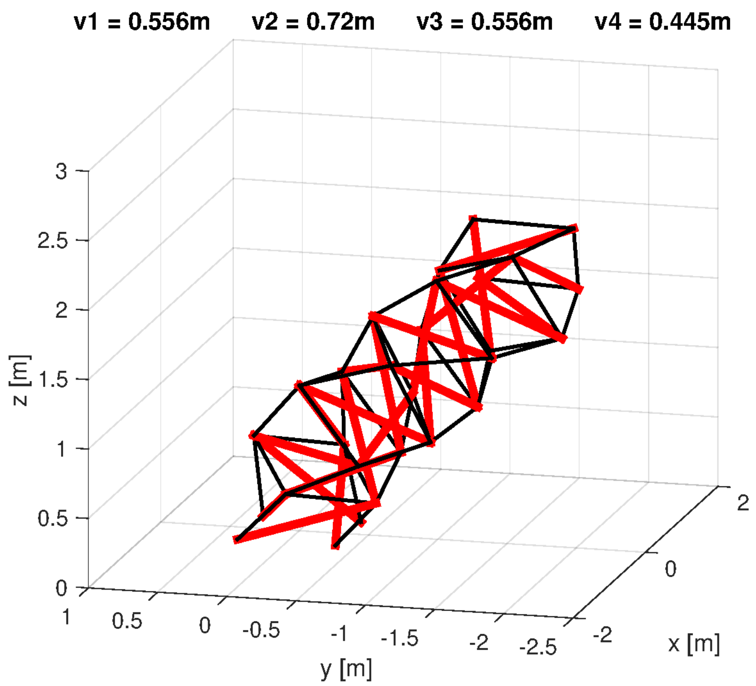

Figure 7.3 – Spiral generated by anticlockwise quadruplex modules.

plied to reduce its length, thereby generating a force on the beam tip directed along the guying cable. However, during the nonlinear analysis, some cables may become slack, requiring the application of conditional commands to remove their stiffness in compression. Given the complexity and temporary nature of this approach, it may be more convenient to apply a load with a constant direction, ensuring that no cable enters a slack state. This alternative will validate the model with significantly less effort. As an example, the first vibration mode in configuration 4 is analyzed in Ansys (Figure 7.4). The deformed configuration and natural frequency validate the numerical model. These Ansys analyzes are omitted in the paper as the results are redundant, but the code associated with this simulation in the *Ansys Mechanical APDL* platform is available in the public repository <https://github.com/FictorP/Tensegrity/blob/main/beam/modal/torreModalImpressa.txt>. Additionally, the natural frequencies obtained from image processing in both papers were determined using Kinovea as the tracking software, with the same 30 fps camera. All experimental vibration frequencies were extracted by observing the amplitude peaks in the frequency domain spectra.

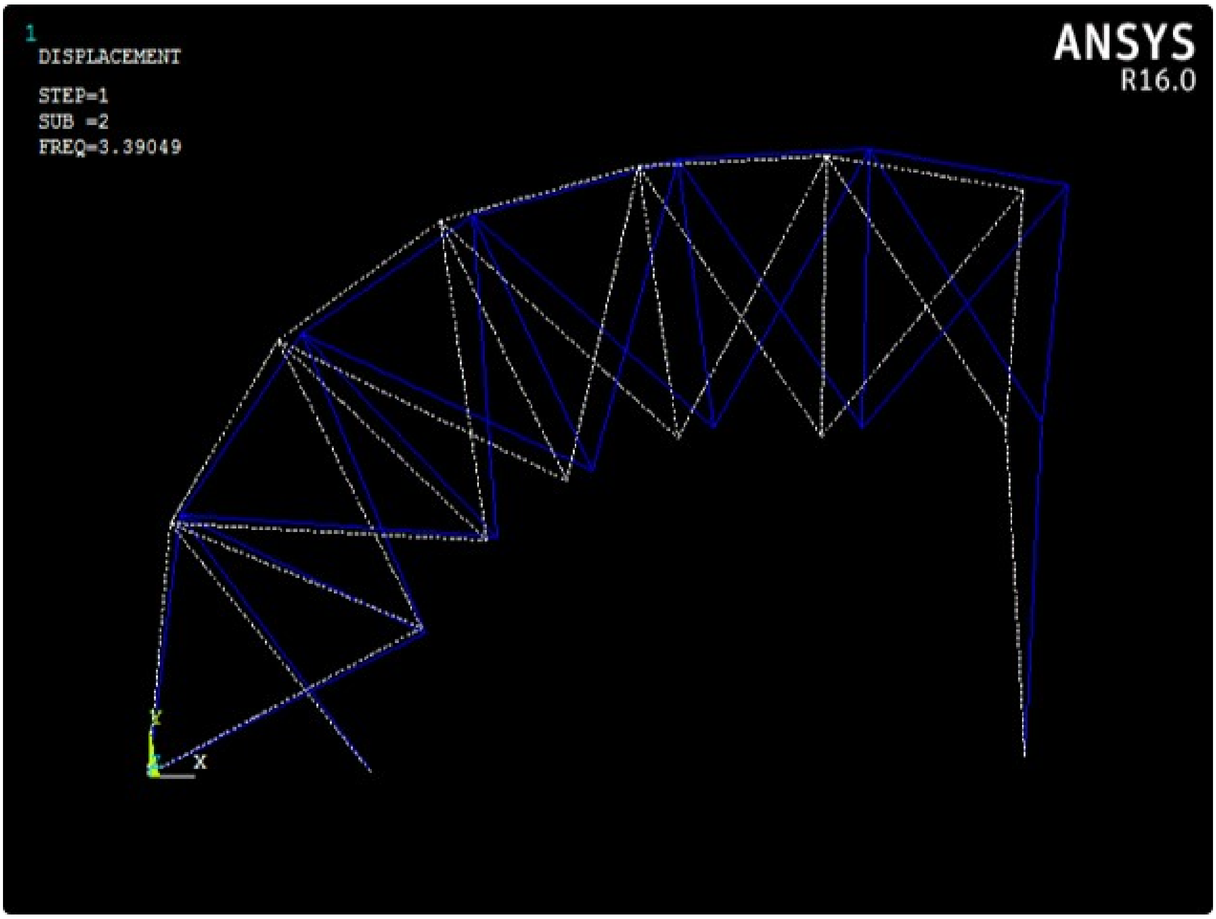

Figure 7.4 – First vibration mode in configuration 4 of the tensegrity beam analyzed in Ansys.

The form-finding work in Chapter 6 was initially developed to solve the four-strut prism only, but it became evident that a general definition for the incidence matrix could extend the method to cover any tensegrity prism stacking. This realization prompted the analytical study in Chapter 6, which required a pause in the form-finding analysis to develop the incidence matrices using floor and ceiling functions. The connectivity matrix contains the same information in a different format, allowing for straightforward formalization of connectivity definitions and making the paper self-sufficient. Even though the paper in Chapter 5 is essential for advancing the form-finding study, its analytical scope points in a different direction, justifying its publication as a separate manuscript.

In Section *4.2 Polynomial Interpolation of Nodal Positions* of the tensegrity beam paper (Chapter 4), a polynomial approximation is adjusted to the nonlinear static results. A similar technique is employed to approximate the workspace of the tensegrity arm in Sections *4. Inverse kinematics* and *5.4. Inverse kinematics of the six quadruplex case* in the form-finding paper (Chapter 6). While both models perform relatively quickly, they are not fully optimized to meet real-time requirements for typical controller strategies. However, these straightforward polynomial approximations do offer a real-time solution with an acceptable level of relative error. This metric extends to the execution time based comparisons in section *5.3 Comparison to other form-finding techniques*.

Providing a general guide on solid mechanics of tensegrity systems is an overall objective of this thesis. Chapters 4, 5 and 6 contribute to this goal because they complement each other when covering statics, kinematics, vibrations and control of tensegrity and membrane mechanisms from analytical, numerical and experimental sources in two and three dimensions.

8 CONCLUSIONS

When properly optimized, tensegrity structures can be ahead of trusses and beams in terms of structural efficiency. Tensegrity systems are also useful to develop mechanisms because of their versatility in terms of shape transformation. These advantages are convenient for space engineering applications, such as arms and towers for exploration probes and satellites. Satellite antennas usually require a reflector surface, which can be replaced by a membrane and combined with a tensegrity to assemble a tensegrity-membrane system. This work presents three separate studies to assess those possibilities: a vibration study of a prestressed membrane, a statics and vibration study of a bi-dimensional tensegrity beam that is pulled by its tip and shows large displacements, and a kinematics study of a three-dimensional tensegrity arm that expands from a compact shape and bows into an arch. Additionally, a theoretical contribution covering analytical expressions to model tensegrity prisms is presented.

The membrane prototype is made of thin rubber and cut in a triangular shape. This shape is beneficial because only one load cell is required to find the traction forces in all three vertexes. The membrane is mounted on an aluminium frame and hung by cables attached to its vertexes. Four load levels are applied to generate four stressed configurations. The first vibration frequency is extracted by image processing in each configuration. In this experiment, the image processing technique is convenient because the weight of the accelerometer would significantly impact the behavior of the structure, as its mass is greater than the prototype's. A numerical model is implemented in *ANSYS Mechanical APDL* for both static and vibration analyses. The cable and membrane are modelled by LINK180 and SHELL281 elements, respectively. The stresses from the static analysis are saved and applied to the vibration analysis with the INISTATE command. The density of the membrane is increased by a factor of 2.6 to account for the air displacement. The relative error between numerical and experimental results remains within 5.02%, which suggests that the numerical model is accurate and can be combined with a tensegrity to assemble a tensegrity-membrane system.

The tensegrity beam is formed by six pairs of crossed bars connected by pin joints to assemble a class 2 tensegrity structure. The design of the bars forces the experiment to remain bi-dimensional. Rubber bands perform the function of the cables and are prestressed from the start. The prototype is hung upside down and loaded by a pulling cable attached to the tip of the beam. The structure is subject to self weight only (configuration 0) and four load levels (configurations 1 to 4). The vibration frequencies are extracted through image processing and accelerometer data in each configuration. An algorithm for nonlinear static analysis is implemented to model the structure and validated with the experimental results. The methodology combines a standard finite element procedure for prestressed tensegrity systems with Euler's incremental loads technique for nonlinear analysis. The numerical modal analysis compares the first and second vibration frequencies of each configuration with both experimental techniques and remains within a relative error of 7%. The numerical model then calculates all intermediate configurations from 1 to 4 and extracts their first ten natural frequencies. Higher loads cause slackness in a few cables, which contributes to a lower stiffness and higher natural frequencies. However, higher loads also reduce the effective length of the structure and increase the stresses in the taut cables, which contributes to a higher stiffness and, therefore, higher natural frequencies. The combination of those phenomena is verified by this study to cause higher natural frequencies. Even though the algorithm is efficient, a real time application would require faster evaluation of the static configurations, therefore a polynomial approximation is employed to predict the trajectories of all nodes, and the coefficients are presented in matrix form. Proportional damping parameters are estimated and a H_∞ control is applied as an example that the model is valid. The MATLAB scripts associated with the static and vibration analyses can be publicly retrieved at <https://github.com/FictorP/Tensegrity/tree/main/beam>.

Most works involving tensegrity prisms apply triplex or quadruplex modules, which are formed by three or four struts, respectively. Prisms with more than four struts should be explored by the scientific community, especially in multidisciplinary studies, but their node and connectivity matrices may offer higher complexity to derive. The analytical definitions of connectivity, incidence and node matrices provided in this thesis cover prisms with four or more struts and might be useful to insipire more research involving prisms with five or more bars. Also, these definitions may be key to adapt methods that are functional only for prisms with a fixed number of struts, and generalize them for a larger scope. They are originated from geometry and pattern recognition. Examples for four to seven struts prisms are provided.

The tensegrity arm is formed by six quadruplex modules, but the presented methodology is valid for any stacking of cylindrical tensegrity modules because it applies the definitions that use floor and ceiling functions described in the analytical study. The modules are capable of shrinking into a flat configuration and expanding into a three-dimensional shape. They are stacked bar to bar to assemble a high aspect ratio class 2 tensegrity tower. This transformation from a flat system to a high tower is addressed as the first stage, while the second stage is associated with transforming the tower into a bowed structure.

The modules remain regular in the first stage, which leads to a simplified kinematics methodology. The bowing movement created in the second stage of the study relies on irregular modules, therefore, requiring more sophisticated kinematics methodologies. A form-finding using the incidence definitions with floor and ceiling functions is adjusted and implemented to calculate this mechanism. Most member lengths are provided, and the algorithm finds the length of the missing element. This technique can be understood as an optimization problem because the structure reaches stability when the cables cannot be shortened anymore. Therefore, the length of the last cable must be minimized. The Newton-Raphson method is used to solve the nonlinear system of equations and nonlinear programming is applied to minimize the error. This form-finding method is compared to the dynamic relaxation algorithm and the Newton-Raphson procedure is compared to the MATLAB inbuilt Levenberg-Marquardt routine. The Levenberg-Marquardt based form-finding method has shown to be more efficient for a large number of iterations, because it reuses cached data, while the Newton-Raphson version outperforms it for a small number of iterations due to the pre calculated Jacobian matrix.

Regardless of the minimization method, the form-finding procedure calculates the node positions (and by extension, the end-effector position) for a given set of cables, but most applications have a target position and require the associated cables set in real time to feed their actuators. A large collection of cable sets is used to calculate an equally large collection of points within the workspace of the mechanism end-effector. The workspace surface is approximated by a polynomial fit that contains all the possible positions the arm can reach. This inverse kinematics problem is solved by a previously trained neural network, and by minimizing the squared error using the genetic algorithm and sequential quadratic programming. The results indicate that the genetic algorithm based inverse kinematics function provides results with a maximum error of 4.78%, but the result is not obtained in real time. The MATLAB scripts associated with the form-finding method and inverse kinematics are publicly available at <https://github.com/FictorP/Tensegrity/tree/main/formfinding>. For applications that require fast responses, the neural networks provide outputs with a maximum error of 1.48% with the drawback of requiring a previously calculated data set of end-effector positions associated with their respective cable lengths and training sessions. This design can be applied as a transportable bridge to aid accessing disaster areas or as a manipulator to carry a camera on top of a space exploration probe.

The studies presented in this thesis are advances of the research developed in (Paiva, 2019). The prestressed membrane study fills the gap between the previously suggested application of a tensegrity-membrane system to assemble a satellite reflector antenna. The tensegrity beam prototype is a substantial improvement of the previous manipulator, which did not have any feature to avoid the occurrence of slack cables or in depth motion. The tensegrity arm design builds upon the expansion study of a single module and develops a full kinematical form-finding method. These improvements are relevant for achieving the individual objectives of the four presented projects and, by extension, the overall goal of demonstrating the viability of tensegrity and membrane systems. This is accomplished by subjecting them to a broad set of solid mechanics studies, including two- and three-dimensional statics and dynamics through analytical, numerical and experimental approaches. The advantages of tensegrity systems justify their application in engineering structures and mechanisms. However, the industry is relatively conservative regarding novel designs and solutions. This thesis contributes to the collection of methodologies and experiments, which is a necessary step to build the acceptance of tensegrities among the community.

Based on the literature review and the concluding remarks, the following topics are relevant future work directions:

- The membrane prototype does not feature catenary edges, which causes wrinkling in high stresses. In an advanced iteration, the prototype and model should present catenary edges.
- Both numerical models of membrane and tensegrity have been validated with experiments. These models should be combined to assemble a tensegrity-membrane system.
- Analytical definitions of node, incidence and connectivity matrices for prisms assemblies are still missing. Finding general formulae for prism assemblies using the definitions provided for single modules is a natural sequence of this work and an open challenge for the community.
- The experimental work with the beam is planar, but the methodology can be applied to three-dimensional systems. The 3D tensegrity arm design should be built and experimented under the same methodologies of the planar tensegrity beam.

- The tensegrity arm suggested is grounded and would require a moving base to travel, this feature limits its range of applications. Therefore, the methodologies proposed should be applied to design a tensegrity robot that can crawl or roll.

- Tensegrity systems frequently feature in biological studies, and the methodologies developed in this thesis should be applied to support multidisciplinary research.

BIBLIOGRAPHY

Agogino, A. K.; SunSpiral, V.; Atkinson, D. **Super Ball Bot-structures for planetary landing and exploration**. [S.l.], 2018.

Ahmed, A. R.; Gauntlett, O. C.; Camci-Unal, G. Origami-inspired approaches for biomedical applications. **ACS omega**, v. 6, n. 1, p. 46–54, 2020.

Ali, N. B. H.; Rhode-Barbarigos, L.; Smith, I. F. Analysis of clustered tensegrity structures using a modified dynamic relaxation algorithm. **International Journal of Solids and Structures**, v. 48, n. 5, p. 637–647, 2011.

Amendola, A.; Carpentieri, G.; De Oliveira, M.; Skelton, R.; Fraternali, F. Experimental investigation of the softening–stiffening response of tensegrity prisms under compressive loading. **Composite Structures**, v. 117, p. 234–243, 2014.

De Angelo, M.; Placidi, L.; Nejadsadeghi, N.; Misra, A. Non-standard timoshenko beam model for chiral metamaterial: identification of stiffness parameters. **Mechanics Research Communications**, v. 103, p. 103462, 2020.

Arsenault, M.; Gosselin, C. M. Kinematic and static analysis of a 3-pups spatial tensegrity mechanism. **Mechanism and Machine Theory**, v. 44, n. 1, p. 162–179, 2009.

Ashwear, N.; Eriksson, A. Natural frequencies describe the pre-stress in tensegrity structures. **Computers & structures**, v. 136, p. 162–171, 2014.

Bansod, Y. D.; Matsumoto, T.; Nagayama, K.; Bursa, J. A finite element bendo-tensegrity model of eukaryotic cell. **Journal of biomechanical engineering**, v. 140, n. 10, p. 101001, 2018.

Carpentieri, G.; Skelton, R. E.; Fraternali, F. Minimum mass and optimal complexity of planar tensegrity bridges. **International Journal of Space Structures**, v. 30, n. 3-4, p. 221–243, 2015.

Carpentieri, G.; Skelton, R. E.; Fraternali, F. A minimal mass deployable structure for solar energy harvesting on water canals. **Structural and Multidisciplinary Optimization**, v. 55, n. 2, p. 449–458, 2017.

Crisfield, M. A. **Non-linear finite element analysis of solids and structures**. [S.l.]: John Wiley & Sons, 1991.

Estrada, G. G.; Bungartz, H.-J.; Mohrdieck, C. Numerical form-finding of tensegrity structures. **International Journal of Solids and Structures**, v. 43, n. 22-23, p. 6855–6868, 2006.

Faroughi, S.; Lee, J. Geometrical nonlinear analysis of tensegrity based on a co-rotational method. **Advances in Structural Engineering**, v. 17, n. 1, p. 41–51, 2014.

Feron, J.; Boucher, L.; Denoël, V.; Latteur, P. Optimization of footbridges composed of prismatic tensegrity modules. **Journal of Bridge Engineering**, v. 24, n. 12, p. 04019112, 2019.

Fonseca, L. M.; Rodrigues, G. V.; Savi, M. A. An overview of the mechanical description of origami-inspired systems and structures. **International Journal of Mechanical Sciences**, v. 223, p. 107316, 2022.

Foresee, F. D.; Hagan, M. T. Gauss-newton approximation to bayesian learning. In: IEEE. **Proceedings of international conference on neural networks (ICNN'97)**. [S.l.], 1997. v. 3, p. 1930–1935.

Fraternali, F.; Senatore, L.; Daraio, C. Solitary waves on tensegrity lattices. **Journal of the Mechanics and Physics of Solids**, v. 60, n. 6, p. 1137–1144, 2012.

Fuller, R. B.; Applewhite, E. J. **Synergetics: Explorations in the Geometry of Thinking**. [S.l.]: Macmillan, 1975.

Furuya, H. Concept of deployable tensegrity structures in space application. **International Journal of Space Structures**, v. 7, n. 2, p. 143–151, 1992.

Gebara, C. A.; Carpenter, K. C.; Woodmansee, A. Tensegrity ocean world landers. In: **AIAA Scitech 2019 Forum**. [S.l.: s.n.], 2019. p. 0868.

Goyal, R.; Bryant, T.; Majji, M.; Skelton, R. E.; Longman, A. Design and control of growth adaptable artificial gravity space habitat. In: **AIAA SPACE and Astronautics Forum and Exposition**. [S.l.: s.n.], 2017. p. 5141.

Holland, D. B.; Stanciulescu, I.; Virgin, L. N.; Plaut, R. H. Vibration and large deflection of cantilevered elastica compressed by angled cable. **AIAA journal**, v. 44, n. 7, p. 1468–1476, 2006.

Hrazmi, I.; Averseng, J.; Quirant, J.; Jamin, F. Deployable double layer tensegrity grid platforms for sea accessibility. **Engineering Structures**, v. 231, p. 111706, 2021.

Hu, Y.; Chen, W.; Chen, Y.; Zhang, D.; Qiu, Z. Modal behaviors and influencing factors analysis of inflated membrane structures. **Engineering Structures**, v. 132, p. 413–427, 2017.

Hu, Y.; Guo, W.; Zhu, W.; Xu, Y. Local damage detection of membranes based on bayesian operational modal analysis and three-dimensional digital image correlation. **Mechanical Systems and Signal Processing**, v. 131, p. 633–648, 2019.

Ingber, D. E. Tensegrity i. cell structure and hierarchical systems biology. **Journal of Cell Science**, v. 116, n. 7, p. 1157–1173, 2003.

Jahn, H.; Böhm, V.; Zentner, L. Analysis of deformation in tensegrity structures with curved compressed members. **Meccanica**, p. 1–12, 2024.

Jáuregui, V. G. **Tensegrity structures and their application to architecture**. Cantabria: Ed. Universidad de Cantabria, 2020. v. 2.

Jiang, S.; Skelton, R. E.; Peraza Hernandez, E. A. Analytical equations for the connectivity matrices and node positions of minimal and extended tensegrity plates. **International Journal of Space Structures**, v. 35, n. 3, p. 47–68, 2020.

Kan, Z.; Peng, H.; Chen, B. Complementarity framework for nonlinear analysis of tensegrity structures with slack cables. **AIAA Journal**, v. 56, n. 12, p. 5013–5027, 2018.

Kan, Z.; Peng, H.; Chen, B. Complementarity framework for nonlinear analysis of tensegrity structures with slack cables. **AIAA Journal**, v. 56, n. 12, p. 5013–5027, 2018.

Kebiche, K.; Kazi-Aoual, M.; Motro, R. Geometrical non-linear analysis of tensegrity systems. **Engineering structures**, v. 21, n. 9, p. 864–876, 1999.

Kitipornchai, S.; Kang, W.; Lam, H.-F.; Albermani, F. Factors affecting the design and construction of lamella suspen-dome systems. **Journal of Constructional Steel Research**, v. 61, n. 6, p. 764–785, 2005.

Koohestani, K. Form-finding of tensegrity structures via genetic algorithm. **International Journal of Solids and Structures**, v. 49, n. 5, p. 739–747, 2012.

Koohestani, K. On the analytical form-finding of tensegrities. **Composite Structures**, v. 166, p. 114–119, 2017.

Koohestani, K. Innovative numerical form-finding of tensegrity structures. **International Journal of Solids and Structures**, v. 206, p. 304–313, 2020.

Kukathasan, S.; Pellegrino, S. Vibration of prestressed membrane structures in air. In: **43RD AIAA/ASME/ASCE/AHS/ASC STRUCTURES, STRUCTURAL DYNAMICS, AND MATERIALS CONFERENCE**. [S.l.: s.n.], 2002.

Kurka, P.; Paiva, V.; Teixeira, L.; Izuka, J.; Gonzalez, P. Dynamic behavior and vibration analysis of tensegrity-membrane structures. In: **Proceedings of ISMA**. [S.l.: s.n.], 2018.

Kurka, P. R.; Izuka, J. H.; Gonzalez, P.; Burdick, J.; Elfes, A. Vibration of a long, tip pulled deflected beam. **AIAA journal**, v. 52, n. 7, p. 1559–1563, 2014.

Kurka, P. R.; Paiva, V. A.; Silva-Teixeira, L. H.; Ramos, P. G.; Izuka, J. H. A dynamical model for the control of a guyed tensegrity beam under large displacements. **Journal of Mechanisms and Robotics**, v. 16, n. 9, 2024.

Leipold, M.; Runge, H.; Sickinger, C. Large sar membrane antennas with lightweight deployable booms. In: **28th ESA Antenna Workshop on Space Antenna Systems and Technologies, ESA/ESTEC**. [S.l.: s.n.], 2005.

Lessard, S.; Castro, D.; Asper, W.; Chopra, S. D.; Baltaxe-Admony, L. B.; Teodorescu, M.; SunSpiral, V.; Agogino, A. A bio-inspired tensegrity manipulator with multi-dof, structurally compliant joints. In: IEEE. **2016 IEEE/RSJ International Conference on Intelligent Robots and Systems (IROS)**. [S.l.], 2016. p. 5515–5520.

Li, D.; Zheng, Z.-L.; Yang, R.; Zhang, P. Analytical solutions for stochastic vibration of orthotropic membrane under random impact load. **Materials**, v. 11, n. 7, p. 1231, 2018.

Li, Y.; Feng, X.-Q.; Cao, Y.-P.; Gao, H. A monte carlo form-finding method for large scale regular and irregular tensegrity structures. **International Journal of Solids and Structures**, v. 47, n. 14-15, p. 1888–1898, 2010.

Liedl, T.; Högberg, B.; Tytell, J.; Ingber, D. E.; Shih, W. M. Self-assembly of three-dimensional prestressed tensegrity structures from dna. **Nature nanotechnology**, v. 5, n. 7, p. 520–524, 2010.

Liu, C.; Deng, X.; Liu, J.; Zheng, Z. Impact-induced nonlinear damped vibration of fabric membrane structure: theory, analysis, experiment and parametric study. **Composites Part B: Engineering**, v. 159, p. 389–404, 2019.

Liu, C.; Wang, F.; He, L.; Deng, X.; Liu, J.; Wu, Y. Experimental and numerical investigation on dynamic responses of the umbrella membrane structure excited by heavy rainfall. **Journal of Vibration and Control**, v. 27, n. 5-6, p. 675–684, 2021.

Liu, C.; Wang, F.; Liu, J.; Deng, X.; Zhang, Z.; Xie, H. Theoretical and numerical studies on damped nonlinear vibration of orthotropic saddle membrane structures excited by hailstone impact load. **Shock and Vibration**, v. 2019, 2019.

Liu, C.-J.; Todd, M. D.; Zheng, Z.-L.; Wu, Y.-Y. A nondestructive method for the pretension detection in membrane structures based on nonlinear vibration response to impact. **Structural Health Monitoring**, v. 17, n. 1, p. 67–79, 2018.

Liu, R.; Yao, Y.-a. A novel serial–parallel hybrid worm-like robot with multi-mode undulatory locomotion. **Mechanism and Machine Theory**, v. 137, p. 404–431, 2019.

Liu, Y.; Bi, Q.; Yue, X.; Wu, J.; Yang, B.; Li, Y. A review on tensegrity structures-based robots. **Mechanism and Machine Theory**, v. 168, p. 104571, 2022.

Ma, S.; Chen, M.; Zhang, H.; Skelton, R. E. Statics of integrated origami and tensegrity systems. **International Journal of Solids and Structures**, v. 279, p. 112361, 2023.

Ma, Y.; Zhang, Q.; Dobah, Y.; Scarpa, F.; Fraternali, F.; Skelton, R. E.; Zhang, D.; Hong, J. Meta-tensegrity: Design of a tensegrity prism with metal rubber. **Composite Structures**, v. 206, p. 644–657, 2018.

MacKay, D. J. Bayesian interpolation. **Neural computation**, v. 4, n. 3, p. 415–447, 1992.

Maki, J.; Gruel, D.; McKinney, C.; Ravine, M.; Morales, M.; Lee, D.; Willson, R.; Copley-Woods, D.; Valvo, M.; Goodsall, T. *et al.* The mars 2020 engineering cameras and microphone on the perseverance rover: A next-generation imaging system for mars exploration. **Space Science Reviews**, v. 216, n. 8, p. 1–48, 2020.

Micheletti, A.; Ruscica, G.; Fraternali, F. On the compact wave dynamics of tensegrity beams in multiple dimensions. **Nonlinear Dynamics**, v. 98, n. 4, p. 2737–2753, 2019.

Michell, A. G. M. Lviii. the limits of economy of material in frame-structures. **The London, Edinburgh, and Dublin Philosophical Magazine and Journal of Science**, v. 8, n. 47, p. 589–597, 1904.

Motro, R. Tensegrity systems: The state of the art. **International Journal of Space Structures**, v. 7, n. 2, p. 75–83, 1992.

Murakami, H. Static and dynamics analysis of tensegrity structures. part 1. nonlinear equations of motion. **International Journal of Solid and Structures**, v. 38, p. 3599 – 3613, 2001.

Nagase, K.; Yamashita, T.; Kawabata, N. On a connectivity matrix formula for tensegrity prism plates. **Mechanics Research Communications**, v. 77, p. 29–43, 2016.

Ohsaki, M.; Zhang, J. Nonlinear programming approach to form-finding and folding analysis of tensegrity structures using fictitious material properties. **International Journal of Solids and Structures**, v. 69, p. 1–10, 2015.

Paiva, V. **Static, dynamic and modal analysis of tensegrity structures and mechanisms**. Tese (Doutorado) — State University of Campinas, 2019.

Paiva, V.; Silva-Teixeira, L.; Izuka, J.; Okabe, E.; Kurka, P. A form-finding method for deployable tensegrity arms and inverse kinematics. **Meccanica**, p. 1–16, 2024.

Paiva, V. A.; Kurka, P. R.; Izuka, J. H. Analytical definitions of connectivity, incidence and node matrices for t-struts tensegrity prisms. **Mechanics Research Communications**, v. 137, p. 104271, 2024.

Paul, C.; Valero-Cuevas, F. J.; Lipson, H. Design and control of tensegrity robots for locomotion. **IEEE Transactions on Robotics**, v. 22, n. 5, p. 944–957, 2006.

Pellegrino, S. **Mechanics of kinematically indeterminate structures**. Tese (Doutorado) — University of Cambridge, 1986.

Poppleton, E.; Urbanek, N.; Chakraborty, T.; Griffo, A.; Monari, L.; Göpfrich, K. Rna origami: design, simulation and application. **RNA biology**, v. 20, n. 1, p. 510–524, 2023.

Raj, R. P.; Guest, S. Using symmetry for tensegrity form-finding. **Journal of the International Association for Shell and Spatial Structures**, v. 47, n. 3, p. 245–252, 2006.

Rhode-Barbarigos, L.; Ali, N. B. H.; Motro, R.; Smith, I. F. Designing tensegrity modules for pedestrian bridges. **Engineering Structures**, v. 32, n. 4, p. 1158–1167, 2010.

Sabelhaus, A. P.; Bruce, J.; Caluwaerts, K.; Manovi, P.; Firoozi, R. F.; Dobi, S.; Agogino, A. M.; SunSpiral, V. System design and locomotion of superball, an untethered tensegrity robot. In: IEEE. **2015 IEEE international conference on robotics and automation (ICRA)**. [S.l.], 2015. p. 2867–2873.

Scarr, G. Helical tensegrity as a structural mechanism in human anatomy. **International Journal of Osteopathic Medicine**, v. 14, n. 1, p. 24–32, 2011.

Schorr, P.; Li, E. R. C.; Kaufhold, T.; Hernández, J. A. R.; Zentner, L.; Zimmermann, K.; Böhm, V. Kinematic analysis of a rolling tensegrity structure with spatially curved members. **Meccanica**, v. 56, p. 953–961, 2021.

Shi, C.; Guo, H.; Cheng, Y.; Liu, R.; Deng, Z. Design and multi-objective comprehensive optimization of cable-strut tensioned antenna mechanism. **Acta Astronautica**, v. 1, n. 178, p. 406–422, 2020.

Skelton, R.; Fraternali, F.; Carpentieri, G.; Micheletti, A. Minimum mass design of tensegrity bridges with parametric architecture and multiscale complexity. **Mechanics Research Communications**, v. 58, p. 124–132, 2014.

Skelton, R. E.; De Oliveira, M. C. **Tensegrity systems**. New York: Springer, 2009. v. 1.

Song, Z.; Ma, T.; Tang, R.; Cheng, Q.; Wang, X.; Krishnaraju, D.; Panat, R.; Chan, C. K.; Yu, H.; Jiang, H. Origami lithium-ion batteries. **Nature communications**, v. 5, n. 1, p. 3140, 2014.

Sumi, S.; Boehm, V.; Zimmermann, K. A multistable tensegrity structure with a gripper application. **Mechanism and Machine Theory**, v. 114, p. 204–217, 2017.

Sunny, M. R.; Kapania, R. K.; Sultan, C. Solution of nonlinear vibration problem of a prestressed membrane by adomian decomposition. **AIAA journal**, v. 50, n. 8, p. 1796–1800, 2012.

SunSpiral, V.; Agogino, A.; Atkinson, D. Super ball bot-structures for planetary landing and exploration, niac phase 2 final report. 2015.

Sychterz, A. C.; Smith, I. F. Using dynamic measurements to detect and locate ruptured cables on a tensegrity structure. **Engineering Structures**, v. 173, p. 631–642, 2018.

Teixeira, L.; Izuka, J.; Gonzalez, P.; Kurka, P. A numerical analysis of the dynamics of a tensegrity-membrane structure. In: **31st Congress of the International Council of the Aeronautical Sciences**. [S.l.: s.n.], 2018.

Tibert, A.; Pellegrino, S. Review of form-finding methods for tensegrity structures. **International Journal of Space Structures**, v. 18, n. 4, p. 209–223, 2003.

Tibert, A.; Pellegrino, S. Review of form-finding methods for tensegrity structures. **International Journal of Space Structures**, v. 26, n. 3, p. 241–255, 2011.

Tran, H. C.; Lee, J. Initial self-stress design of tensegrity grid structures. **Computers & structures**, v. 88, n. 9-10, p. 558–566, 2010.

Tran, H. C.; Lee, J. Geometric and material nonlinear analysis of tensegrity structures. **Acta Mechanica Sinica**, v. 27, n. 6, p. 938–949, 2011.

Vassart, N.; Motro, R. Multiparametered formfinding method: application to tensegrity systems. **International journal of space structures**, v. 14, n. 2, p. 147–154, 1999.

Veuve, N.; Sychterz, A. C.; Smith, I. F. Adaptive control of a deployable tensegrity structure. **Engineering Structures**, v. 152, p. 14–23, 2017.

Wang, Y.; Xu, X.; Luo, Y. Minimal mass design of active tensegrity structures. **Engineering Structures**, v. 234, p. 111965, 2021.

Wei, J.; Ma, R.; Liu, Y.; Yu, J.; Eriksson, A.; Tan, H. Modal analysis and identification of deployable membrane structures. **Acta Astronautica**, v. 152, p. 811–822, 2018.

Wendling, S.; Cañadas, P.; Chabrand, P. Toward a generalised tensegrity model describing the mechanical behaviour of the cytoskeleton structure. **Computer Methods in Biomechanics & Biomedical Engineering**, v. 6, n. 1, p. 45–52, 2003.

Wong, W.; Pellegrino, S. Wrinkled membranes i: experiments. **Journal of Mechanics of Materials and Structures**, v. 1, n. 1, p. 3–25, 2006.

Wong, W.; Pellegrino, S. Wrinkled membranes ii: analytical models. **Journal of Mechanics of Materials and Structures**, v. 1, n. 1, p. 27–61, 2006.

Wong, W.; Pellegrino, S. Wrinkled membranes iii: numerical simulations. **Journal of Mechanics of Materials and Structures**, v. 1, n. 1, p. 63–95, 2006.

Xu, X.; Luo, Y. Form-finding of nonregular tensegrities using a genetic algorithm. **Mechanics Research Communications**, v. 37, n. 1, p. 85–91, 2010.

Yang, S.; Sultan, C. Modeling of tensegrity-membrane systems. **International Journal of Solids and Structures**, v. 82, p. 125 – 143, 2016.

Yang, S.; Sultan, C. A comparative study on the dynamics of tensegrity-membrane systems based on multiple models. **International Journal of Solids and Structures**, v. 113, p. 47–69, 2017.

Yang, S.; Sultan, C. Deployment of foldable tensegrity-membrane systems via transition between tensegrity configurations and tensegrity-membrane configurations. **International Journal of Solids and Structures**, v. 160, p. 103–119, 2019.

Yeh, F.-Y.; Chang, K.-C.; Sung, Y.-C.; Hung, H.-H.; Chou, C.-C. A novel composite bridge for emergency disaster relief: Concept and verification. **Composite Structures**, v. 127, p. 199–210, 2015.

Yu, X.; Yang, Y.; Ji, Y. Automatic form-finding of n-4 type tensegrity structures. **Latin American Journal of Solids and Structures**, v. 19, 2022.

Zhang, J.; Ohsaki, M. Adaptive force density method for form-finding problem of tensegrity structures. **International Journal of Solids and Structures**, v. 43, n. 18-19, p. 5658–5673, 2006.

Zhang, J.; Ohsaki, M. **Tensegrity structures**. [S.l.]: Springer, 2015. v. 7.

Zhang, J. Y.; Ohsaki, M. **Tensegrity structures - form, stability and symmetry**. [S.l.]: Springer, 2015.

Zhang, L.; Gao, Q.; Liu, Y.; Zhang, H. An efficient finite element formulation for nonlinear analysis of clustered tensegrity. **Engineering Computations**, v. 33, p. 252–273, 2016.

Zhang, L.-Y.; Li, Y.; Cao, Y.-P.; Feng, X.-Q.; Gao, H. A numerical method for simulating nonlinear mechanical responses of tensegrity structures under large deformations. **Journal of Applied Mechanics**, v. 80, n. 6, p. 061018, 2013.

Zhang, L.-Y.; Li, Y.; Cao, Y.-P.; Feng, X.-Q. Stiffness matrix based form-finding method of tensegrity structures. **Engineering Structures**, v. 58, p. 36–48, 2014.

Appendix

APPENDIX A – KRONECKER PRODUCT

If $\mathbf{H}$ is a $i \times j$ matrix and $\mathbf{G}$ is a $\alpha \times \beta$ matrix, the Kronecker product $\mathbf{H} \otimes \mathbf{G}$ of dimensions $i\alpha \times j\beta$ is defined in equation A.1.

$$\mathbf{H} \otimes \mathbf{G} = \begin{bmatrix} H_{11}\mathbf{G} & H_{12}\mathbf{G} & \cdots & H_{1j}\mathbf{G} \\ H_{21}\mathbf{G} & H_{22}\mathbf{G} & \cdots & H_{2j}\mathbf{G} \\ \vdots & \vdots & \ddots & \vdots \\ H_{i1}\mathbf{G} & H_{i2}\mathbf{G} & \cdots & H_{ij}\mathbf{G} \end{bmatrix} =$$

$$= \begin{bmatrix} \begin{bmatrix} H_{11}G_{11} & H_{11}G_{12} & \cdots & H_{11}G_{1\beta} \\ H_{11}G_{21} & H_{11}G_{22} & \cdots & H_{11}G_{2\beta} \\ \vdots & \vdots & \ddots & \vdots \\ H_{11}G_{\alpha 1} & H_{11}G_{\alpha 2} & \cdots & H_{11}G_{\alpha\beta} \end{bmatrix} & H_{12}\mathbf{G} & \cdots & H_{1j}\mathbf{G} \\ H_{21}\mathbf{G} & H_{22}\mathbf{G} & \cdots & H_{2j}\mathbf{G} \\ \vdots & \vdots & \ddots & \vdots \\ H_{i1}\mathbf{G} & H_{i2}\mathbf{G} & \cdots & H_{ij}\mathbf{G} \end{bmatrix} \tag{A.1}$$

APPENDIX B – PERMISSION TO USE CONTENT – ELSEVIER

All copyright clearances from Elsevier are presented in tables B.2 and B.1 and in the Frequently Asked Questions available in Elsevier's website:

Can I use material from my Elsevier journal article within my thesis/dissertation?

As an Elsevier journal author, you have the right to Include the article in a thesis or dissertation (provided that this is not to be published commercially) whether in full or in part, subject to proper acknowledgment; see the Copyright page for more information. No written permission from Elsevier is necessary.

This right extends to the posting of your thesis to your university's repository provided that if you include the published journal article, it is embedded in your thesis and not separately downloadable.

See https://www.elsevier.com/about/policies/copyright for a complete description of Elsevier's permissions and https://www.elsevier.com/about/policies/copyright/permissions for a route to permissions guide.

Table B.1 – Institution rights in Elsevier's proprietary journals

Institution rights in Elsevier's proprietary journals (providing full acknowledgement of the original article is given)	**All articles**
Copies can be distributed electronically as well as in physical form for classroom teaching and internal training purposes	✓
Material can be included in coursework and courseware programs for use within the institution (but not in Massive Open Online Courses)	✓
Articles can be included in applications for grant funding	✓
Theses and dissertations which contain embedded final published articles as part of the formal submission can be posted publicly by the awarding institution with DOI links back to the formal publication on ScienceDirect	✓

Table B.2 – Author rights in Elsevier's proprietary journals.

Author rights in Elsevier's proprietary journals	**Published open access**	**Published subscription**
Retain patent and trademark rights	✓	✓
Retain the rights to use their research data freely without any restriction	✓	✓
Receive proper attribution and credit for their published work	✓	✓
Re-use their own material in new works without permission or payment (with full acknowledgement of the original article): 1. Extend an article to book length 2. Include an article in a subsequent compilation of their own work 3. Re-use portions, excerpts, and their own figures or tables in other works.	✓	✓
Use and share their works for scholarly purposes (with full acknowledgement of the original article): 1. In their own classroom teaching. Electronic and physical distribution of copies is permitted 2. If an author is speaking at a conference, they can present the article and distribute copies to the attendees 3. Distribute the article, including by email, to their students and to research colleagues who they know for their personal use 4. Share and publicize the article via Share Links, which offers 50 days' free access for anyone, without signup or registration 5. Include in a thesis or dissertation (provided this is not published commercially) 6. Share copies of their article privately as part of an invitation-only work group on commercial sites with which the publisher has a hosting agreement	✓	✓
Publicly share the preprint on any website or repository at any time (see *Sharing Policy* for more information).	✓	✓
Publicly share the accepted manuscript on non-commercial sites	✓	✓ using a CC BY-NC-ND license and usually only after an embargo period
Publicly share the final published article	✓ in line with the author's choice of end user license	×
Retain copyright	✓	×

APPENDIX C – PERMISSION TO USE CONTENT – ASME

The copyright agreement available in this appendix provides clearance to use the paper to *perform, lecture, teach, conduct related research, display all or part of the Paper, and create derivative works in print or electronic format. Author may reproduce and distribute the Paper for non-commercial purposes only.* See https://www.asme.org/rights-and-permissions for a complete description of ASME's permissions.

COPYRIGHT AGREEMENT (as of February 2010)

ASME Publishing • Two Park Avenue • New York, NY 10016

For questions about Conference paper copyright, please e-mail copyright@asme.org

For questions about Journal paper copyright, please email journalcopyright@asme.org

Before publication of your paper in a conference proceedings or journal, ASME must receive a signed Copyright Agreement. For conference papers, this form should be received by the deadline indicated by the Conference. Other forms may NOT be substituted for this form, nor may any wording on the form be changed.

PAPER NUMBER (for conference/journal papers): JMR-23-1476

TITLE: A dynamical model for control of a guyed tensegrity beam under large displacements

AUTHOR(s): Victor Paiva

CONFERENCE NAME:

JOURNAL NAME: Journal of Mechanisms and Robotics

ASME requests that authors/copyright owners assign copyright to ASME in order for a conference or journal paper to be published by ASME. Authors exempt from this request are direct employees of the U.S. Government, whereby papers are not subject to copyright protection in the U.S., or non-U.S. government employees, whose governments hold the copyright to the paper. Otherwise, the author/ copyright owner(s) of the Paper should sign this form as instructed below. Please refer to the section below "Who Should Sign" and also to ASME's FAQ page for more information regarding copyright ownership and the copyright process.

WHO SHOULD SIGN

Only the copyright owner(s) of the Paper, or an authorized representative, can sign this form. If one of the following applies, you may not own the copyright to the paper, or you may not be authorized to sign this agreement, and you may need to have the appropriate copyright owner(s) or organization representative sign this Agreement:
(1) You created the Paper within the scope of your employment, and your employer is the copyright owner
(2) You created the Paper under an independent contractor agreement**
(3) You received a grant that funded your Paper.

Please review your company policies regarding copyright, and if you are not authorized to sign this agreement, please forward to the appropriate organization representative. Please review applicable company, institutional, and grant policies and your employment/independent contractor agreement to determine who holds the rights to your Paper. For more information, please refer to the FAQs.

****Note to U.S. Government Contractors:** If you created the Paper under contract with the U.S. Government, e.g., U.S. Government labs, the paper may be subject to copyright, and you or your employer may own the copyright. Please review your company/institutional policies and your contractor agreement. Your Paper may also require a footer acknowledging contract information and also the following statement:

"The United States Government retains, and by accepting the article for publication, the publisher acknowledges that the United States Government retains, a non-exclusive, paid-up, irrevocable, worldwide license to publish or reproduce the published form of this work, or allow others to do so, for United States Government purposes."

It is your responsibility to ensure that the final PDF version of the Paper you submit includes all necessary footers and statements required under your contract.

COPYRIGHT ASSIGNMENT

The following terms of copyright assignment refer to Sections 1, 2, and 3. Sections 4 and 5 may not be subject to copyright.

The undersigned hereby assigns irrevocably to ASME all worldwide rights under copyright in the Paper.

Authors retain all proprietary rights in any idea, process, procedure, or articles of manufacture described in the Paper, including the right to seek patent protection for them. Authors may perform, lecture, teach, conduct related research, display all or part of the Paper, and create derivative works in print or electronic format. Authors may reproduce and distribute the Paper for non-commercial purposes only. Non-commercial applies only to the sale of the paper per se. For all copies of the Paper made by Authors, Authors must acknowledge ASME as original publisher and include the names of all author(s), the publication title, and an appropriate copyright notice that identifies ASME as the copyright holder.

PLEASE READ THE TERMS AND CONDITIONS WHICH ARE FULLY INCORPORATED IN THIS AGREEMENT.

PAPERS OWNED BY EMPLOYER OF AUTHOR(s) (Author may sign if so authorized; otherwise, an officer or other authorized agent of the employer should sign below.)

Author or Authorized Agent

Name: Victor Paiva Signature: Victor Paiva Date: 21 Aug 2023

Affiliation: University of Campinas Title: PhD Student
(Company or Institution)

Street Address: Rua Mendeleyev, 200

Campinas 13083-860 Brazil
(City) (State) (Zip Code) (Country)

Phone: 551935213226 Fax: Email: victorasmpaiva@gmail.com

Author: (Applied only if you are signing for other)

Name: Signature: Date:

Affiliation: Title:
(Company or Institution)

Street Address:

(City) (State) (Zip Code) (Country)

Phone: Fax: Email:

ASME COPYRIGHT FORM TERMS AND CONDITIONS

The following terms and conditions are fully incorporated into the Copyright Form. Please read them carefully.

REPRESENTATIONS, OBLIGATIONS, ACKNOWLEDGEMENTS, AND INDEMNIFICATION

You represent and acknowledge that:

(A) This Paper represents: either the first publication of material or the first publication of an original compilation of information from a number of sources as specifically noted by footnotes and/or bibliography.

(B) You have the right to enter into this Copyright Form and to make the assignment of rights to ASME. If the Paper contains excerpts from other copyrighted material (including without limitation any diagrams, photographs, figures or text), you have acquired in writing all necessary rights from third parties to include those materials in the Paper, and have provided appropriate credit for that third-party material in footnotes or in a bibliography.

(C) If you are signing this Form on behalf of any co-authors or other copyright holders, you have obtained express authorizations from all those authors and/or copyright holders to make this assignment of rights to ASME.

(D) To the best of the author's knowledge, all statements contained in the Paper purporting to be facts are true or supported by reasonable scientific research, the Paper does not contain any defamatory or libelous material and does not infringe any third party's copyright, patent, trade secret, or other proprietary rights and does not violate the right of privacy or publicity of any third party or otherwise violate any other applicable law; furthermore that to the best of your ability, you are responsible for ensuring the accuracy of your research and the Paper's content.

(E) If the Paper was produced in the course of an author's employment by, or contractual relationship with, the U.S. Federal or State Government and/or contains classified material, it has been appropriately cleared for public release and such is indicated in the paper.

(F) The Paper is not subject to any prior claim, encumbrance or form and is not under consideration for publication elsewhere.

(G) You have appropriately cited and acknowledged all third parties who have contributed significantly in the Paper's technical aspects.

(H) ASME is not responsible for any misrepresentation, errors or omissions by those signing this copyright form.

(I) All print and electronic copies of the Paper submitted to ASME become ASME's physical property regardless of whether or not ASME publishes the Paper, and that ASME is not obligated to publish your paper (see the Termination Section below if your paper is not published).

(J) ASME is not responsible for any of your expenses incurred in connection with preparing the Paper or attending meetings to present it, nor will ASME pay you any financial compensation if it publishes your Paper.

(K) Subject to and to the maximum extent permitted by law, you agree to indemnify and hold harmless ASME from any damage or expense related to a breach of any of the representations and warranties above.

TERMINATION

If ASME decides not to publish your Paper, this Form, including all of ASME's rights in your Paper, terminates and you are thereafter free to offer the Paper for publication elsewhere.

GENERAL PROVISIONS

This Copyright Form, the Terms & Conditions, and ASME Copyright Guidelines, constitutes the entire agreement between you and ASME, and supersedes all prior or current negotiations, understandings and representations, whether oral or written, between you and ASME concerning the Paper.

This Agreement is governed by, and should be construed in accordance with, the laws of the State of New York, United States of America, applicable to agreements made and performed there, except to the extent that your institution is prohibited by law from entering contracts governed by New York law, in which limited case this Agreement is governed by, and should be construed in accordance with, the laws of the jurisdiction in which your institution is located. Any claim, dispute, action or proceeding relating to this Agreement may be brought only in the applicable state and federal courts in the State and County of New York, and you expressly consent to personal jurisdiction and venue in any of those courts.

APPENDIX D – PERMISSION TO USE CONTENT – SPRINGER

All copyright clearances from Springer Nature are presented in table D.1. See https://www.springernature.com/licensing-and-copyright for a complete description of Springer Nature's permissions and https://www.springernature.com/third-party for a route to permissions guide.

Table D.1 – Author rights under different Springer Nature licence agreements.

Author rights	**OA licence agreement - CC BY 4.0**	**OA licence agreement - CC BY-NC-ND 4.0**	**Springer Nature Subscription licence agreement**
Retain copyright, patent, and trademark rights	Yes	Yes	Yes
Reuse their own material in new published works without permission or payment	Yes	Yes	Yes, see licensing agreement for details
Reproduce their own work for the purpose of course teaching	Yes	Yes, for non-commercial purposes	Yes, for non-commercial purposes
Reuse their work in a thesis written by the Author	Yes	Yes	Yes
Reuse graphic elements in presentations and other works created by the Author	Yes	Yes	Yes
Share the final published work with peers	Yes	Yes	Limited sharing for research and career advancement allowed
Deposit a preprint of their original research manuscript	Yes	Yes	Yes
Self-archive the accepted manuscript (AM) in an institution/funder repository	Yes	Yes, under the same terms as the licence applicable to the article	Yes, subject to SN's self-archiving policy, embargo period, and deposition terms